National Library of Canada
Acquisitions and Bibliographic Services Branch
395 Wellington Street
Ottawa, Ontario
K1A 0N4

Bibliothèque nationale du Canada
Direction des acquisitions et des services bibliographiques
395, rue Wellington
Ottawa (Ontario)
K1A 0N4

A Theoretical Study of Radio-Frequency Ablation of the Myocardium

by
Sylvain Labonté

A thesis submitted to the
School of Graduate Studies and Research
in partial fulfillment of the requirements for the degree of

Doctor of Philosophy

Ottawa-Carleton Institute for Electrical Engineering

Department of Electrical Engineering
Faculty of Engineering
University of Ottawa

ISBN 0-315-93589-8

Canada

UNIVERSITÉ D'OTTAWA
UNIVERSITY OF OTTAWA

Abstract

Theoretical modeling of the lesion formation process during radio-frequency ablation of the myocardium is presented. The model is axisymmetric and consists of a catheter electrode coming in contact at right angle with the heart tissue. The electric power dissipated in the tissue is calculated and from it the temperature distribution and the resulting lesion are evaluated as a function of time. The cooling effect of the blood flow and the temperature dependence of the electrical conductivity are included in the model, making it non-linear. The finite-element method is used to discretize the spatial domain and a finite-difference algorithm resolves the time dependence.

The numerical simulator is validated with a series of experiments performed on a tissue-equivalent material. Both the measured temperature distribution in the tissue sample and the electrode resistance as a function of time agree well with the theoretical predictions.

The model is used to study the effect of the electrode geometry and the electrical excitation on the resulting lesion. Theoretical predictions for the time evolution of the lesion size and the electrode resistance are presented for the first time. Recommendations for the improvement of the RF ablation procedure are formulated.

Remerciements

Je remercie mes directeurs de thèse Dr. S.S. Stuchly et Dr. G. Costache pour leur supervision durant ces années d'études. Je tiens aussi à remercier Dr. A.S.L. Tang de l'institut de recherche en cardiologie pour les nombreuses discussions ayant trait à l'aspect médical de ce projet de recherche. Merci aussi au Conseil de recherches en sciences naturelles et en génie (CRSNG) et au Fonds pour la formation de chercheurs et l'aide à la recherche (FCAR) pour leur support financier durant ces études.

Je suis très reconnaissant envers M. Kevin Smith et M. Tristano Nicoletta de la compagnie BNR de Kanata pour m'avoir donné accès à la caméra infra-rouge utilisée dans cette recherche.

Je veux aussi exprimer mon appréciation à tous mes confrères qui se sont succédés depuis le début. À Marko, Karu, Richard, Rédouane, Michel, Chen, Mike, Hassan, Jean-François et tous les autres, merci pour les discussions animées qui ont agrémenté les longues heures à l'université.

Par-dessus tout je veux dire merci à Sylvie dont la compréhension, la patience et les encouragements ont rendu tout ceci possible. Enfin, merci à Florence pour sa joie de vivre et sa sérénité.

Contents

List of Figures

List of Tables

Chapter 1

Introduction

1.1 Motivation

Radio-frequency (RF) ablation is a medical procedure in which a RF electrical discharge is used to destroy small areas of the heart in order to cure cardiac arrhythmias. This technique was introduced around 1986. Its appeal comes from its simplicity, safety and relative efficacy compared to other approaches using laser or DC discharges.

This research was undertaken in 1989 and let us take a look back at the situation then. At that time, RF ablation is at the early developmental stage. In the medical community, much interest is demonstrated for the understanding of the mechanisms involved in the new technique. The available literature, dealing mainly with in-vitro experiments, is characterized by its empirical nature. Although the basics of RF ablation are known, in general very little theory is presented to support the experimental findings. The problem of comparing the results of different experiments and the absence of reliable theoretical data are responsible for the rather superficial understanding of the procedure.

Despite the lack of a thorough knowledge of it, the RF ablation technique is rapidly promoted from the laboratory to clinical trials. The interest of the main investigators for the mechanisms of ablation itself soon shifts to the clinical studies. Within a couple of years, the cardiologists develop a good command of the new technique. However part of the success comes from the fact that generally, the procedure is applied until the desired result is obtained. Today, the general attitude towards RF ablation seems to be that the lesions that it produces are not large enough. Already, new techniques based on microwave energy are being proposed as potential alternatives.

This research is motivated by the desire to understand the mechanisms of lesion formation during RF ablation. The rationale is that a more thorough understanding should lead to the identification of an optimal mode of ablation that maximizes the lesions.

1.2 Objectives and Approach

The global objective of this study is to gain insight into, and to quantify the thermal and electrical processes occurring during RF ablation. The main questions to be answered are:

- How superior is RF ablation compared to hot-tip ablation?
- How important is the blood flow?
- How significant is the electrode geometry?
- How can the applied RF power be used to optimize the lesion?
- How do tissue temperature and lesion progress with time?

A theoretical approach is used to answer these questions because it is more versatile and to some extent simpler than a study based on experimentation. Experiments would require equipment and medical expertise that is not readily available. Furthermore, the variety and variability of factors coming into play during experimentation often obscure the underlying mechanisms. A theoretical approach on the other hand can better identify and isolate the significant factors of ablation. Moreover, theoretical results (unavailable up to now) constitute a convenient basis for the evaluation of the efficacy of the procedure.

Because the problem is too complex for an analytical treatment, numerical modeling must be used. The **first objective** is thus to set-up a numerical model that is a reasonable representation of the physical reality.

Since the whole project relies heavily on the simulation results, it is essential that good confidence in the computer programs be developed. Simple examples with analytical solutions are used for a preliminary verification. However, the nature of the problems of interest is so complex that it is preferable to perform an experimental validation of the software on a more realistic problem. The **second objective** is therefore to realize an experiment whose results are used to validate the numerical simulator. This experiment must be complex enough to

lead to convincing conclusions, and at the same time simple enough to be workable. Ablation on an artificial material is done for that purpose.

The **third objective** is to carry out a series of simulations to build up a bank of theoretical results and to answer the questions raised above. Finally the **fourth objective** is to use the information obtained by the theoretical study to propose recommendations as to the optimal modes of RF ablation.

1.3 Organization of the Thesis

Chapter 2 of this thesis presents background information of a medical nature. The physiology of the heart is reviewed followed by a review of catheter ablation techniques using direct-current, laser and RF. This section is a succinct version of the review presented in the candidacy paper preliminary to this thesis.

Chapter 3 contains the description of the theoretical model used in this work. All the information on the modeling is included there. The model, the governing differential equations and the mathematical development are exposed. Little emphasis is put on the mathematics in order to lighten the presentation. The mathematical details are included in Appendices A,B, and C. A section is devoted to the physical properties of biological tissues which is a primordial aspect of modeling. Since this issue is rather complex, a fair amount of information is given. The major mechanisms responsible for the properties and a repertory of published values for the tissues of interest are presented. The last section contains a preliminary validation of the software done by considering simple cases with analytical solutions.

Chapter 4 presents an experiment performed to validate the modeling software on a realistic, non-linear problem. It consists in the measurement of the temperature distribution in a specimen of tissue-equivalent material submitted to RF ablation. Details are presented on the tissue-equivalent material itself, the electrical apparatus, and the thermographic camera used for the experiment. The results agree well with the theoretical predictions confirming the applicability of the software to the solution of RF ablation problems.

Chapter 5 consists of preliminary numerical calculations. Their purpose is to identify the determinant factors that must be included in the simulations. Of interest are the blood flow, the temperature dependent conductivity, the boundary conditions, and the model dimensions. After this preliminary investigation, the model is well defined and ready to be applied for the

simulation of RF ablation.

Chapter 6 is the modeling of ablation itself and constitutes the body of the thesis. The transient evolution of the lesion is calculated for various electrode shapes and electrical excitations. The data is presented so as to facilitate the comparison of various situations and to enable meaningful conclusions. Each simulation result is interpreted individually. A summary of all the results is presented in the discussion. Their application to the determination of an optimal method of RF ablation is discussed in the last section.

The final chapter concludes by summarizing the work done and suggesting avenues for further work.

1.4 Contribution

This is the first in-depth theoretical study of RF ablation. Consideration is given to most of the determinant factors of the procedure. In contrast to all previous reports which are experimental in nature, this study quantifies the effect of a series of factors taken in isolation. The specific contributions of this work are:

- Creation of a software environment for modeling the lesion formation process based on the finite-element time-domain method: automatic mesh generator, graphical mesh editor, finite element analysis software, graphics output. Most software is written in C and X Windows on DECstation 3100 workstations. The analysis considers the temperature dependence of the electrical conductivity and is therefore non-linear.

- Realization of an experiment to validate the theoretical analysis. This includes the realization of a tissue-equivalent material at 1 MHz and the construction of the experimental apparatus.

- For the first time, a theoretical evaluation of the significant factors of RF ablation is presented: importance of blood flow, effect of electrode geometry, transient evolution.

- Well supported recommendations are made about the optimal mode for ablation.

The expertise developed in this study has fostered a growing collaboration with the University of Ottawa Heart Institute Research Center. Already, joint research on microwave ablation has been undertaken.

Chapter 2

Background

This chapter provides background information on the topic of this research. Information of a medical nature is presented in the first section and an overview of the catheter ablation technique is given in the second section.

2.1 The Heart

Here is a summary of the medical knowledge necessary to understand the topic of this work. By no means is it an exhaustive treatment of the material. It is intended to provide a basic understanding of the physiology of the heart, of cardiac arrhythmias and of the catheterization technique. Its purpose is also to introduce the medical terms used in this work. The following references have been consulted for the writing of this section [1, 2, 3, 4].

2.1.1 Physiology of the Heart

The heart is a hollow muscular organ whose function is to pump blood in the circulatory system of the body. Its walls are made of muscle fibers and are called the myocardium. The inside surface of the myocardium is the endocardium. The heart can be divided longitudinally into two functionally similar parts (the right and left heart) each containing two chambers: the atrium and the ventricle (Figure 2.1). The two atria and the two ventricles respectively share a common wall called the atrial and the ventricular septa. The right heart pumps the blood returning from the periphery towards the lungs for oxygenation. The left heart pumps the oxygenated blood returning from the lungs towards the periphery.

The great vessels conduct the blood in and out of the heart. They are the superior and inferior vena cava at the input of the right atrium, the pulmonary arteries and veins,

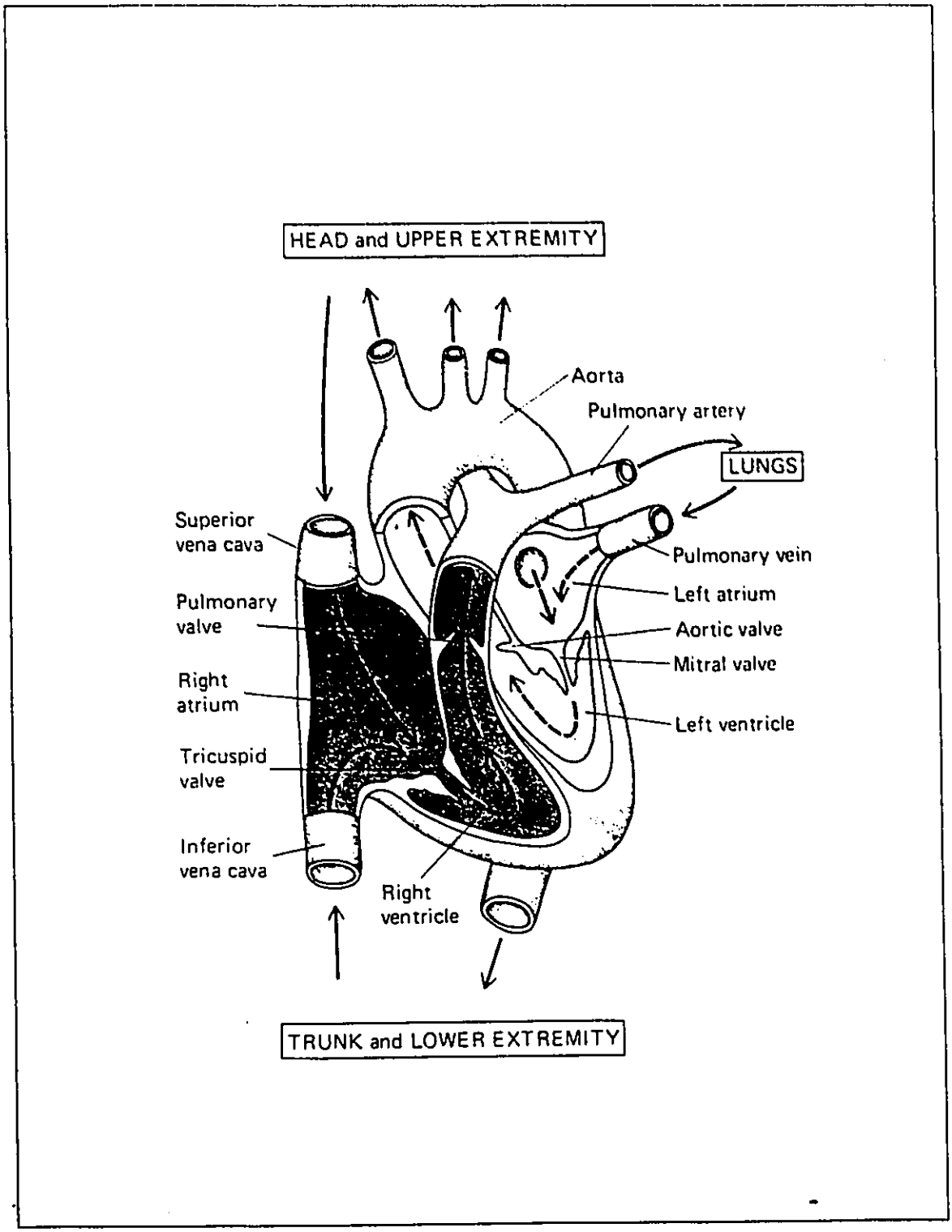

Figure 2.1: A schematic representation of the heart showing its principal structures. From [5, p. 82].

respectively at the output of the right ventricle and the input of the left atrium, and finally the aorta at the output of the left ventricle. The direction of the flow in the heart is controlled by passive valves at the orifices of the chambers. Three of them are of a particular interest (Figure 2.2). The right and left atrioventricular valves separate their respective atrium and ventricles. The right one is made of three cusps (the tricuspid valve) designated by their position as anterior, posterior and septal (near the septum) cusps. The left atrioventricular valve comprises two cusps, the anterior and posterior. At the root of the aorta are located the three aortic semilunar valves. The heart valves allow the passage of blood in one direction and prevent back flow when pressure gradient is reversed. The ventricle side of the atrioventricular valves are attached by tendinous cords, the *chordae tendinae*, to the interior wall of the ventricles. This arrangement stays the valves against the ventricular pressure since the valves have no intrinsic rigidity.

The supply in nutrients to the myocardium is done through the coronary circulation, a network of arteries and veins covering the heart. The arterial supply is provided by the right and left coronary arteries. They arise from the root of the ascending aorta just above and behind two of the three aortic semilunar valves. The coronary arteries branch out and cover the myocardium to supply oxygenated blood. The blood is then drained by the coronary veins which for the most part accompany the coronary arteries. The principal terminus of the veins is the coronary sinus. This is a short, wide venous channel on the posterior side of the heart, between the atria and the ventricles (Figure 2.2). The coronary sinus opens into the right atrium between the inferior vena cava and the atrioventricular opening (Figure 2.3).

To effectively pump the blood, the four chambers of the heart beat in an orderly sequence: The contraction of the atria is followed by the contraction of the ventricles and by a rest period where all chambers are relaxed. For effective blood expulsion, the ventricular contraction must progress from the apex (the tip of the ventricles) to the base (the end with the valves). The complete heartbeat originates in a specialized conduction system with intrinsic coordination of the event.

Before the origin of the heartbeat is described, it is useful to say a few words about muscle excitation. All muscle fibers including the myocardial fibers contract in response to a sudden flow of ions in both directions across their membranes. This results in a sudden

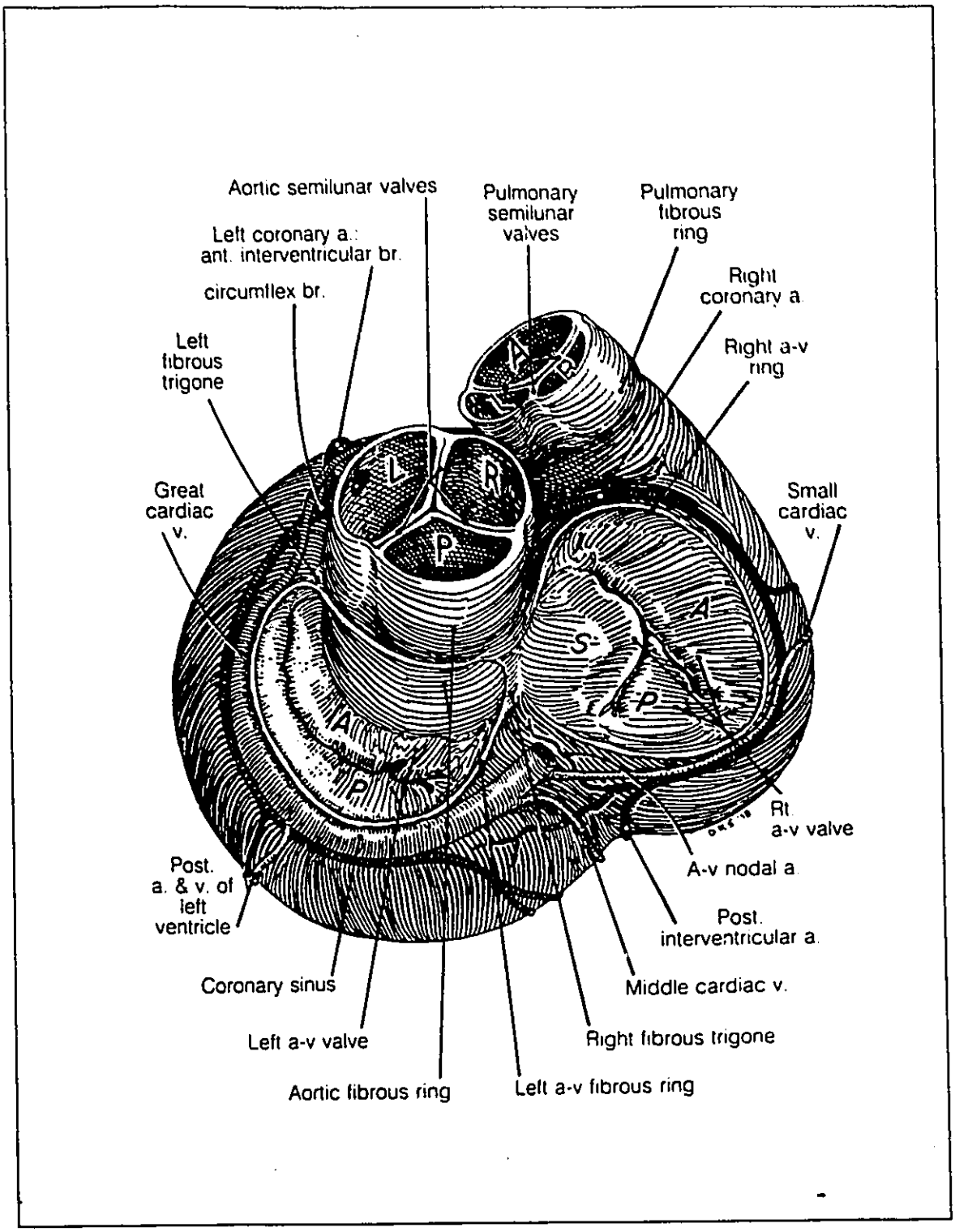

Figure 2.2: A section of the heart between the atria and the ventricles, looking down at the ventricles. The heart valves, the coronary arteries and the coronary sinus are shown. From [1, p. 383].

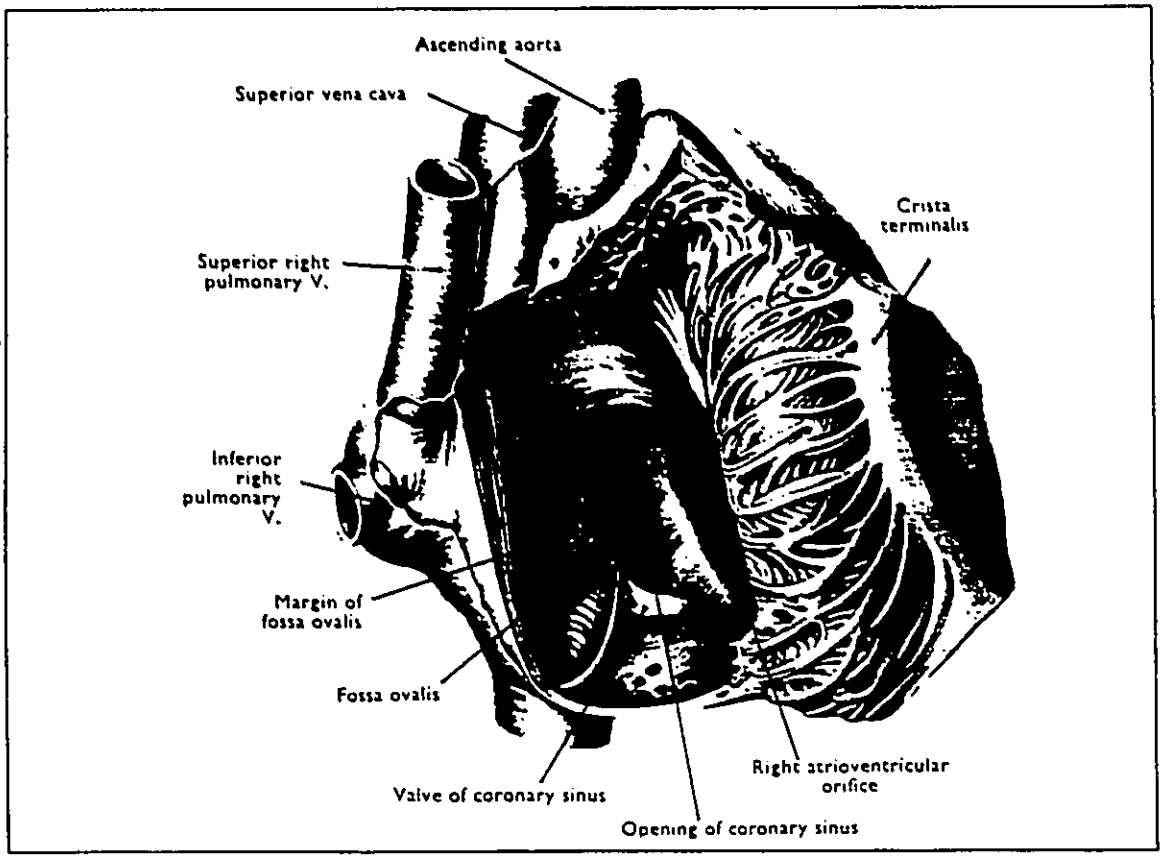

Figure 2.3: The interior of the right atrium exposed by turning its right and anterior wall to the left. From [2, p. 48].

change in the voltage difference normally maintained across the membrane. Accordingly, the phenomenon is called *depolarization*. Because of special junctions between individual myocardial fibers, depolarizations can propagate from a fiber to its neighbors. After a fiber has been excited, it relaxes and remains refractory to subsequent depolarizations for a short period of time. This explains the outward propagation of the depolarization fronts. In the normal heart, depolarizations travel freely over the myocardium but can not travel directly between the atria and the ventricles because these are separated by a layer of isolating fibrous tissue. Electrical conduction between them is nonetheless necessary and is provided by the specialized conduction system.

The structures that make up the conduction system are the sinoatrial node, the atrioventricular node, the bundle of His and the Purkinje fibers (Figure 2.4). The sinoatrial (SA) node is a small collection of specialized myocardial fibers with spontaneous, rhythmic depolarization. The SA node is the pacemaker of the heart and this is where the heartbeat is initiated. It is located at the intersection of the superior vena cava and the right atrium. The AV node is made of the same kind of tissue as the SA node and is situated in the septal wall of the right atrium between the opening of the coronary sinus and the septal cusp of the atrioventricular valve.

The bundle of His is a strand of specialized myocardium establishing an electrical connection between the AV node and the ventricles. It passes from the AV node into the ventricular septum. At the top of the ventricular septum, the bundle of His gives off a left branch and continues as the right branch. Both branches run subendocardially down either side of the septum toward the apex. There, they come in contact with the fast Purkinje fibers[1] which diffuse the excitation to all parts of the ventricular myocardium. This diffusion makes possible a more or less simultaneous contraction of all ventricular fibers.

Figure 2.5 shows the spread of the electrical activity in the normal heart. The impulse from the SA node reaches the atrioventricular (AV) node through myocardial conduction in the atrium walls. The AV node is responsible for the delay between the ventricular and atrial contraction by retarding the propagation of the excitation by 0.1 s approximately. The impulse then follows the bundle of His to the Purkinje fibers to initiate the ventricular

[1]Conduction speed in the Purkinje fibers is about 4 times higher than in the ventricles in order to excite the apex first.

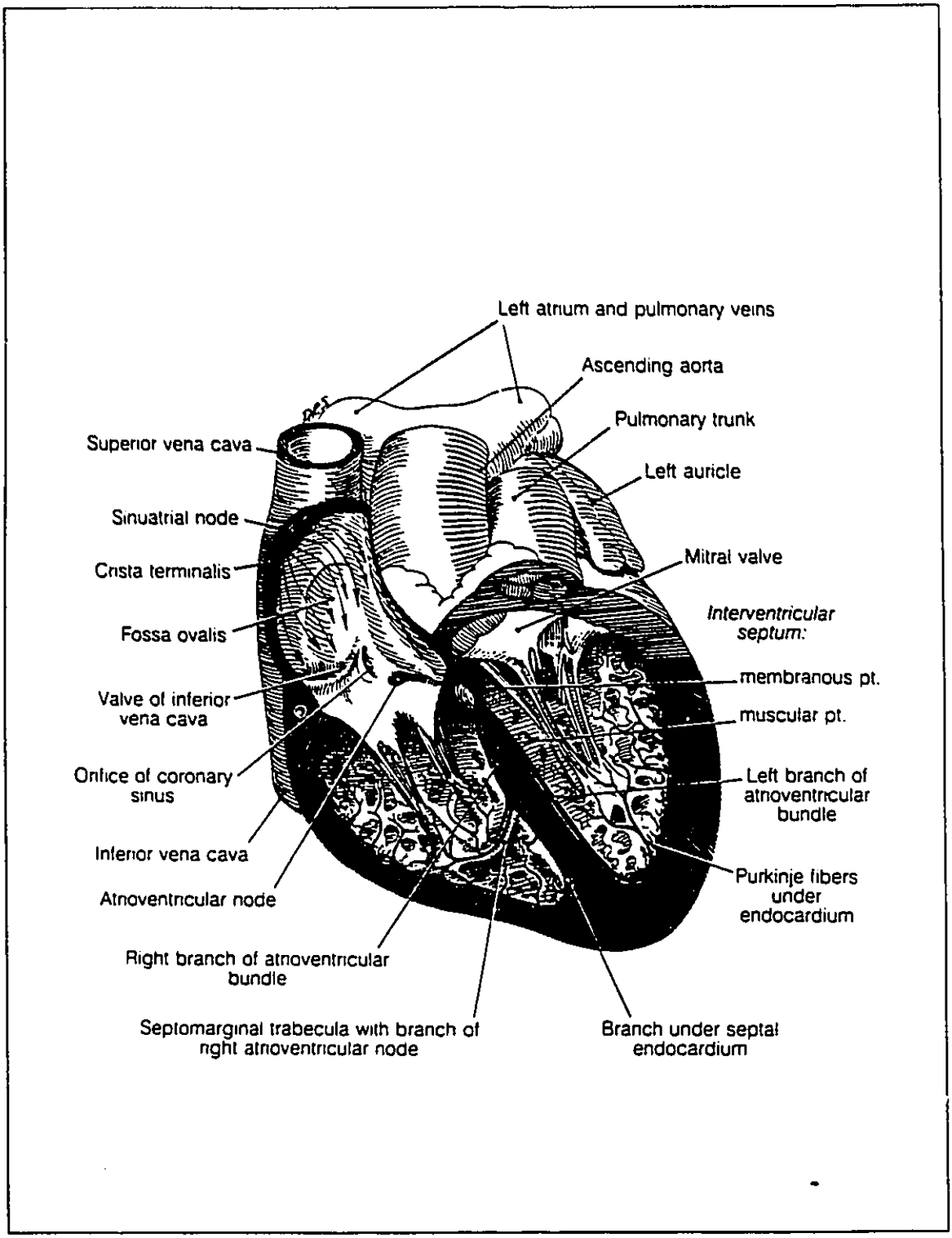

Figure 2.4: The specialized electrical conduction system of the heart. From [1, p. 386].

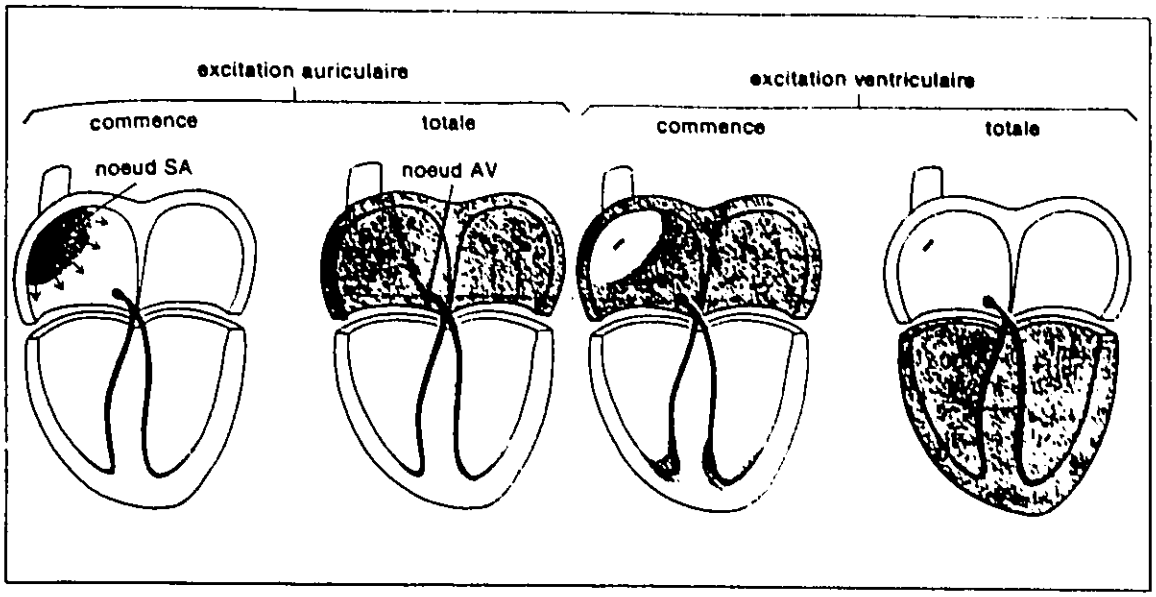

Figure 2.5: Normal spread of the electrical activity in the heart. From [3, p. 223].

contraction.

In the normal heart, the AV node and the bundle of His (sometimes called the AV junction) constitute the only conduction pathway between the atria and the ventricles. When this pathway is totally or partially interrupted, an AV block is said to be present. AV blocks can take several forms and are differentiated into various degrees. The first and second degree blocks correspond to slowed conduction whereas a third degree block is a complete interruption. When a third degree AV block is produced, a permanent pacemaker is essential to maintain adequate ventricular excitation.

2.1.2 Cardiac Arrhythmias

Various anomalies of the heart can result in the loss of synchronization and departure from the normal pace. These are called arrhythmias. Two phenomena are associated with the initiation of arrhythmias: an ectopic focus of excitation and reentry. An ectopic focus is a group of cells that develops spontaneous rhythmic activity and imposes its pace to the rest of the heart. These can occur in both the atria and ventricles. Reentry is a defect that permits a wave of excitation to propagate continuously within a closed circuit called circus movement. Zones of delayed conduction or increased refractoriness are substrate for reentrant arrhythmias. Circus movements can also become established between the atria and

the ventricles when, in addition to the His bundle, an accessory conduction pathway develops between them.

Cardiac arrhythmias can take the form of an irregular or an accelerated pace (200 bpm and more) resulting in less effective blood pumping. In the worst cases, ventricular fibrillation can occur. It consists in an unsynchronized contraction of all ventricular fibers due to the existence of several ectopic foci. During fibrillation no blood is pumped and unless emergency procedures are undertaken, it is fatal.

When an arrhythmia can not be controlled by pharmaceutical treatment the abnormal tissues responsible for it must be ablated. For atrial arrhythmias, and independently of their point of origin, the ablation of the AV junction will prevent the excitations from reaching the ventricles. Alternately, if the ectopic focus can be localized, its destruction will cure the problem. Unfortunately, the resulting lesion may sometimes itself be arrhythmogenic because of the reentry phenomenon. For an arrhythmia due to the presence of an accessory conduction pathway between the ventricles and the atria, the interruption of this pathway can be a solution.

The ablation of these structures can be performed during open-heart surgery or using catheter techniques. The latter consists in ablating the tissue with a catheter that is introduced in a peripheral vessel and advanced into the heart chambers. It represents a higher degree of complexity both in the access to the tissues to be ablated and the ablation modality. On the other hand, it is less traumatic for the patient and less expensive than surgery. These advantages stimulate the development of catheter ablation. The various methods proposed for it are reviewed later.

2.1.3 Catheterization

Cardiac catheterization consists in advancing a catheter through a blood vessel in an arm, a leg or the neck, and into the heart, usually under fluoroscopic control (real-time X-rays). Many types of catheters are available for different functions such as blood sample collection, biopsy and pressure measurement. Of relevance to this work are the catheters used for electrophysiological studies (EPS). They consist of a suitably insulated electrical conductor exposed at the distal end to form an electrode. The proximal end is connected to an electronic instrument for the recording or generation of electrical signals. So-called bipolar and

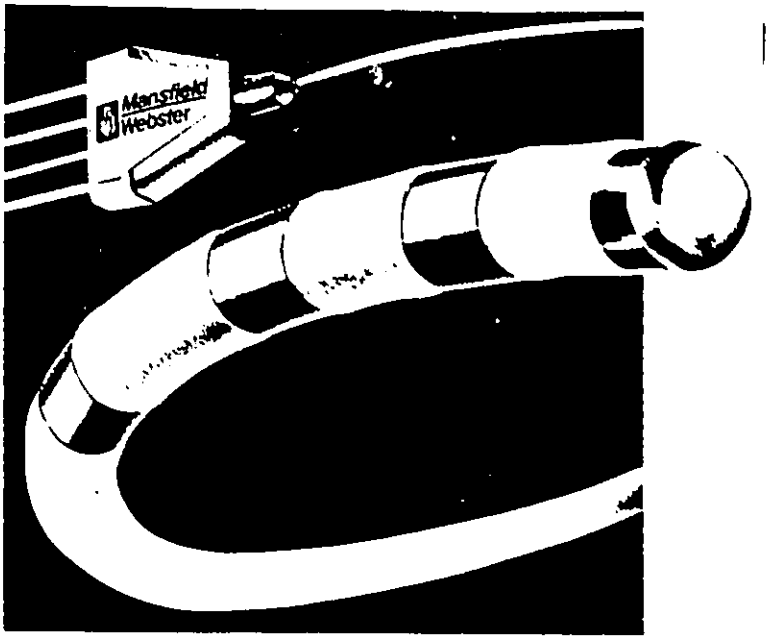

Figure 2.6: Drawing of a 6F quadripolar recording catheter showing the 4 electrodes and the proximal 4-lead connector.

quadripolar catheters with 2 and 4 independent conductors are common. In those cases, the electrodes often take the form of metal rings around the catheter. Catheter size is measured in the rather peculiar units of French (F). Three French correspond to a diameter of 1 mm. A 6F, quadripolar catheter has four independent electrodes, and an outside diameter of 2 mm (see Figure 2.6).

A whole set of specialized EPS catheters are available depending on the particular cardiac structure to be paced or whose electrical activity is to be recorded[2]. Those catheters differ by their inter-electrode spacing and electrode length. Furthermore, despite their flexibility for smooth approach to the heart chambers, they have pre-formed bends to facilitate access to the desired sites. Catheterization is not an easy technique and the situation is exacerbated by the heart and valve movements and the blood flow which tend to displace the tip of the catheter. Because of the intra-cardiac geometry, some structures (coronary sinus, AV junction, ventricular apex) are easier to reach than others.

The difficulty in locating the site to be ablated by catheter techniques is also an important problem. At the present, the approach used is to record electrograms with an electrode

[2]Electrode catheters are available from several American companies such as United States Catheter and Instrument Company, Billerica, Mass., or Mansfield Scientific Inc., Mansfield, Mass.

catheter that is moved around until a suitable pattern of electrical activity is identified. Depending on the type of arrhythmia, this "target pattern" can be more or less well-defined and the selection of the ablation site depends on the examiner's experience. The uncertainty of the process comes from the combination of three factors. First, only a limited number of locations on the endocardium can be reached and therefore the site chosen for ablation is the best among *the available sites*. Second, the electrical activity is recorded at only one site at a time and from this it is not always clear which location is the best for ablation. Thirdly, the movements of the heart and the flow of blood contribute to displace the electrode between the time the electrogram is recorded and the ablation itself.

2.2 Catheter Ablation

The removal of undesired tissues can be performed by several methods with various degrees of sophistication: conventional surgery, electrosurgery, cryosurgery, laser and even acoustic waves. These techniques offer advantages and disadvantages in terms of safety, controllability and side-effects. The choice of the surgeon is therefore a trade-off based on the nature of the intervention, the acceptable level or risks and complications, the availability of the equipment and personal experience. We saw earlier that it is sometimes necessary to perform the ablation of internal heart tissues for the treatment of arrhythmias. In these cases, so-called catheter techniques present interesting advantages because they eliminate the need for open-chest surgery. Three methods of ablation amenable to catheter use in cardiology have been proposed. The first one is called direct-current (DC) ablation and consists in applying a high-current pulse at the target site. The second approach is to use a laser beam to vaporize the target. Finally, the third method, referred to as radio-frequency ablation involves the flow of an alternative current through the tissue to be ablated. Historically, in cardiology, DC catheter ablation was introduced first. However, unacceptable complications stimulated the quest for safer methods and laser and RF ablation were investigated. Today, RF ablation seems to be the preferred solution as it combines safety, simplicity and relative efficacy.

A review of catheter ablation techniques was presented in a preliminary document [6]. A summary is given here.

2.2.1 DC Ablation

Catheter DC discharges have been used to ablate AV junctions, accessory pathways and ventricular ectopic foci. Despite its relative success, this procedure is not free of complications and animal and clinical tests demonstrated side effects including ventricular fibrillation and rupture of the coronary sinus. Fontaine [7] and Scheinman [8] edited review books on ablation techniques for cardiac arrhythmias where a great deal of information and many references are presented concerning the DC ablation technique.

Description

The DC catheter ablation procedure consists of an electrical discharge delivered through a catheter to produce a local burn. In clinical treatments, the total energy delivered is 100-400 J per pulse with peak voltage and current of 2-3 kV and 40-50 A for a duration of less than 10 ms. Conventional defibrillator units (consisting of a capacitor and an inductor in series) are normally used to produce the electrical shock. Two modes of discharge can be used:

- the *unipolar mode* where the current flows between a catheter electrode and a large grounded electrode positioned on the chest or the back of the patient, and
- the *bipolar mode* where the discharge is produced between two catheter electrodes near the target.

The flow of current from one electrode to the other elevates the local temperature. At low power levels, Joule heating is responsible for tissue destruction. However, if enough power is applied, an explosion takes place and the adjacent tissue is pulverized. Many investigators have described the sequence of events taking place during DC ablation under various conditions and have proposed an explanation of the physics behind it [9, 10, 11, 12, 13]. A particularly good treatment can be found in [14].

Clinical Experience with DC ablation

A good review of clinical experience with DC ablation is presented by Scheinman in [15]. Clinical details can also be found in [16] and [17] among others. The evidence suggests

that 90% of the patients suffering from drug refractory supraventricular arrhythmias are improved after attempted ablation of the AV junction. The procedure is as successful as surgical ablation but is cheaper to perform and associated with lower morbidity. In a series of attempts to produce AV block using catheter DC ablation, Bredikis *et al* [16] concluded that the difficulty in locating the optimal ablation site is responsible for occasional failure of the procedure.

The clinical experience with the ablation of accessory pathways and ventricular ectopic foci is more limited than that for AV junction because target location is harder. The success rate is not as high and the complications can be very serious (rupture of the coronary sinus) [18, 19].

Physiological Effects of DC ablation

Both anodal and cathodal discharges produce similar ellipsoidal lesions. The acute[3] histologic findings consist of necrosis, edema, and inflammatory cell infiltration. The chronic[4] findings include fibrosis[5] and fatty infiltration at the margin of the lesion. Abnormality in impulse conduction and refractoriness in large border zones around the lesion are also observed. For more details on the physiologic effects of DC ablation see [8, 13, 20, 21, 22].

Advantages and Disadvantages of DC ablation

DC catheter ablation is a very attractive alternative to surgery for the treatment of drug-refractory cardiac arrhythmias. The success of the procedure for some particular interventions is undeniable. However, it seems that the ablation procedure is hardly controllable, and the tissues surrounding the target site are often unnecessarily damaged.

The complications associated with DC ablation include more arrhythmias and perforation attributed to the shock wave. Another potential complication is the gas released during DC ablation which carries the risk of embolization. However, this has never been reported in animals or humans. Finally, because DC current can stimulate muscles and nerves, anesthesia is required during the intervention. These complications have encouraged the search for other

[3] Shortly after the ablation.

[4] After healing.

[5] The formation of fibrous tissue. This type of tissue is usually encountered in parts of organs that play a structural role like the fibrous rings of the heart which form its skeleton.

forms of energy for catheter ablation.

2.2.2 Laser Ablation

Laser is another form of energy that can be used for catheter ablation. It has been used in many clinical applications such as ophthalmology and dermatology and its application to cardiovascular treatment has been considered. Around 1984 Saksena and co-workers, who seem to be the main investigators of this technique, began experiments aimed at evaluating the clinical efficacy and safety of intraoperative and catheter myocardial ablation using laser. The information presented in two review papers by this group of investigators [23, 24] is summarized in this section. Today, the interest for catheter ablation of the myocardium using laser seems to have faded considerably.

Description

Special optical fiber catheters are used to deliver the laser energy to the heart. Unlike for DC ablation, the lesions induced by laser are essentially thermal in nature. The laser energy is absorbed by intra- and extra-cellular water vaporizing the cellular fluid. The tissue surface swells and ruptures with a popping sound and cellular debris and steam are released from the surface. The tissue surrounding the vaporized area undergoes thermal damage leading to coagulation necrosis[6] and charring. The gross lesions usually show a central crater lined with charred tissue. The extent of the coagulation and charring depends on the laser source and power level. Compared to DC ablation, the affected area appears to be much more localized without any significant border zone of delayed electrical conduction. Experiments where power and energy of laser irradiation are varied reveal that total delivered energy is the primary determinant of lesion dimensions. Comparable lesion sizes are obtained with pulsed or continuous wave laser at comparable energy levels [25].

Experiments with Laser Ablation

Only a very limited number of catheter experiments have been reported [26, 27] (none in humans). In addition to the fiber optic catheter, the technique necessitates a separate electrode

[6] Necrosis of a portion of some organ or tissue, in which a relatively small part seems to have been deprived of the afflux of blood by the plugging of its vessels with coagula.

catheter to aid in positioning.

Experiments in dogs show that complete or partial atrio-ventricular block can be produced by total or partial transection of His bundle fibers [23, 27]. In animal work, laser ablation has sometimes resulted in short bursts of nonsustained ventricular tachycardia and ventricular fibrillation [23, 26]. However it appears that these complications are less frequent than with DC ablation. The technique is highly experimental and information on long-term follow-up is limited.

The photoproducts of laser ablation in human myocardium have been found to reflect a high degree of tissue degradation: protein fragments, hydrogen, carbon monoxide and organic gases. All of these are water soluble and rarely form bubbles.

Advantages and Disadvantages of Laser Ablation

The laser injuries do not present a wide border zone of delayed electrical conduction. This and the comparative reduced arrhythmogenicity represent advantages over DC ablation. In addition, the hemodynamic and mechanical deleterious effects associated with DC are not found with laser ablation. On the other hand, the relative smallness of the lesions and the lack of controllability of catheter laser ablation are major drawbacks. Also, the need for a separate electrical catheter and a special fiber optic catheter and the cost and bulkiness of the equipment limit the interest for this technique.

2.2.3 Radio-frequency Ablation

Radio-frequency ablation is the destruction of tissue by the application of a RF electrical current. In this application, the term radio-frequency refers to the range 100 kHz to a few MHz. Like DC energy, RF energy is easily amenable to catheter application. A significant advantage of RF though, is that the discharges do not produce the pressure wave observed during DC ablation. Another advantage is that unlike lower frequencies, RF signals do not stimulate muscles and nerves. Therefore, unlike DC, the flow of a RF current through the heart is rarely associated with the incidence of ventricular fibrillation and does not require general anesthesia.

Description

Except for the generator, the procedures for ablation using RF and DC currents are very similar. RF energy can be delivered in the unipolar or bipolar mode by bringing the active electrode(s) in contact with the tissue to be ablated. At power levels (less than 30 watts) normally used for ablation, no gas bubble formation (electrolysis) is observed during the intervention which eliminates the harmful shock wave associated with DC ablation.

The lesions produced by RF catheter ablation are essentially the result of tissue destruction by protein denaturation due to overheating. No evidence of other types of chemical or physical degradation is observed at those levels of electric fields. RF current flows in the tissue and heat is produced by Joule effect. The resulting temperature distribution and consequently lesion shape is determined by energy deposition and thermal transfer phenomena that take place over the time of application. The electrode itself is heated by thermal conduction.

The lesions produced are described as sharply demarcated and composed of homogeneous scar tissue without interspersed myocardial fibers and the tissues surrounding the ablated area are generally completely spared. Therefore unlike the lesions produced by DC ablation, they do not constitute a favorable substrate for reentrant circuits and potential arrhythmias.

Development of RF Ablation

The clinical use of radio-frequency energy is not new. Electrosurgery, which refers to the use of RF energy to cut, coagulate or desiccate tissues, has been commonly utilized in operating rooms for over 40 years. In many fields of medicine, heating with RF energy has been employed to produce focused lesions or to induce hyperthermia: neurosurgery [28, 29], gastroenterology [30, 31], oncology [32]. It is in the mid 80's that RF energy was proposed as an alternative to DC catheter ablation [22, 33, 34, 35, 36, 37]. The success of the first experiments combined with the increased safety over DC ablation led to a very rapid development of this technique [38, 39, 40, 41, 42, 43, 44, 45, 46, 47, 48, 49, 50, 51]. The clinical trials reported in [52, 53, 54, 55, 56, 57, 58, 59] show that the technique produces good results. The enormous increase in the number of clinical reports on the subject between 1989 and 1992 illustrates that point very well. As of April 1992, RF ablation is used on a routine basis in

many centers in the USA and Canada (refer to the proceedings of recent scientific sessions of the American Heart Association and the American College of Cardiology [60, 61]). Historical reviews of the medical use of RF energy can be found in [33] and [34].

Current Status of RF Ablation

The RF ablation procedure basically consists in repeating the application of power until the desired effect is obtained, which partly explains the high success rates that are reported. It appears that the number and intensity of power applications necessary to cure the arrhythmias vary widely from patient to patient. The difficulty in locating the target might be the reason of this situation. At this time, increasing the lesion size seems to be the only solution to alleviate this problem. Despite the differences in procedures and equipment, it is possible to draw the following list of features common to most groups:

- Ablation is performed in the so-called unipolar mode, that is, between a catheter electrode and a skin electrode located on the scapula. 6F to 7,5F catheters are used with 4 mm long hemispherical tip electrode.
- RF power between 20 and 30 W is applied until the desired effect is obtained.
- The resistance between the ablation electrodes is in the order of 100 ohms.
- Often, an electro-surgical unit is used as the RF generator. The output is a continuous wave between 500 and 1000 kHz. Special generators are also available commercially.
- Voltage and current are monitored during the procedure in order to detect a sudden rise of the resistance revealing tissue charring and boiling which occurs at 100°C [47, 50]. This situation must be avoided because it prevents lesion progression.

Advantages and Disadvantages of RF Ablation

The experimental evidence confirms that RF ablation is very promising for the non-surgical treatment of cardiac arrhythmias. This technique offers the following advantages:

- It produces well delineated homogeneous scars with no intact myocardial fibers,
- it does not cause barotrauma and gas bubble formation,

- it is less arrhythmogenic and in general safer than DC,
- it does not require general anesthesia and
- it is relatively inexpensive.

Ablation with RF current provides the ability to better control the delivery of the energy. But the most significant advantage of RF over DC ablation is the reduction in associated medical complications [52]. A multicenter study [55] concludes that the use of RF is much safer than DC but that DC ablation is more effective for the production of atrio-ventricular block. It is likely that the better efficiency of DC be due to the larger size of the lesions produced. In that sense the localized nature of RF lesions is a drawback and may necessitate a better positioning of the electrode.

2.3 Conclusion

This chapter shows the evolution of the catheter ablation technique for the treatment of cardiac diseases. As mentioned, the use of RF energy requires relatively simple equipment and procedures and yields good results. Today, it is used practically on a routine basis to cure certain types of arrhythmias. However, for ablation on the ventricular walls, the lesions produced by RF current are still too small.

Radio-frequency ablation presents definite advantages over laser and DC respectively in terms of simplicity and safety. The main limitation of RF ablation is the small size of the lesions. Paradoxically, it seems that little consideration has been devoted to improve this situation. A possible reason may be the relative command of the technique in the clinical setting which may be considered to give optimum results already. Nevertheless, from the engineering point of view, the optimization of RF catheter ablation deserves further studies.

Microwave ablation has recently been proposed as an alternative which could potentially produce larger lesions. No in-depth development work has been reported so far on this new approach. Preliminary results [62] are not sufficient to confirm whether larger lesions can be created. Major problems of catheter flexibility and loss are foreseeable since very thin coaxial catheters must be used for this application.

Unipolar ablation is by far the most common mode used today for RF ablation. Accordingly the research focuses on this mode of operation.

Chapter 3

Theoretical Modeling I: Description

This chapter presents the model used in the theoretical studies. It is divided into two sections. The first one presents the model itself, how it relates to the physical situation, and the differential equations that govern it. It ends with a presentation of the material properties of interest in this study. The second section of this chapter presents the numerical treatment of the model: the numerical method used, the software developed for the application and its validation by comparisons with known solutions.

3.1 The Model

This section presents a model of RF ablation that is amenable to numerical analysis and yet reasonably representative of the reality. The physical environment encountered during the ablation treatment is first described. This provides the justification for the choice of the particular model used in the study and presented in the following subsection.

The goal of the modeling process is to calculate the lesion produced in the tissue under various conditions of ablation. In order to do that a thermal damage function based on the history of the tissue temperature must be defined. This function is presented in the third subsection. Finally, the model is not complete until the actual values for the physical properties of its components are determined. A review of the thermal and electrical properties of biological tissues is thus presented in the last subsection.

3.1.1 Description of the Physical Situation

During RF transcatheter ablation an electrode catheter is introduced inside the heart and moved until it is in contact with the area to be ablated. This is a difficult task because the heart is a complex environment with an irregular shape and moving parts (Fig. 2.4, p. 11). In practice, the catheter tip is wedged in one of the many wrinkles of the endocardium and maintained there by exerting a pressure on it. The electric current is then applied between the catheter electrode and an external grounded electrode to produce a local burn. The external electrode is large in order to avoid skin burns and should be positioned to optimize current flow through the target area. The electric current should be such that the tissue temperature does not exceed 100°C. Indeed, this is undesirable because charring and boiling occur, producing a sharp rise in the resistance and limiting lesion progression [47, 50]. A maximum duration of power application of 1 to 2 minutes is achievable in practice. Frequencies of 500 to 1000 kHz are used most of the time for the electrical excitation. These frequencies are both high enough to avoid the undesired stimulation of nerves and muscle, and low enough to allow easy and efficient coupling of energy to the tissues.

The lesion produced by RF ablation is entirely dependent on the thermal process taking place at the point of contact of the catheter electrode and the endocardium. The source of heat is the electric current through the tissue which depends strongly on the electrode-tissue configuration, and on the applied voltage, the tissue properties, and the position and size of the external electrode. Unfortunately, catheter positioning is not easily repeatable, and the actual electrode-tissue configuration cannot be controlled at will. The situation is globally so complex that important simplifications must be made to allow any analysis.

3.1.2 Description of the Model

The first step towards the definition of an appropriate model is to limit the number of variables to be dealt with. Of course, those variables that *can be controlled* during RF ablation must remain. Accordingly, the study is limited to the case where the catheter comes in contact with the tissue at right angle, and tissue heterogeneity is neglected. The inclusion of these two aspects in the model would necessitate a 3-D analysis with a large number of input data. Since most of the data on the detailed geometry is absolutely uncontrollable and highly case dependent, no meaningful conclusions could ever be drawn from such an analysis.

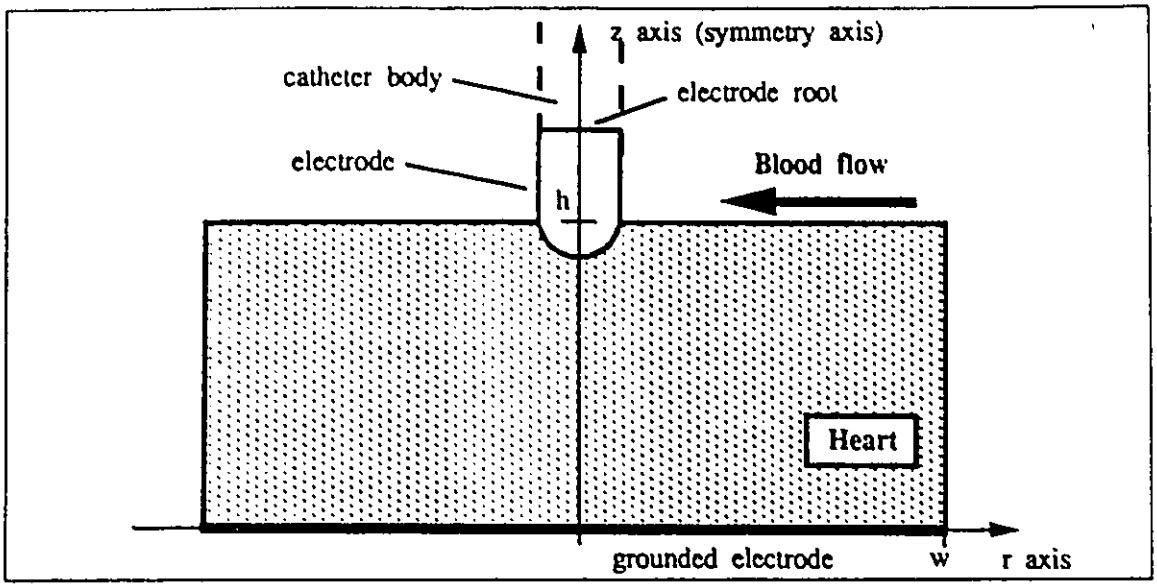

Figure 3.1: Proposed model. Axial symmetry is present so only the right half is considered in the simulations.

The proposed model (Fig. 3.1) consists of a slab of homogeneous tissue with blood flowing on one side (the endocardium) and a large grounded plate on the opposite side. The two sides are assumed parallel. Axial symmetry is present so that the problem is two-dimensional. The tip of the catheter electrode touches the endocardium at right angle. In practice, the size and geometry of the electrode are known. On the other hand, the depth of penetration inside the tissue is not controllable during the intervention and is *a priori* unknown. Despite its limitations, this model is much more realistic than the one considered previously by Haines [45][1]

The lesion produced in the tissue is of a thermal nature and is a function of the temperature distribution which is to be evaluated. Heat transfer mechanisms present in biological tissues include conduction, convection, metabolic heat generation, storage of thermal energy and absorption of energy from external sources. In principle, the effects of all these processes can be combined in the *bio-heat equation*, to obtain the resulting tissue temperature. In practice, in order to limit the complexity of the model and in the absence of detailed and accurate data quantifying the various mechanisms, some simplifications are made for the heat transfer problem.

[1] Steady-state, one-dimensional, no blood.

The first one concerns the blood perfusion. The significance of this factor is not clear in the context of tissue ablation. Reported experimental work concludes that the intramyocardial blood flow does not contribute significantly to the cooling of the ablated area [45]. One possible explanation is the occlusion of the micro-vasculature in the heated area by blood coagulation. Another one is the existence of high thermal coupling between afferent and efferent circulation, so that the perfusing blood is at thermal equilibrium with the surrounding tissue with no net exchange of heat between them [63]. In view of this, blood perfusion is not considered in this study. Similarly, the metabolic heat generation is also neglected. Metabolic heating is a determinant factor of tissue baseline temperature but not particularly significant for hyperthermia applications [64]. It can *a fortiori* be neglected in ablation studies where the heating is much shorter in duration and is applied over a much smaller area.

With the above simplifications, the temperature distribution can be found by solving the heat conduction equation,

$$\rho c_p \frac{\partial T}{\partial t} = \nabla \cdot k \nabla T + q \tag{3.1}$$

where the following quantities are used:

$$\begin{aligned}
\rho &= \text{density } (\text{kg m}^{-3}), \\
c_p &= \text{specific heat } (\text{J kg}^{-1}\,^{\circ}\text{C}^{-1}), \\
T &= \text{temperature } (^{\circ}\text{C}), \\
t &= \text{time } (\text{s}), \\
k &= \text{thermal conductivity } (\text{W m}^{-1}\,^{\circ}\text{C}^{-1}), \\
q &= \text{heat source } (\text{W m}^{-3}).
\end{aligned}$$

Only the temperature increase with respect to the basal temperature is responsible for the lesion production. So without loss of generality it will be assumed throughout that the basal temperature is 0°C instead of 37°C.

The source of heat q in the above expression is the Joule loss due to the electric current which must be calculated. This is relatively simple because at the frequencies of interest the quasi-static approximation is valid and the capacitive nature of the materials can be neglected (see Appendix A). The electric source is the RF voltage (RMS) imposed between the electrodes which may vary with time. The resulting voltage throughout the domain obeys

Laplace's equation:

$$\nabla \cdot \sigma \nabla V = 0 \tag{3.2}$$

where

$$\begin{aligned} \sigma &= \text{electrical conductivity } (\text{S m}^{-1}), \\ V &= \text{electric potential } (\text{V}). \end{aligned}$$

Hence, to determine the extent of the lesion in the model, one must first solve (3.2) in order to obtain the potential distribution. The distributed heat source is next calculated with

$$q = \sigma \cdot (\nabla V)^2.$$

Then (3.1) is solved for the temperature distribution. The heat conduction and Laplace's equations are formally similar to the following,

$$F(\phi) = \nabla \cdot P \nabla \phi + Q \frac{\partial \phi}{\partial t} + \psi = 0, \tag{3.3}$$

which will be considered as a generic equation in the remaining of the formulation.

Boundary Conditions

The boundary conditions remain to be defined (Fig. 3.1). First consider the electrical problem. The electrodes constitute Dirichlet boundaries where the voltage is fixed. The vertical boundary at $r = w$ will be considered as a Neumann boundary, which means that no current flows through it. Its location must be chosen adequately in order to be a reasonable representation of the RF ablation process. In the human body, the volume available for current flow is large but the current density is by far the highest in the immediate neighborhood of the catheter electrode. The model needs to reflect this situation with global dimensions as small as possible to limit the number of unknowns. The choice of the boundary location is discussed in Chapter 5. Finally, the horizontal boundary on the blood side must be determined. A Neumann condition will be enforced there because it is more realistic than a Dirichlet condition. However the location of the NBC must be chosen carefully. The obvious choice of the heart-blood interface ($z = h$) may not be adequate because of the effect it may have on the current distribution at the electrode tip. The issue is further studied in Chapter 5.

For the thermal problem the situation is the following. At the heart-blood and catheter-blood interfaces, heat is lost by convection to the moving blood. This is a *convective boundary*, where the temperature obeys

$$\nabla T \cdot d\vec{S} = h\,k^{-1}(T_0 - T) \tag{3.4}$$

with h the heat transfer coefficient, k the conductivity of the solid and T_0 the fluid temperature. In our case, it is reasonable to assume that the blood temperature is constant because the flow is high so that thermal equilibrium with the body is maintained. An approximation for the convection coefficient $h \approx 2000$ W m^{-2} °C^{-1} is obtained with the expression for a laminar flow over a flat surface (Appendix B). Considering that the situation is highly complex with variable flow, this assumption seems reasonable as a first approximation. The situation at the electrode root (junction between the electrode and the catheter body) is not well defined and is treated in Chapter 5. On the other boundaries the temperature is considered to be constant (Dirichlet condition).

Summary

The proposed model includes a number of significant factors affecting lesion formation:

1. electrode geometry and depth,
2. blood flow,
3. time-variable electrical excitation,
4. temperature-dependent tissue properties,

In order to be tractable, the model is a simplification of the reality of RF ablation. The major simplifications are:

1. Axial-symmetry is assumed therefore the model is two-dimensional.
2. The electrode catheter touches the tissue at right angle.
3. A close mechanical and electrical contact exists between electrodes and tissue.
4. The blood perfusion in the tissue is neglected in the heat transfer equation since its significance is doubtful.

5. The approximation for laminar flow over a flat surface is used to estimate the heat transfer coefficient at the blood interfaces.

6. Biological material is isotropic and piecewise homogeneous.

7. Material properties are independent of temperature, except the electrical conductivity (see section on material properties)

8. Material properties are independent of state of tissue (burnt or intact).

The proposed model allows the quantification of many aspects of RF ablation which have been unknown up to now:

- influence of the blood flow,
- temperature distribution,
- lesion size and sharpness,
- transient evolution.

Furthermore, this theoretical model provides a convenient standard against which experimental results can be compared.

3.1.3 Thermal Damage Factor

The amount of thermal damage produced to living tissues is a function of both the elevation of temperature and the duration of exposure [65, 66, 67]. A chemical process behaving in this way is a *chemical rate process*. The basic postulate of the analysis of thermal damage is that the degree of injury suffered by the tissues can be predicted by the standard expression for a chemical rate process

$$\Omega = P \int_0^t e^{-\Delta E/RT} dt, \tag{3.5}$$

where

Ω	=	arbitrary thermal damage function,
P	=	constant related to the definition of Ω (s^{-1}),
ΔE	=	activation energy of the process: a measure of the energy requirement for the chemical reaction to take place (J mol^{-1}),
R	=	ideal gas constant, 8.315 (J mol^{-1} K^{-1}),
T	=	temperature (K),
t	=	time (s).

T (°C)	t (s)
44	21500
45	10700
50	344
52	89
60	0.5

Table 3.1: Table showing the time necessary to produce irreversible damage to tissue when the temperature is constant.

P and ΔE have been evaluated by curve fitting to experimental data for pig and human skin published in [65, 66, 67] and the values we obtained[2] are:

$$P = 2.3921 \cdot 10^{92}\ \mathrm{s}^{-1},\ \text{(yes, ten to the ninety-two!)}$$
$$\Delta E = 5.8694 \cdot 10^{5}\ \mathrm{J\ mol}^{-1}.$$

The value of P depends on the arbitrary choice that for $\Omega \geq 1$ irreversible damage is obtained. It is also found experimentally that tissue damage is reversible when $\Omega \leq 0.5$. For instance, assuming that the temperature is constant, the time before irreversible damage is produced varies as shown in Table 3.1. These figures correspond to cell damage due to protein denaturation [65].

The rate equation is used in the model to calculate the lesion size and sharpness during ablation. The coefficients cited above are used since no reports have been found specifically for heart tissue. The problem of defining what an irreversible lesion is in the context of ablation has not been investigated because it is not within the scope of this work. It is possible that other mechanisms than protein denaturation can lead more rapidly to the loss of functionality of myocardial cells. This would mean that the lesions calculated in this work may be slightly smaller than the real ones.

3.1.4 Material Properties

In order to be representative of the reality, the various components of the model must be attributed the same physical properties as those of the real tissues they stand for. The

[2]The values of ΔE and P used here do not correspond exactly to those proposed in [65] but we find that they provide a better fit to the experimental data.

problem here is that for a given biological material, the thermal and electrical properties can exhibit a relatively large variability from animal to animal or even sample to sample ($\pm 10\%$). Therefore one must realize and accept the inherent inaccuracy of any calculation made for biological materials.

This section contains a summary of the electrical and thermal property values of biological materials found in the literature. Averages of the published values are used in this study. As our application involves the heating of the tissues, the temperature dependence of tissue properties becomes an important issue. It is found that the variation of the electrical conductivity with temperature can be significant and should be taken into account.

Electrical Properties

An overview of the abundant literature on the electrical properties of biological materials is given here. Good reviews can be found in [68, 69].

The response of a material to an applied electric field involves the physical displacement of charges. The movement of bound charges produces electric dipoles and establishes a polarization inside the material. From a macroscopic point of view, the polarization is advantageously considered by using the concept of relative permittivity ϵ, relating the applied electric field and the resulting electric displacement, $\bar{D} = \epsilon_0 \epsilon \bar{E}$.

Since all polarization mechanisms require the displacement of particles each having a mass, it is clear that the strength of polarization must decrease with frequency. That is, a particle's inertia prevents it from following the oscillations of the applied field so that the material polarization and the applied electric field are not in phase. In phasor notation, the permittivity becomes a complex value

$$\epsilon = \epsilon' - j\epsilon''.$$

The real part of the permittivity is referred to as the dielectric constant. Its imaginary part is associated with power loss which is macroscopically indistinguishable from the loss due to the movement of free charges. ϵ'' can be related to an apparent conductivity σ by

$$\epsilon'' = \frac{\sigma}{\omega \epsilon_0}.$$

The real and imaginary parts of the permittivity cannot vary independently with frequency and, accordingly, the frequency dependence of ϵ' determines that of σ and conversely. Any

decrease with frequency in ϵ' must be accompanied by an increase in σ (Kramers-Kronig relations).

In biological materials, several different polarization mechanisms exist. The main ones behave as relaxation processes. That is, the polarization exponentially relaxes towards its steady-state value in response to a step in the applied electric field. As a function of frequency, a given relaxation process is characterized by a sudden drop in the magnitude of ϵ' at the so-called *relaxation frequency*. The portion of the spectrum where this occurs is called the dispersion range of the relaxation process. At frequencies well below and far above the dispersion range, the permittivity is relatively constant. The three polarization mechanisms mainly responsible for the dielectric properties of tissues are:

1. interfacial polarization,

2. orientational polarization and,

3. counterion polarization.

Interfacial polarization arises at the interfaces between the various phases in the tissue such as cell membranes. Orientational polarization is the partial rotation of permanent dipoles. Finally the third class of phenomena arises from ionic diffusion in the double layers adjacent to charged surfaces. In biological tissues, counterion effects are prominent at audio frequencies, while the effects of interfacial and orientational polarization are more pronounced at radio frequencies. Due to their complex nature, the frequency behavior of biological materials typically displays 3 or 4 more or less distinct dispersion regions. They are called the α, β, γ and δ dispersions, and their basic mechanisms can usually be identified in terms of those mentioned above. The frequency dependence of the dielectric properties of heart tissue is shown in Figure 3.2.

In addition to frequency, dielectric properties also vary with temperature. The magnitude of this variation depends on the frequency in a somewhat complicated way [69]. For ϵ' the temperature coefficient varies with increasing frequency through the dispersion range from about $-0.3\%\,^{\circ}C^{-1}$ to a maximum of $+2\%\,^{\circ}C^{-1}$ and back to around $-0.3\%\,^{\circ}C^{-1}$. The coefficient of the conductivity is in the order of $+2\%\,^{\circ}C^{-1}$ (same as simple electrolytes) for all frequencies when a tissue presents overlapping dispersions. This temperature coefficient appears significant in a study like this one and will be considered.

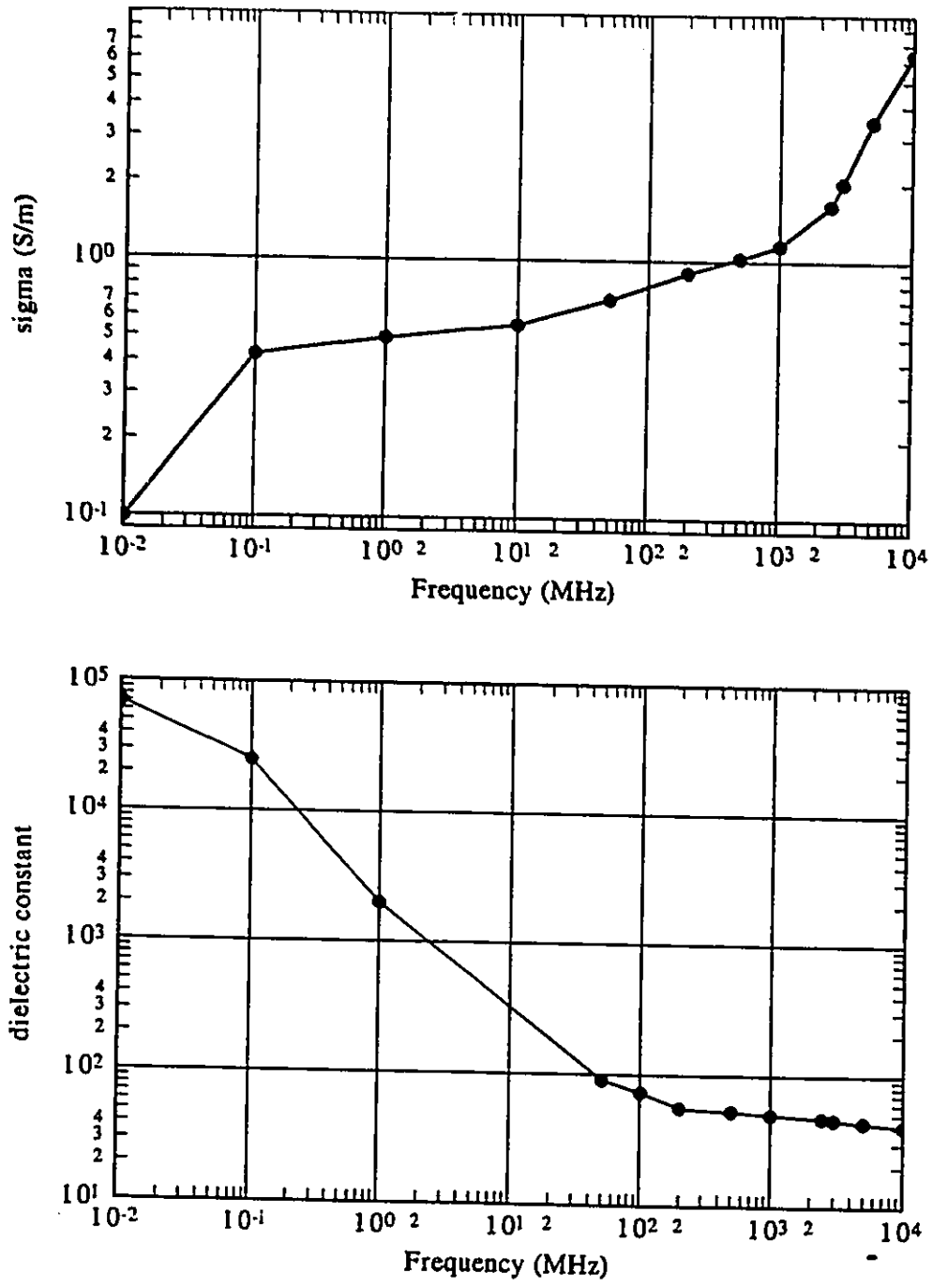

Figure 3.2: Frequency dependence of the dielectric properties of heart tissue, from [70].

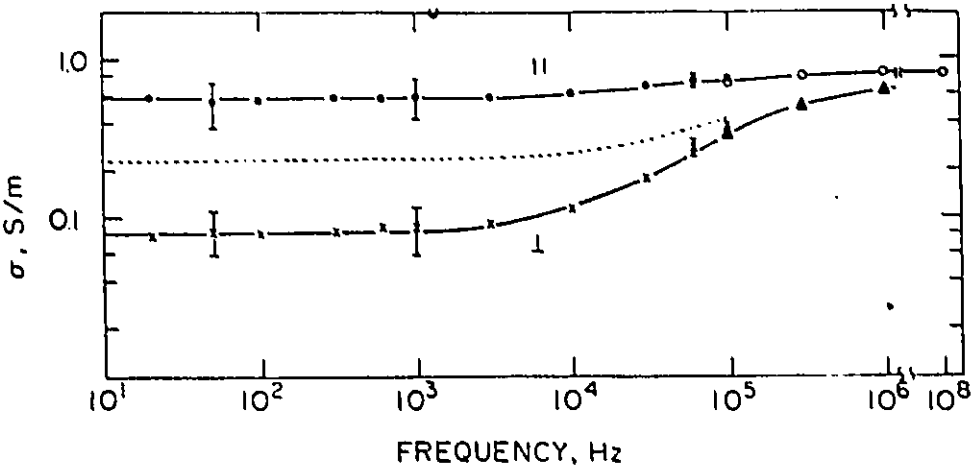

Figure 3.3: Conductivity of dog skeletal muscle in directions normal and parallel to the fibers, from [68, Fig. 7C, p. 59].

Many tissues exhibit an important anisotropy in their dielectric properties due to the preferential orientation of their constituent fibers. This anisotropy is predominant at low frequencies and gradually disappears with increasing frequency. It may persist to some degree even at microwave frequencies. Figure 3.3 shows the conductivity of dog skeletal muscle in directions parallel and perpendicular to the fibers. In this case, anisotropy disappears above 1 MHz. Anisotropy is neglected in this study.

Living biological tissues present an additional difficulty. Their dielectric properties differ from those of post-mortem or excised tissue. The breakdown of cellular structure and membrane functions, ion migration and loss of moisture contribute to those changes. The deterioration of the properties occurs faster after excision and is much more pronounced at low frequencies, where cell membranes play a significant role, than at radio frequencies where the water and protein content are the major determinant factors. If care is used in the handling of tissue samples and especially if water content is maintained, the properties measured within a few hours after excision are similar to the in-vivo data, within the animal-to-animal variability [71].

Thermal Properties

The ability of a material to transport thermal energy is expressed by its thermal conductivity k. The specific heat c_p characterizes the ability to store energy by an elevation of temperature. Whereas theories of thermal transfer in solids are available to predict their thermal properties, it is not the case for liquids and even less so for complex biomaterials. Accordingly, there seems to be much less literature treating the thermal properties of biomaterials than their electrical counterparts. Good reviews are presented in [63, 72].

The reported data on thermal conductivity exhibit a relatively large degree of scatter due to measurement technique, normal tissue variability, anisotropy and state (in-vitro vs in-vivo). No explicit data for the temperature dependence of the thermal properties of biological materials was found. However the data for water are available and should be representative of tissues for high-water content. In [73] we find that between 40 and 100°C, the thermal conductivity of water varies less than 8%, the density less than 4% and the specific heat is practically constant. In view of this, the temperature dependence of the thermal properties is neglected in this study.

Tissue Properties, Tabulated

Table 3.2 shows the published values for the properties of various tissues of interest in this study. The values are given at a frequency of 1 MHz and a temperature of 37°C. Averages of the published values are used in this study and are indicated. All properties are considered to be independent of temperature except the electrical conductivity which has a coefficient of $+2\%\ °C^{-1}$. The properties of burnt tissue (below 100°C) is assumed to be the same as for intact tissue because no reliable data is available for it. As can be seen in the table, the electrical properties of lung and heart are similar which justifies the use of a homogeneous model. The properties of Platinum, which electrodes are made of, are also indicated.

3.2 Numerical Analysis

3.2.1 Numerical Method

This section briefly explains the mathematical treatment of the differential equations governing our model. Only a conceptual description is given here. More details are presented

k W m^{-1} °C^{-1}	ρc_p kg m^{-3} J kg^{-1} °C^{-1}	σ S m^{-1}	ϵ'	comments
FAT at 37°C				
		0.02–0.07		[68] dog fat at 1 kHz, excised human tissue at 27°C
0.1–0.4	$0.4 \cdot 10^6$			[63] fat
0.2				[72] human fat
0.22				[74] human fat in-vitro
0.2	$0.4 \cdot 10^6$	0.05		**used in this study**
BLOOD at 37°C				
		0.95	2700	[70] rabbit blood at 23°C extrapolated to 37°C with +2% °C^{-1}
0.5–0.6				[63] body fluids
0.5				[72] human blood (average)
0.48				[74] human blood
0.55	$4.0 \cdot 10^6$	0.95	2700	**used in this study**
LUNG at 37°C				
		0.56–0.67		[70] human lung
0.26				[72] bovine and canine average
0.478				[74] human in-vitro varies much with age
0.3	$4.0 \cdot 10^6$	0.6		**used in this study**
LIVER at 37°C				
		0.23	2000	[75] human liver
		0.2–0.4	2000	[71] cat liver
		0.27	1300	[76] bovine liver
		0.22–0.47	1200–2000	[70] human liver
		0.31–0.62		[77] human liver
		0.27–0.3	1970	[68] dog and rabbit liver
0.4–0.6	$1.8 \cdot 10^6$–$4 \cdot 10^6$			[63] internal soft tissues
0.6	$3.75 \cdot 10^6$			[72] canine liver, average
0.51				[74] human, in-vitro
0.5	$3.75 \cdot 10^6$	0.35	2000	**used in this study**

Table 3.2: Material properties at 1MHz (continued next page).

k W m^{-1} °C^{-1}	ρc_p kg m^{-3} J kg^{-1} °C^{-1}	σ S m^{-1}	ϵ'	comments
HEART at 37°C				
		0.53	1245	[75] human heart
		0.6–0.8	2000	[71] cat muscle
		0.63		[70] human, minced
		0.65–0.79		[77] human skeletal muscle
		0.58–0.63	1900–2150	[68] non-oriented dog muscle
0.4–0.6	$1.8 \cdot 10^6$–$4 \cdot 10^6$			[63] human, internal soft tissue
0.7–1.0				[63] muscle in-vivo
0.48	$3.2 \cdot 10^6$			[72] dog heart
0.59	$4 \cdot 10^6$			[72] human heart
0.49	$3.4 \cdot 10^6$			[72] sheep heart
0.2–0.6				[72] human and animal muscle
0.53				[74] human in-vitro
0.7	$3.9 \cdot 10^6$	0.61	2000	**used in this study**
Platinum				
73	$2.8421 \cdot 10^6$	$9.4 \cdot 10^6$		[73]
TEM at 22°C				
0.6	$4.18 \cdot 10^6$	0.61		Chapter 4 from 1.5 to 1000 kHz.

Table 3.2: (continued) Material properties at 1MHz.

in Appendix C. The formulation relies on the finite-element method (FEM) to discretize the spatial domain and a finite-difference algorithm to resolve the time dependence.

The differential equations to be solved are of the generic form (Eq. (3.3))

$$F(\phi) = \nabla \cdot P\nabla\phi + Q\frac{\partial\phi}{\partial t} + \psi = 0. \tag{3.6}$$

Depending on the values of P, Q, ϕ and ψ, this generic differential equation is used to calculate the electrical potential V or the temperature T. For the electrical problem,

$$\begin{aligned} \phi &= V \ (\mathrm{V}) \\ P &= \sigma \ (\mathrm{S\ m^{-1}}) \\ Q &= 0 \\ \psi &= 0 \end{aligned}$$

and for the thermal problem,

$$\begin{aligned} \phi &= T \ (^{\circ}\mathrm{C}) \\ P &= k \\ Q &= -\rho c_p \ (\mathrm{kg\ m^{-3}})(\mathrm{J\ kg^{-1}\ ^{\circ}C^{-1}}) \\ \psi &= q \ (\mathrm{W\ m^{-3}}). \end{aligned}$$

Since biological material can be considered piecewise homogeneous, $F(\phi)$ can be rewritten:

$$F(\phi) = P\nabla^2\phi + Q\frac{\partial\phi}{\partial t} + \psi = 0.$$

The solution consists in finding an approximate solution ϕ', element of a suitable function space $\mathcal{F}_1$, that minimizes $F(\phi')$. The idea is to chose $\mathcal{F}_1$ large enough, so that ϕ' is reasonably close to ϕ. One possible way[3] to minimize the residue $F(\phi')$ is to force it to be orthogonal to all the elements of a function space $\mathcal{F}_2$, according to a suitable inner product

$$< a\,,\, b > = \int_V ab\, dV.$$

Suppose β_q is a set of functions spanning $\mathcal{F}_2$. Then the minimization takes the form:

$$< F(\phi'), \beta_q > = \int_V P\beta_q\nabla^2\phi' + Q\beta_q\frac{\partial\phi'}{\partial t} + \psi\beta_q\, dV = 0.$$

[3]An alternative is to force the residue to be zero at a number of predetermined points. It is the collocation method but its accuracy is very dependent on the location of the collocation points. It is in general less accurate than the method proposed here.

The first term can be developed by Green's theorem as follows:

$$\int_V P\beta_q \nabla^2 \phi' \, dV = P \oint_S \beta_q \nabla \phi' \cdot d\vec{S} - P \int_V \nabla \beta_q \cdot \nabla \phi' \, dV.$$

This constitutes a significant simplification because the admissible ϕ' need only be differentiable once in space instead of twice as before (∇ operator instead of ∇^2). What this means is that a larger set of functions $\mathcal{F}_1$ for the expansion of ϕ' can be used, including linear functions. Rewriting we get

$$P \oint_S \beta_q \nabla \phi' \cdot d\vec{S} - P \int_V \nabla \beta_q \cdot \nabla \phi' \, dV + \int_V Q \beta_q \frac{\partial \phi'}{\partial t} + \psi \beta_q \, dV = 0. \tag{3.7}$$

In our case, axial symmetry applies and the space becomes a plane (r–z). This plane is discretized into NN nodes forming NTR triangles. The next step consists in expanding

$$\phi' = \sum_{i=0}^{NN-1} u_i(t)\, \alpha_i(r,z)$$

where the α_i's constitute a suitable basis for $\mathcal{F}_1$. With the Galerkin procedure ($\mathcal{F}_1 = \mathcal{F}_2$, $\beta_q = \alpha_q$) Eq. (3.7) is transformed into a set of ODE's in $u_i(t)$ and $d\,u_i(t)/dt$:

$$\langle \mathrm{A} \rangle \langle \mathrm{u}(t) + \langle \mathrm{B} \rangle \langle \frac{d\mathrm{u}(t)}{dt} + \langle \mathrm{C}(t) = 0,$$

where matrix notation has been used. The last term represents the source in the generic differential equation. To transform the above ordinary differential equations into a set of algebraic equations, the time variables are discretized using a finite-difference scheme. With it, those variables are expressed in terms of their values at $t = n\,\Delta t$ (current value) and $t = (n+1)\Delta t$ (unknown). It is called a time-stepping scheme. The final system of equations has the form

$$\langle \mathrm{D} \rangle \langle \mathrm{u}^{(n+1)} = \langle \mathrm{E} \rangle \langle \mathrm{u}^{(n)} + \langle \mathrm{F}^{(n)} + \langle \mathrm{F}^{(n+1)}$$

where the last two terms represent the source at the current and the coming time step.

The source terms are dropped when solving an electrical problem, but must be considered when dealing with the heat equation. In this case the source varies with time in two different ways. First, when the applied voltage is modulated, its *magnitude* varies accordingly. Secondly, because of the temperature dependent electrical conductivity, both the *magnitude* and the *distribution* of the heat source become time-dependent. In the first case, $\langle \mathrm{F}^{(n+1)}$ is

simply obtained from $\langle \mathbf{F}^{(n)}$ by multiplication with a scalar modulation factor related to the magnitude of the voltage. In the second case, the problem becomes non-linear and we need to know $\langle u^{(n+1)}$, the temperature itself at the coming time step, in order to calculate $\langle \mathbf{F}^{(n+1)}$. This difficulty is resolved by assuming that the distribution of the heat source at the next time step is almost the same as the current one. After $\langle u^{(n+1)}$ is calculated, the distributed heat source is updated by solving the electrical problem and time-stepping can proceed in this fashion.

Concerning the thermal damage factor, its value is updated at each time step according to the discretized form of (3.5) on p. 29:

$$\Omega(N) = \sum_{n=1}^{N} \frac{2.3921 \cdot 10^{93}}{e^{2\Delta E/R(T^{(n)}+T^{(n-1)})}} \Delta t.$$

This is a concise presentation of the mathematical treatment. The details of the formulation are included in Appendix C for reference.

3.2.2 Software Validation

The program implementing the above mathematical formulation is developed in the C language. The nature of the particular problem to be solved is specified at run time by initializing the equation parameters to the appropriate thermal or electrical values. Validation of the program is done by comparing its results to the known solutions of a number of simple problems. The electrical and the thermal calculations are verified independently, on *uncoupled* problems. The problems considered all deal with homogeneous material.

To verify the ability of the program to handle electrical simulations the resistance between pairs of conductors in various configurations are calculated. In all cases, namely two concentric cylinders, two parallel disks, two parallel rings and two concentric spheres, the numerical calculations are within fractions of 1% of the analytical values. This strongly suggests that both the voltage and the Joule loss calculations are correct.

Analytical solutions to many simple thermal problems can be found in [78]. In particular, those used to test the program are

1. 1-D, rectangular coordinates, constant heat source, Dirichlet boundary conditions, steady-state, (p. 17),

2. 1-D (along z) in cylindrical coordinates, no source, both convective and Neumann boundary conditions, steady-state, (p. 18),

3. 1-D, rectangular coordinates, no source, Dirichlet boundary conditions, transient, (p. 77),

4. 1-D (along r) in cylindrical coordinates, no source, Dirichlet boundary conditions, transient, (p. 116),

5. 1-D (along r) in cylindrical coordinates, no source, convective boundary conditions, transient, (p. 77, 95, 121)

In all these problems the numerical solutions agree very well (typically everywhere within 2%) with the analytical solutions.

The problem of transient heat transfer between two concentric spheres is also considered. This is a one-dimensional problem in spherical coordinates that can be handled by the program. The numerical solution is compared to a solution obtained with another numerical method, the finite-difference time-domain method, which is particularly simple to implement in this case. As before the agreement is excellent.

The valid solutions produced by the program in the various cases studied here demonstrate its reliability. Obviously, the finer the FEM mesh and the smaller the time step that are used in the numerical calculation, the more accurate the results. The problems considered here are simple because they are uncoupled and without non-linearities. This is quite different from the situations of interest in this study. The next chapter presents an experimental confirmation of the computer simulation with coupling of the electrical and the thermal problems.

Associated Software

It is clear that apart from the main FEM program necessary for this study, a number of utility programs need be developed. In a research like this one where analysis is conducted on many different configurations, it is essential to have a good automatic mesh generator. One was developed in the course of this work, using the algorithm proposed in [79]. Together with a graphical mesh editor which was also developed for this research, it proved to be

very versatile, fast and easy to use. Another program for the color display of 2-dimensional temperature distributions written with X Window, also proved very useful in this work. The development of the software tools represents a significant portion of the total effort spent on this project.

3.3 Conclusion

In this chapter the model used in this research is presented and justified. Its geometry, the material properties and the differential equations governing it are outlined. The mathematical treatment is also succinctly presented. Finally, the software developed for the application is validated with simple problems. For clarity many details of the mathematical formulation are omitted. They can be found in Appendix C.

At this point we have a numerical simulator for the study of ablation. Before going too far with the modeling work, and to get a feeling for the degree of accuracy achieved by the simulations, we felt necessary to verify experimentally the results of a relatively complex simulation. This is done in the following chapter.

Chapter 4

Experimental Validation of the Software

This study of radio-frequency ablation of the myocardium relies heavily on the numerical modeling software presented in Chapter 3. It is therefore of paramount importance to ensure its validity. To this end, a series of experiments with a complexity that is close to that found during RF ablation is undertaken. The agreement between the calculated and the measured time-dependent resistance and temperature distributions is found to be good. This confirms the applicability of the simulator to the problem of RF ablation.

This chapter describes the experimental apparatus and procedures. Their conception and realization were performed entirely during the course of this research.

4.1 Objectives

Experimentation is conducted in order to verify the capacity of the numerical simulator described in the previous chapter to handle correctly the proposed model of RF ablation, and to assess the degree of agreement between the reality and the theoretical results. Specifically, an experiment is designed in which the temperature distribution obtained inside the tissue during ablation and the resulting time-dependent resistance are measured and compared with theoretical values.

4.2 Materials and Methods

The experiment is a reproduction of the RF ablation procedure performed on a simple tissue model. The tissue model is made of tissue-equivalent material instead of biological tissue

for reasons of convenience and repeatability and relatively accurate knowledge of its physical properties. The experiment consists in applying a pre-programmed electrical discharge at the tip of an ablating electrode in contact with the tissue model. A large grounded electrode is located on the other side of the material specimen. The value of the resistance between the two electrodes is calculated, based on voltage and current measurements made in real-time during the procedure. Because of the relatively small extent of the heated volume, the temperature distribution inside the material cannot be measured with conventional temperature probes. The only reliable method for rapid and accurate measurement of temperature distributions in these circumstances is a thermographic camera. This device performs the measurement of the *surface temperature* of an object. Consequently, the heated specimen must be opened up in order to expose a cross-section of the 3-D temperature distribution. The experimental measurements of temperature and resistance are compared with theoretical predictions which are easy to make with the simulator because the experimental conditions are well known.

4.2.1 Experimental Set-up

The experimental arrangement is shown in Fig. 4.1. It consists of a computer-controlled electrical generator with output voltage and current monitoring, stainless steel electrodes (one for ablation and one acting as ground plate and mechanical support), the tissue model ($88 \times 88 \times 44$ mm^3) and a thermographic camera. The tissue model and the supporting plate are made of two parts that can be rapidly separated, in order to allow exposure of a cross-section of the heated volume. The arrangement is such that the plane of separation is centered under the ablating electrode. Therefore, the exposed surface is a vertical plane containing the symmetry axis of the temperature field. Films of polyethylene (≈ 20 μm thick) are laid on the faces between the two parts in order to facilitate their separation. Because of the symmetry, they are not expected to interfere with the electrical and thermal processes. Small parts of the films covering the heated area are cut out so as not to disturb the temperature reading. The ablating electrode is installed on a sliding plate that can be moved up and down accurately using a micrometer. Two ablating electrodes are considered in these experiments: a flat-tip electrode and a hemispherical-tip electrode. They both have a diameter of 2.5 mm at their tip. A heated vernier caliper is also positioned in the field of view of the camera. It constitutes a reference for the measurement of length on the final

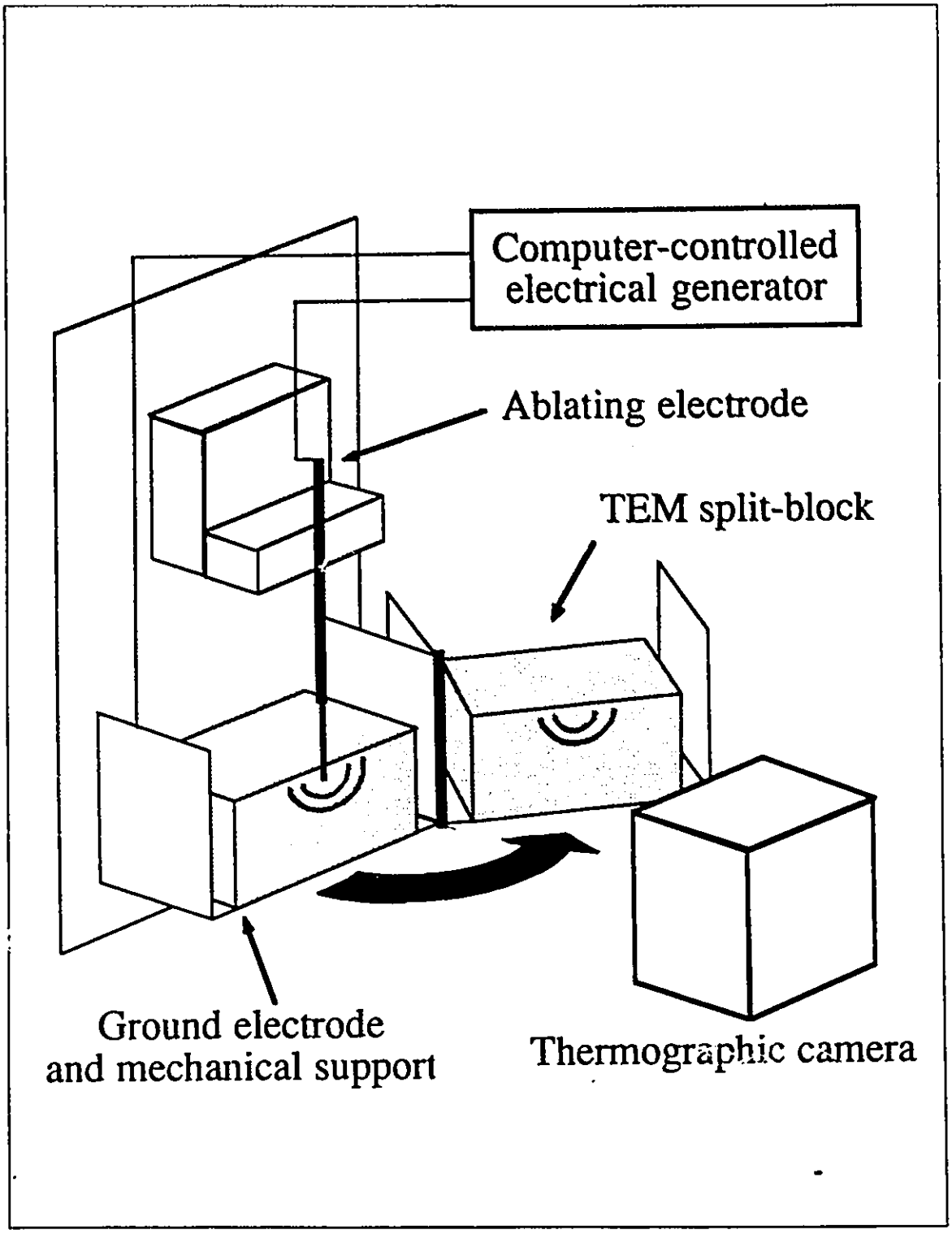

Figure 4.1: Experimental set-up.

temperature picture.

During the experiment, a pre-programmed RF voltage sequence is applied between the ablating electrode and the ground plate. The output current and voltage are continuously monitored and recorded by the computer for later use. After the heating sequence is terminated, the split block model is rapidly opened up, typically within one second. A cross-section of the heated area is thus exposed and the temperature distribution can be recorded by the camera (scanning takes slightly more than one second to complete). The camera output is digitized, displayed on a color monitor and stored on disk for post-processing. Unavoidable cooling by conduction, convection and water evaporation occurs between the end of the heating sequence and the completion of the camera scan. It is minimized by acting as fast as possible to expose the heated area. Nevertheless, this factor must be taken into account in the interpretation of the measured temperature distributions.

4.2.2 Tissue-Equivalent Material

In this experiment tissue-equivalent material (TEM) is used instead of real biological tissue for reasons of convenience and repeatability of the properties. The particular difficulty is that the material must be very viscous, so that it can be molded into a shape that is appropriate to the measurement to be made. Also, it must be able to withstand temperatures up to 60°C without liquefying. The TEM formulation is based on that suggested in [80]. It consists of saline with a gelling agent to increase the viscosity.

The TEM is prepared so as to possess at room temperature the same electrical conductivity as heart tissue at 37°C (σ = 0.61 S m^{-1}, Table 3.2, p. 36). As mentioned earlier, at frequencies lower than 1 MHz the dielectric constant can be neglected. Expressions relating salinity and temperature to the conductivity of saline [81] are used to provide some guidance in the empirical development of the TEM formulation.

To measure the electrical conductivity of the highly viscous gel a special conductivity cell had to be devised. It consists of a cylindrical plexiglass tube with a stainless steel plate electrode closing both ends. By measuring the resistance between the electrodes, the conductivity of the material inside can be calculated, provided the dimensions of the cell are known. In this case the length l is 100.8±0.1 mm and the internal diameter d is 31.7±0.2 mm.

Using $R = l\sigma^{-1}A^{-1}$ where A is the area and R is the measured resistance we have

$$\sigma = \frac{128 \pm 2\%}{R} \quad (\mathrm{m}^{-1}).$$

Electrode-electrolyte interfaces are very complex [82, 83, 84, 85, 86] and present an impedance that could potentially perturb the measurement of the specimen's conductivity. It is known that the interface between stainless steel electrodes and saline can be modeled by a resistor-capacitor combination. The impedance of this interface decreases with frequency and with current density [87]. In order to assess the effect of this impedance, preliminary tests are performed on standard saline solutions at different frequencies. The different methods used to measure the conductivity of the standards are:

1. Wayne-Kerr B642 bridge with the custom cell at 1.5 kHz,
2. W-K bridge with the custom cell at 20 kHz[1],
3. W-K bridge with a commercial platinum-black[2] conductivity probe (K=100/m) at 1.5 kHz,
4. W-K bridge with the commercial conductivity probe at 20 kHz,
5. HP3577A Network Analyzer with the custom cell at 20 kHz.

It turns out that all these measurement methods yield very similar results as shown in Fig. 4.2. We then conclude that no significant parasitic effect is present in the conductivity cell down to 1.5 kHz. Probably this is due to the large surface area of the electrodes. For reasons of simplicity and versatility, the HP3577A is used throughout this research to measure the conductivity. The estimated accuracy of this measurement is ±2%.

The gelling agent used in the TEM is Hydroxyethylcellulose (HEC) known as NATROSOL® 250 HHR, by AQUALON Company, Wilmington, DE 19894. It is a non-toxic and water-soluble powder-like polymer. To increase the polymerizing time, the powder is coated with a special agent that must dissolve before cross-linking can begin. This dissolution time depends on the temperature of the water. The warmer the water the faster the dissolution. For very

[1] An external source and an oscilloscope in the X-Y mode as the detector are used.

[2] Platinum-black electrodes have extremely low electrode-electrolyte impedance, which is the reason they are often used as standard electrodes. Their special property is due the roughness of their surface which produces a large effective area.

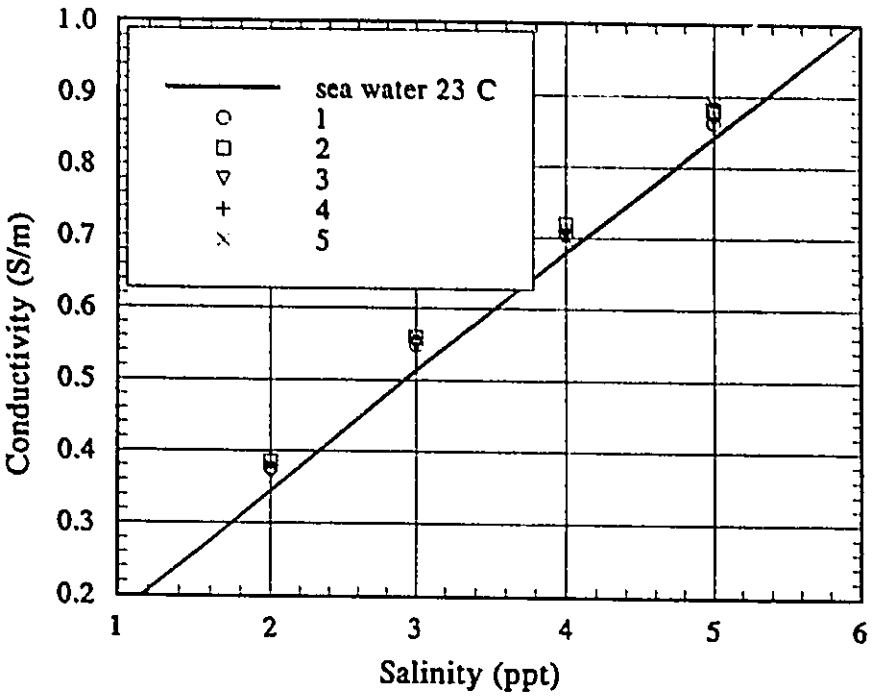

Figure 4.2: Conductivity of standard saline measured by the different methods defined in the text. The data for seawater come from [81]. The offset between the curve and the data points was not investigated but may be due to a difference in the temperatures.

viscous mixtures like the one considered here, fast polymerization results in the trapping of air bubbles which is undesirable. Therefore a compromise is necessary between the rapidity of the preparation and the quality of the material. At high concentration, NATROSOL solutions have a significant electrical conductivity which cannot be neglected.

The TEM was prepared by trial and error until the right viscosity and electrical conductivity were obtained. The list of ingredients is the following: water 100 g, NaCl 0.2 g, bacteriacide 0.1 g, HEC 16 g. First, the water and the salt are mixed together. The resulting solution has a conductivity of 0.362 S m^{-1} at 22°C. Then the bacteriacide and the HEC are added, and the mixture is stirred constantly until it thickens (approximately 8-10 minutes at 25°C). At that time it is poured into molds. A few hours must be allowed for cooling and setting. If the gel is prepared at 30°C instead of 25, stirring time is reduced by half but the gel contains more air bubbles and shrinks much during setting.

The TEM is translucent with a yellowish color. Its mechanical rigidity is sufficiently high to permit the molding of cubes that maintain their shape for up to 1 hour if left on a flat surface. It does not melt even at temperatures higher than 80°C. Its conductivity measured at 20, 50 and 500 kHz with the conductivity cell and the HP3577A is 0.61 S m^{-1} at 22°C. This is within less than 2% of the value measured at 500 and 1000 kHz with the measurement circuitry used for the ablation and described later. The temperature coefficient of the conductivity was experimentally estimated to be about +2% $°C^{-1}$. The specific heat and thermal conductivity of the TEM are assumed to be those of water. The properties of the tissue-equivalent material are presented in Table 3.2 at page 37.

4.2.3 Thermography

A thermographic camera consists of an infra-red (IR) detector, and an IR optical scanning system. The principle of thermometry with a camera like this is to relate the detected radiation to the source's temperature. Modern cameras are usually coupled to a computer which performs the operations of digitizing, temperature measurement and storing. A good description of practical thermometry with a thermographic camera can be found in [88]. Before going any further, a few comments about the radiation properties of materials must be made.

For an opaque surface, the principle of energy conservation relates the absorbed and the

reflected fractions of incident radiation of wavelength λ as follows: $1 = \alpha_\lambda + \rho_\lambda$, where α_λ is the absorptivity and ρ_λ the reflectivity of the surface[3]. In addition, Kirchhoff's relation states that under thermal equilibrium, the absorptivity and the emissivity ϵ_λ are equal. The emissivity is the ratio of the radiation emitted by a real surface to that emitted by a theoretical blackbody at wavelength λ. We thus have

$$1 = \epsilon_\lambda + \rho_\lambda.$$

For a theoretical blackbody, $\epsilon_\lambda = \alpha_\lambda = 1$ and consequently $\rho_\lambda = 0$. The above relations can be extended to characterize the radiation of the object over the bandwidth of the IR detector. We then talk about the absorptance (α), the emittance (ϵ) and the reflectance (ρ) of the surface, as equivalent averages over the bandwidth of interest. This being said, let us describe how the camera can relate radiation and temperature.

The spectral characteristics of the radiation of a theoretical blackbody source in terms of its temperature are given by Planck's relation [89, Chap.7], [90]. The thermographic camera can detect this radiation and calculate the corresponding temperature. The output signal of a thermographic camera is a function of the magnitude of the incident radiation over the active bandwidth of the detector. It also depends on the characteristic responses of the detector itself, the optics and the electronics. All these are taken into account in the camera calibration.

For real surfaces, the total response of the camera is the sum of the radiation reflected and emitted by the subject,

$$i = \epsilon I(T) + \rho I(T_{\text{ambient}})$$

where $I(T)$ is the response of the camera to a blackbody at temperature T. To obtain T from the measurement of i, one must know the function $I(T)$ and the values of ϵ and T_{ambient}. The above relation is valid only when the source is opaque. If it is not, the radiation from the background comes into play and it is then impossible to know the surface temperature accurately. Fortunately this is not our case as will be shown later.

The camera used in this study was generously made available by Bell Northern Research, Kanata, Ontario. It is a UTI Model CCT 9000 Computerized Color Thermograph System

[3]These quantities have been defined in various ways by different authors, and the complexity of the matter is quite a bit higher than suggested by the above statement (see [89] for example). However, we limit ourselves to the simple case of normal viewing of a diffuse surface, where the above relation is valid.

by UTI Instruments Company, Sunnyvale, Ca. The infra-red detector responds over the bandwidth 8–14 μm (a window of low absorption in air). The camera output is digitized and then treated by the computer. This one calculates the subject's temperature using ϵ and T_{ambient} entered by the user, and the distance to the object. The camera contains an internal blackbody reference, which is used for automatic calibration ($I(T)$). The temperature distribution is shown on the monitor using a user-adjustable color code. A cursor is provided to allow the reading of the temperature at precise locations. The temperature data can be stored on disk and a color printer is available for hard-copies.

In order to make accurate temperature readings, it is essential to perform a number of preliminary measurements. These are presented next.

Blackbody

A blackbody reference is necessary for the calibration of the camera. Since none was readily available, one had to be built. It is relatively simple to construct a blackbody cavity with an effective emittance of at least 0.999 [91, 92]. The real difficulty for metrologists is to know with accuracy what its emissivity really is, but this is not necessary here. A typical experimental blackbody consists of an *isothermal* cavity with a relatively small aperture, constructed with opaque material. Many designs can be considered. The simplest one in our case is to use a rectangular aluminum box ($\approx 70 \times 110 \times 50$ mm^3, 2 mm walls) with a 1 cm hole drilled at the center of an end face. A cone is placed inside the box at the end facing the aperture in order to increase internal reflections. The internal walls of the cavity are coated with matte black lacquer with an approximate emittance of 0.97 [93]. According to [92], the aperture of an isothermal cavity like this has an effective emittance larger than 0.999.

To ensure thermal uniformity, the aluminum box is surrounded by 5 cm thick styrofoam insulation. It is also covered with resistive wire so that it can be heated easily. After the box is heated, a delay is respected to let the temperature become uniform. Two temperature probes are fixed to the walls at both ends of the cavity to permit temperature comparisons. They had previously been calibrated against one another by inserting them in water baths at various temperatures. The blackbody is not used until the two temperature readings are within 0.1°C of each other. The thermal isolation and inertia of the blackbody result in a thermal time constant that is long enough to allow measurement with the camera.

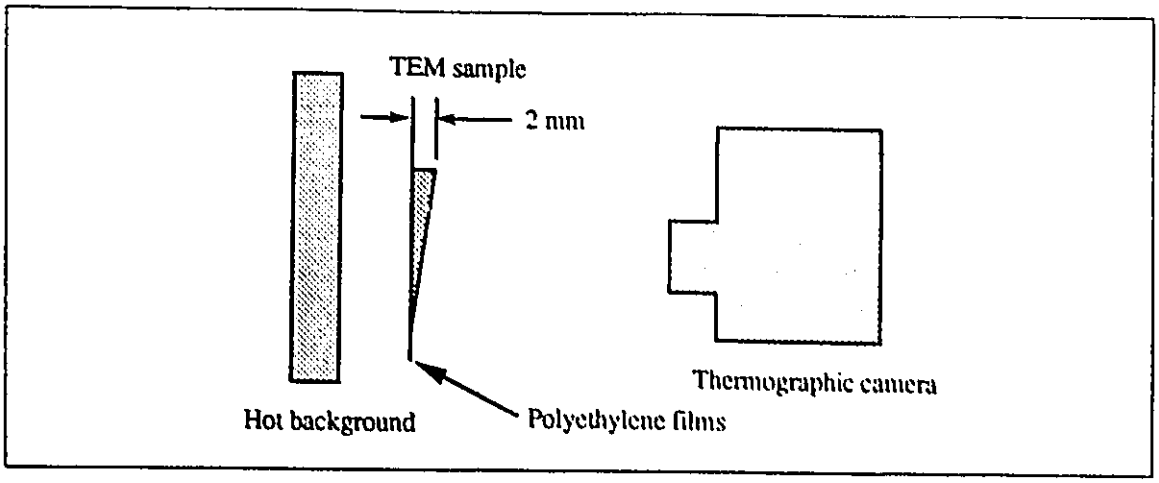

Figure 4.3: Experimental set-up for the determination of the IR opacity of the tissue-equivalent material.

Calibration of the camera is performed using the blackbody as reference. The cavity is heated to different temperatures and the camera reading is compared to the temperature readings of the built-in probes. At an ambient temperature of 22°C and using a blackbody emissivity of 0.99 (this is the maximum value that can be entered in the computer system), the camera slightly overestimates the temperature. A linear regression is applied on the available data and yields

$$T_{\text{real}} = 1.0412\, T_{\text{camera}} - 3.0073. \tag{4.1}$$

This relation is valid for temperatures in the range 20-60 °C.

Opacity

To know whether the measurement of surface temperature distribution is at all possible, it must first be confirmed that the tissue-equivalent material is opaque. If it was not, then the radiation emitted by deeper regions would add up to that emitted by the surface thus perturbing the reading of the temperature. The opacity of the material to IR radiation is not at all obvious, as it is translucent to visible light.

The arrangement used to determine the opacity of the TEM is as shown in Fig 4.3. A thin slice of TEM (26°C) is placed in front of a hot background (29°C) and its temperature is read by the camera. The specimen has a wedge shape with a maximum thickness of

2 mm and a minimum thickness of approximately 0.1 mm. To prevent rapid cooling by water evaporation, it is covered on both its faces by a polyethylene film ("Glad-wrap", few tens of μm thick). The high IR transparency of this film had been confirmed in a previous experiment by comparing the temperature of the blackbody aperture read by the camera with and without the film in front of it. The two differed by less than 1°C below 40°C confirming that the film is highly transparent. This agrees with Cetas [88] who evaluated the transparency of a 50 μm-thick film of polyethylene to be around 0.9. Back to the experiment depicted in Fig. 4.3, the temperature read by the camera proves to be uniform over the TEM sample, regardless of its thickness. The recorded temperature varies sharply between the gel and the hot background so that the contour of the specimen is made clearly visible. We conclude that the tissue-equivalent material is opaque at least for a thickness larger than 0.1 mm. This is in agreement with the results obtained in [88] for another type of high-water content material, and the data for water [93].

Now that the opacity of the TEM is established, its emittance must be determined in order to measure its temperature.

Emittance

The emittance of a material is estimated by comparing it with that of a known material at the same temperature. In principle the blackbody cavity could be used for that purpose but it is very difficult to achieve thermal equilibrium with a TEM specimen. Instead, the approach chosen is to spray matte black lacquer ($\epsilon \approx 0.97$) on a portion of the TEM surface and compare the camera reading with that of the adjacent unpainted portion. This ensures that the two measurement points are practically at the same temperature. Again, it is important to cover the TEM with polyethylene film because water evaporation results in rapid cooling of the unpainted surface.

The results reveal that there is no difference in the temperature reading between the black and plain surfaces. It is then concluded that the TEM and the black lacquer look identical to the IR camera. The emittance of the TEM is therefore considered to be 0.97 in this study. Again this agrees with the data for water, which is its main constituent.

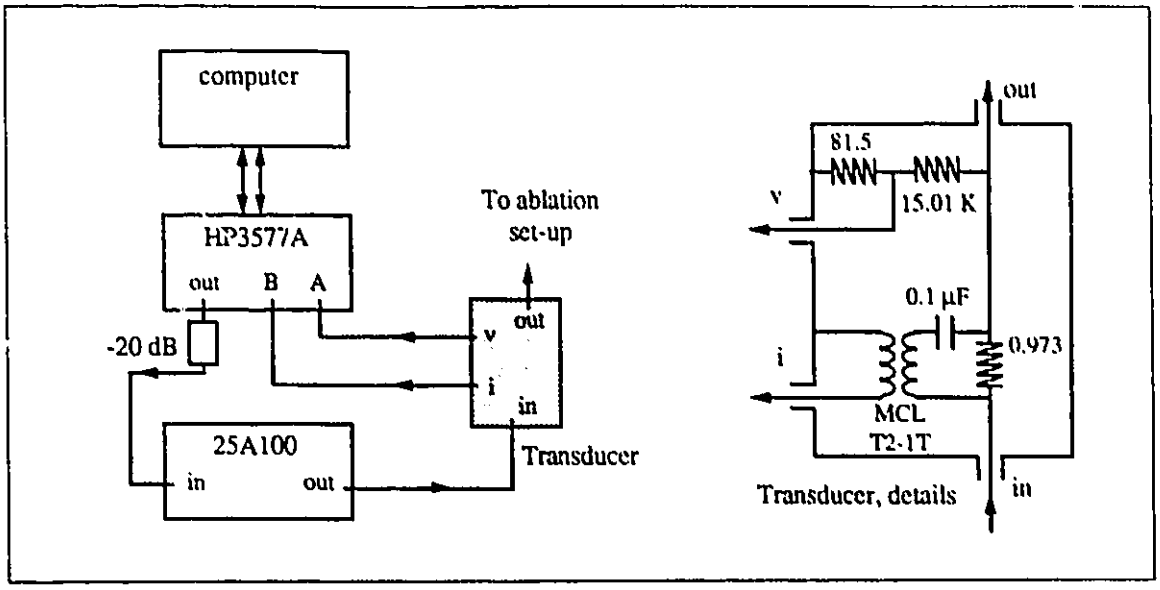

Figure 4.4: Schematic diagrams of the electrical generator and the transducer box.

4.2.4 Electrical Generator

In principle the electrical generator need not function at a frequency of 1 MHz for experiments on TEM. Because the quasi-static state prevails and the TEM conductivity does not vary significantly below 1 MHz, a lower frequency is expected to yield the same outcome at less expense. However, the design was originally made so that it could eventually be used for tests on animal tissue samples. In that case, the electrical properties are not independent of frequency and a 1 MHz excitation is necessary.

The electrical generator must be capable to provide at least 10 W of power at 1 MHz, have a controllable output level, allow for the monitoring of output voltage and current, and be computer controlled. A schematic diagram of the set-up used in this study is shown in Fig. 4.4. The arrangement consists of an HP3577A network analyzer, an Amplifier Research 25A100 power amplifier (25 W, 10kHz–100MHz), a custom-made transducer box and a computer. The source signal of the network analyzer is fed to the power amplifier through a 20-dB attenuator to protect the amplifier input stage. The RF power signal is then passed through the transducer box before being applied to the ablation set-up. The transducer box has two RF outputs, respectively proportional to the load current and voltage. These voltages are read by two high-impedance inputs of the network analyzer. Control and data acquisition is

done by the computer through the HP-IB interface and the HP3577A.

The diagram for the transducer box is also shown in Fig. 4.4. To calibrate it, the voltage divider is first calibrated at the frequencies of interest (0.5, 1.0 and 1.5 MHz). Then the transducer box is connected to the HP3577A with a standard 50-Ω load at its output port. The current transducer is then calibrated using the measured load voltage and the known voltage-current ratio. Verifications are made with a number of standard loads to confirm the validity of the calibration.

The computer program sets the level of the source and controls the data acquisition according to parameters found in a user-specified command file. It also performs the necessary operations to calculate the load resistance and power, and displays them in graphics form as ablation proceeds.

4.2.5 Procedure

Let us first remind at this point that the goal of the experimentation is to verify the numerical predictions. Accordingly, three experiments involving different factors of interest in this application are undertaken. In addition, a fourth one is performed in order to confirm that the polyethylene film used to facilitate the separation of the two TEM blocks does not upset the measurements.

In general, the TEM specimens are taken out of the molds just prior to the experiment in order to limit drying and deformation. They are then covered with pre-cut pieces of polyethylene film and fixed on the ablation set-up with waterproof tape. Great care must be used to ensure good, level mechanical contact between the two blocks of TEM where the ablating electrode touches. The edges of the blocks must be as sharp as possible for this. After the TEM is in place, the electrode is gradually lowered onto it so that the desired contact with the gel is obtained. This contact is verified by measuring, at low power level, the resulting resistance.

Experiment no. 1 consists in verifying that the presence of the polyethylene film between the two halves of the TEM block does not upset the electrical heating. In order to do that, the spherical tip electrode is positioned so as to produce an initial resistance of 208 Ω on a TEM block. This corresponds to the electrode touching the material only with the hemispherical portion of its tip. A constant voltage of 14.5 V is then applied for 60 s, during

which the resistance is recorded. This experiment is repeated twice. In the first case the two TEM halves are in direct contact and in the other case they are separated by two layers of polyethylene film.

The objective of Experiment no. 2 is to verify the validity of the theoretical prediction of the resistance value during heating. The set-up is the same as for Experiment no. 1. Two cases are considered. In the first one the voltage is initially high and decreases gradually. It is applied for 60 s. In the second case, the voltage is pulsed with a period of 10 s and a duty ratio of 0.5. The amplitude of the voltage in the two cases is determined by numerical simulations in order to produce a maximum tissue temperature increase of +43°C after 5 s of heating and to keep it afterwards. Unfortunately in this experiment the electrode-tissue contact was not done very thoroughly and the resulting initial resistance departs slightly from the theoretical value of 208 Ω. However this does not affect the relevance of the experiment.

Experiment no. 3 is again a comparison of the calculated and measured resistance but this time with a flat-tip electrode. The initial resistance is 177 Ω. Two constant voltage levels of 10.95 and 14.14 V applied during 30 s are considered.

Finally, in Experiment no. 4 the calculated temperature distribution is compared to the one obtained experimentally. This is done with 3 constant voltage levels of 10.95, 14.14 and 15.81 V, for a duration of 30 s each. A hemispherical tip electrode is used with an initial resistance of 208 Ω. Both the resulting resistances and temperature distributions are recorded and compared to the simulation.

All the above experiments have been repeated many times. However, because of the limited availability of the camera only a small number of temperature distributions (Exp. 4) have been obtained. Of those, some had to be rejected because the camera was out of focus or the movement of the experimental set-up blurred the picture. At the end, 5 good temperature recordings were kept.

Theoretical Modeling

The model considered for the simulations is that of Fig. 3.1 (p. 25), with the dimensions and physical properties of the material used experimentally. The ablating electrode is truncated at 10 mm above the TEM surface. Its properties are those of Platinum which are close to

the properties of steel[4].

A convective boundary condition is applied at the TEM and the electrode surfaces. The value of the heat transfer coefficient there is that of free air convection, approximately $h = 25$ W m^{-2} °C^{-1}. At the truncated end of the electrode, a convective boundary condition is also applied but with a higher coefficient of $h = 100$ W m^{-2} °C^{-1} to take into account the heat lost by conduction to the shaft of the electrode. This is a first approximation that does not significantly affect the outcome of the simulation because the surface area over which it is applied is relatively small. A time step of 1 s is selected after having verified that using 0.5 s produces no significant difference in the outcome.

4.3 Results

Fig. 4.5 presents the experimental results for the resistance between the two electrodes with the TEM half-blocks in direct contact and separated by two polyethylene films. The applied voltage is as shown in the figure. It is seen to decrease with time. This is an undesired effect of the amplifier's output impedance. The two resistance curves are indistinguishable with an initial value of 208 and a final value of 125 Ω. The agreement was expected because as mentioned earlier, the electric current and thermal transfer should not be disturbed by the film because of the symmetry. Nonetheless, the degree of harmony between the two curves is striking.

The following figure shows a comparison of the calculated and the measured resistance vs time for Experiment no. 2 (Fig. 4.6). The theoretical results have been obtained using the TEM data given earlier, with a time step of 1 second. Apart from an initial difference of about 8 Ω, the theoretical and experimental curves are in very good agreement. This difference is due to an improper adjustment of the contact between the spherical tip electrode and the TEM. Had it been done properly in the experiment, the agreement would have been excellent for the first 30 s or so, and slowly degrading afterwards. In particular the undershoot at six second in the resistance curve for the modulated voltage is well predicted by the numerical model.

[4]The properties of Pt have historically been used in our simulations because it is the metal clinical electrodes are made of. For the simulations of interest here we forgot to replace them with those of steel. The two metals have similar ρc_p products but it seems that their respective thermal conductivities may be different by a factor of 2 or so. This is not expected to produce any significant consequence on the outcome of the simulations as the thermal conductivity of the two metals is at least thirty times larger than that of the TEM.

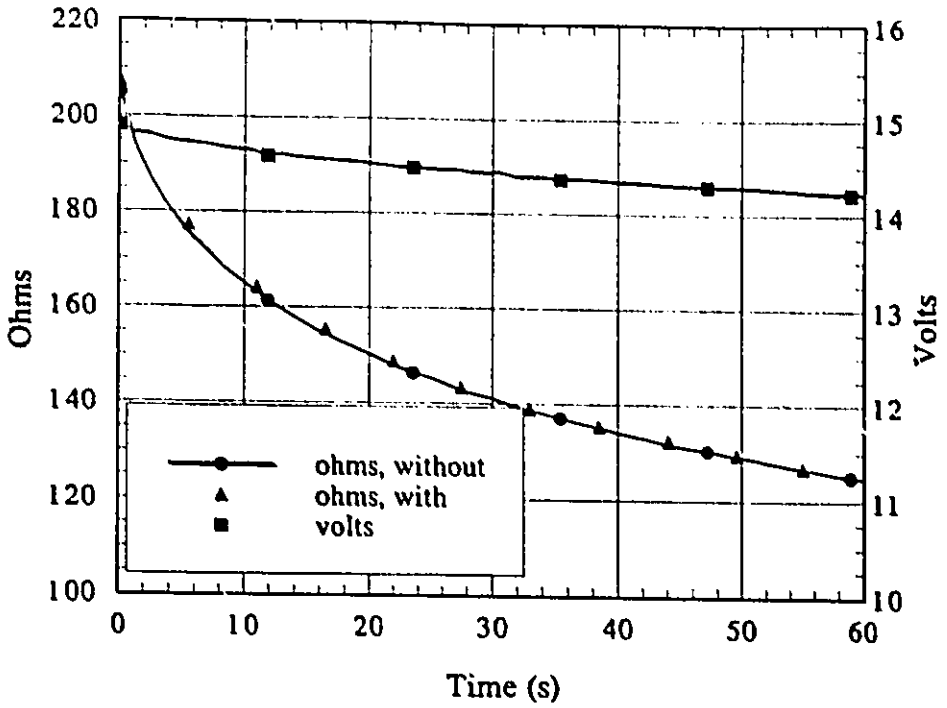

Figure 4.5: Experimental resistance and voltage with and without 2 layers of polyethylene film between the TEM half-blocks (Exp. 1).

Similarly, the amplitude of the oscillations for the pulsed voltage corresponds closely to the predictions. The degradation in the concordance of the theoretical and the experimental results after 30 s is partly explained by the cumulative addition of the errors from time 0.

Fig 4.7 shows the results obtained in Experiment no. 3 with the flat-tip electrode. The application of two constant voltage levels of 10.95 and 14.14 V for a duration of 30 s is considered. Again, the theoretical predictions agree well with the experimental results.

Finally, Fig. 4.8 and Figs. 4.9, 4.10, 4.11, 4.12 show respectively the resistance and the temperature distributions of Experiment no. 4. In all cases the initial resistance is 208 Ω and decreases with time as the sample heats up. The agreement between the calculated and the experimental resistance is, as before, good in all three cases.

All temperature distributions are spherical and concentric with the electrode tip, as shown in Fig. 4.9 for the case where the voltage is 10.95 V. To simplify comparisons, only the TEM temperature on an imaginary line that prolongs the electrode axis is considered. Accordingly, the temperature is plotted against the depth in millimeters. For the voltage level of 10.95 V, only one good quality temperature distribution could be recorded. On the other hand, for

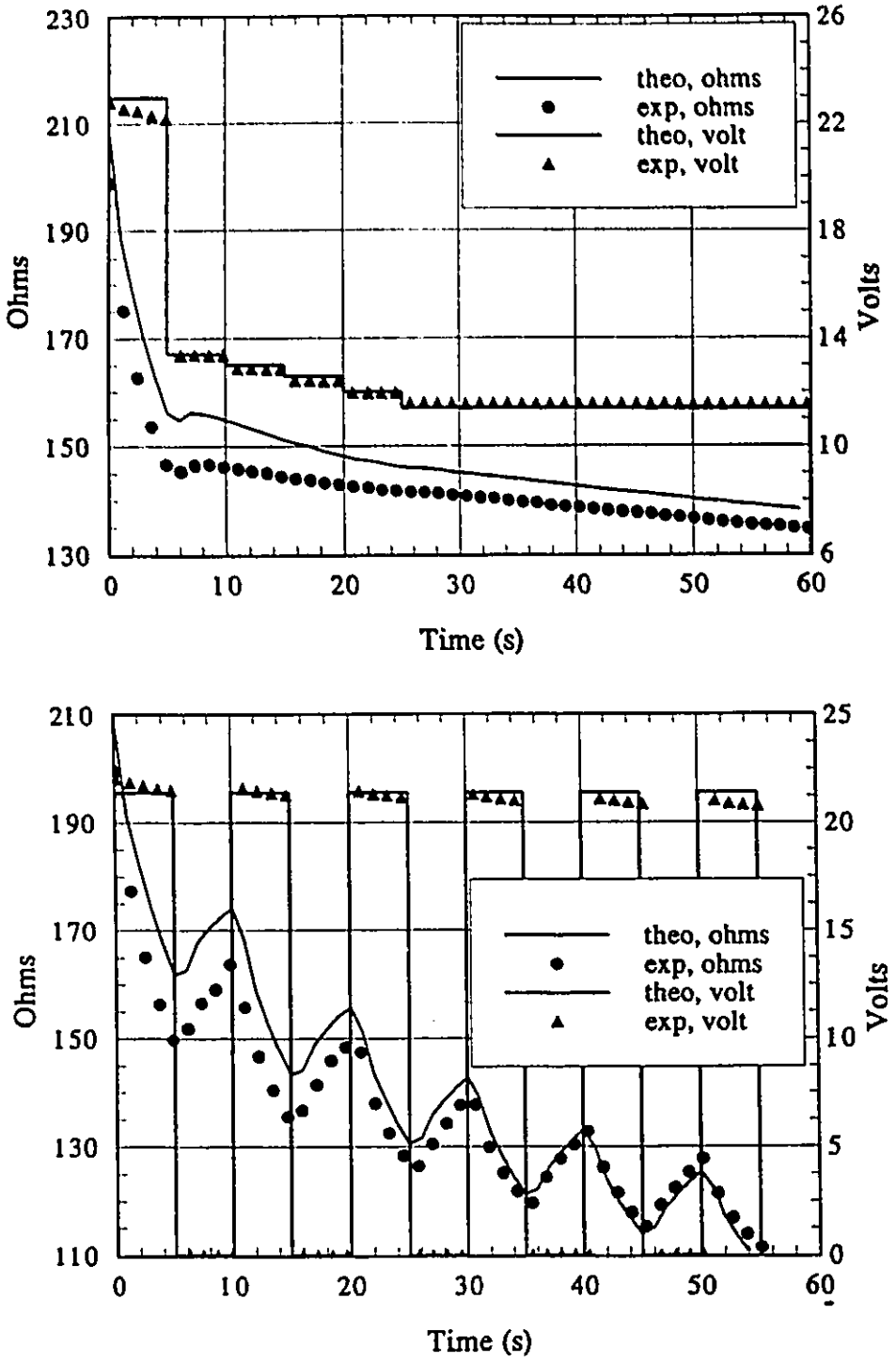

Figure 4.6: Experimental and theoretical resistances with modulated voltage (top) and pulsed voltage (bottom) (Exp. 2). The voltage curves are also shown.

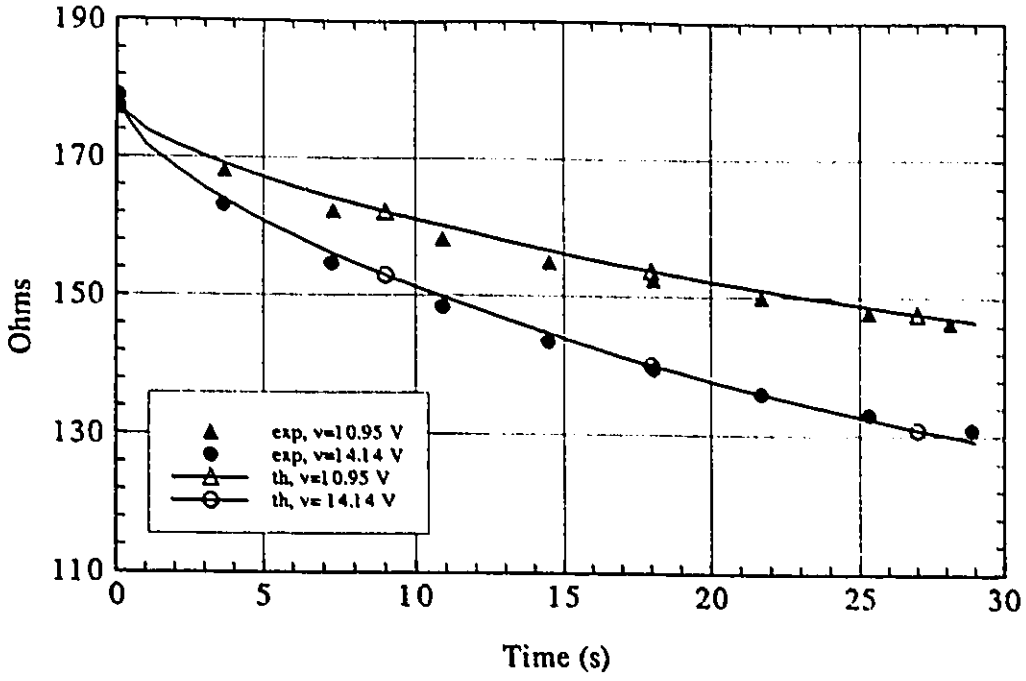

Figure 4.7: Experimental and theoretical resistances with a 2.5 mm flat-tip electrode (Exp. 3). Two constant voltage levels of 10.95 and 14.14 V are applied for 30 s.

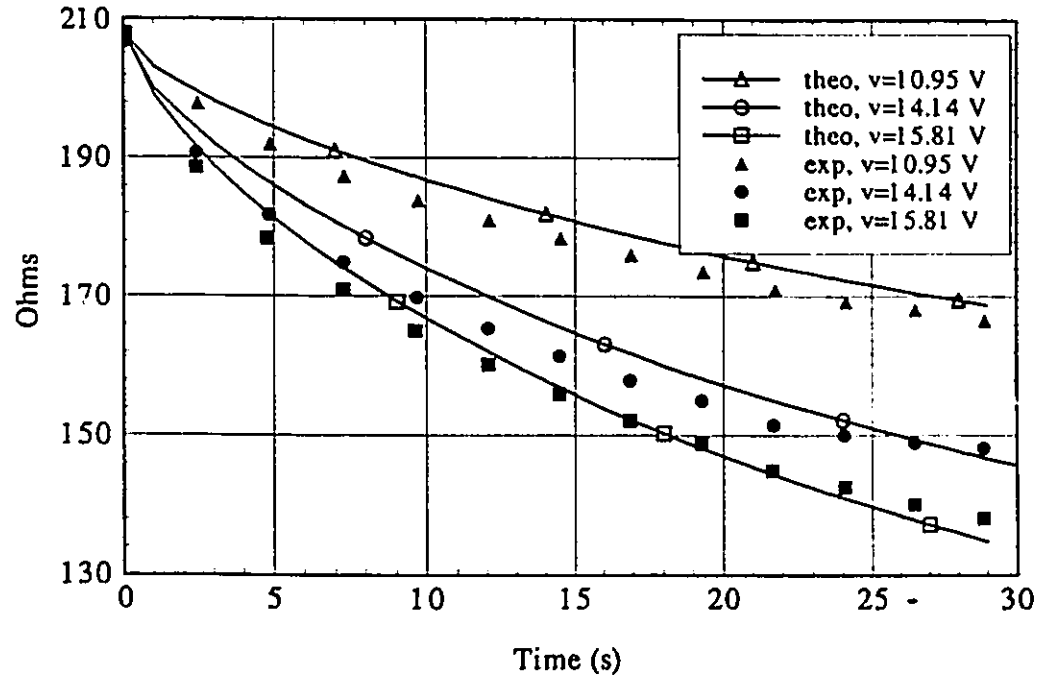

Figure 4.8: Experimental and theoretical resistance, 3 different constant voltages (Exp. 4).

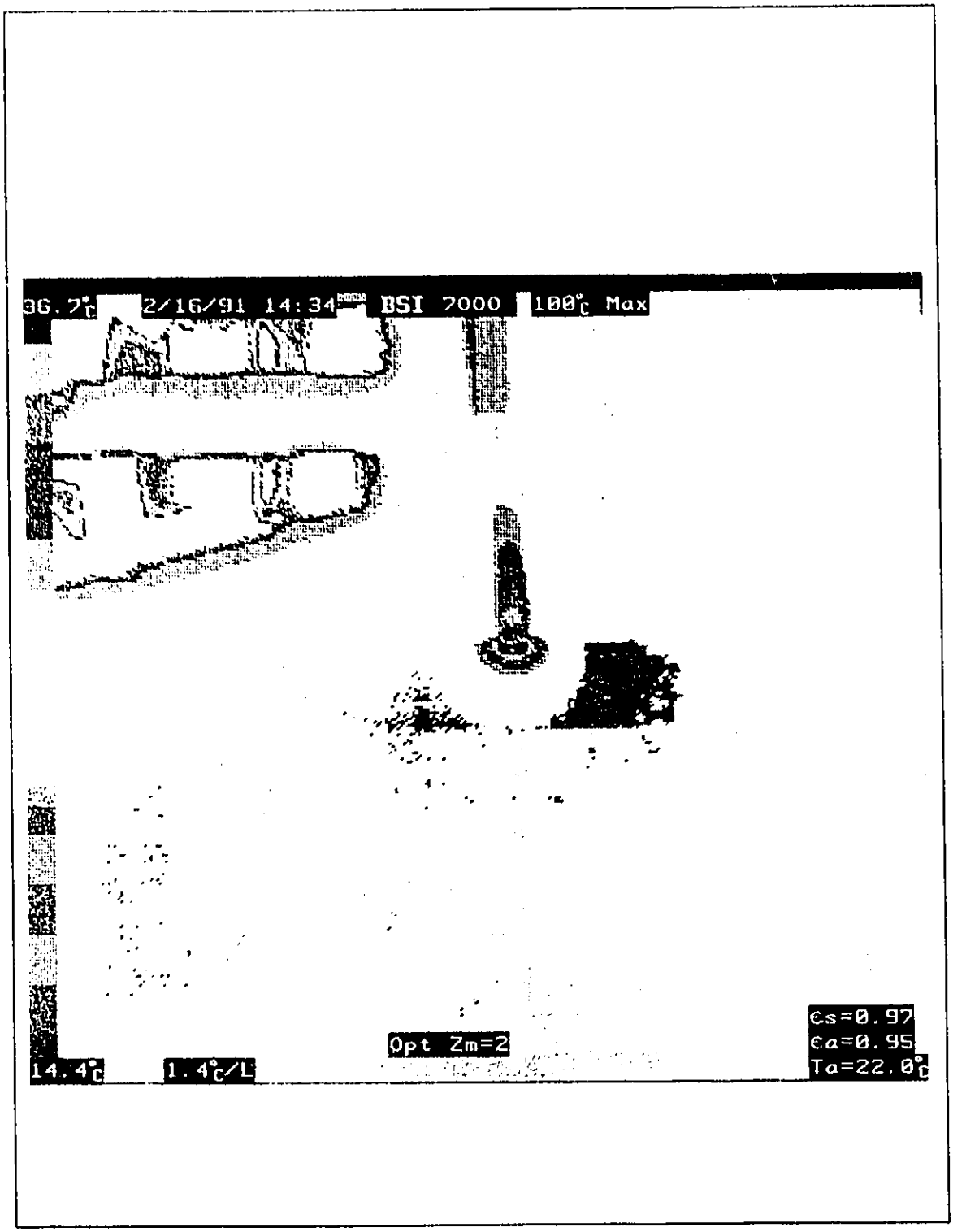

Figure 4.9: Color plot generated by the thermography system. (File v120t30.004). In the top left corner is the vernier caliper, the electrode tip is at the center. V=10.95 V, Exp. 4.

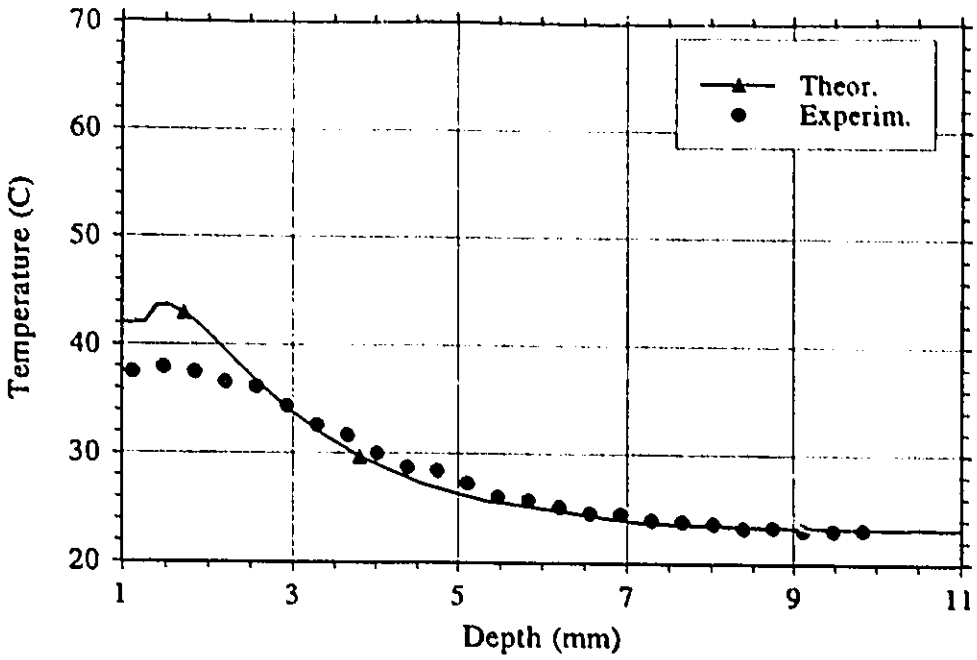

Figure 4.10: Temperature profiles on the electrode axis, v=10.95 V, theory vs experiment (Exp. 4).

14.14 and 15.81 V two good experimental recordings were made and both are shown in the respective figures. No measurements of temperature at depths smaller than 1.0 mm are presented on the graphs. The reason for this is that this region corresponds to the electrode tip itself (with a radius of 1.25 mm) and because stainless steel has a low emittance, the camera is incapable of making an accurate measurement of its temperature. The experimental data have been corrected to remove the camera's inaccuracies (Eq. (4.1)). In addition, all curves have been adjusted to have a basal temperature of 23 °C.

The temperature profiles all feature a maximum at a depth of approximately 1.5 mm and a gradual decrease at larger depths. The measured temperatures are lower than the calculated values below 4 mm approximately, and slightly higher at larger depths. Below 3 mm, the experimental curves depart significantly from the theoretical results, while the agreement is good elsewhere. The discrepancies below 3 mm can be explained by several factors, discussed in the next section.

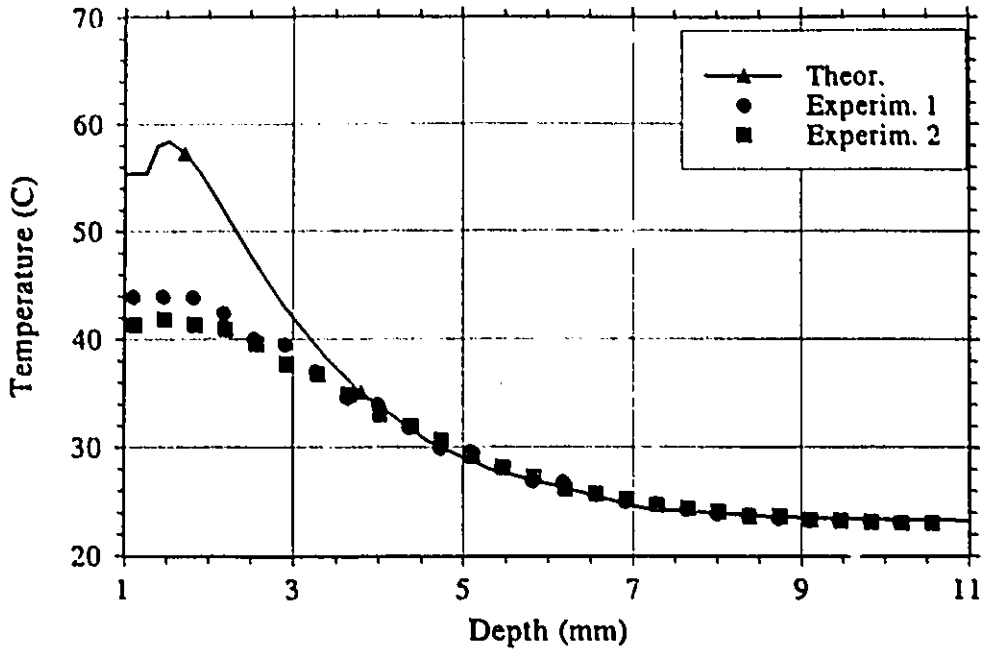

Figure 4.11: Temperature profiles on the electrode axis, v=14.14 V, theory vs experiment (Exp. 4).

4.4 Discussion

The results of Experiment no. 1 clearly show that the effect of the polyethylene film used to separate the TEM blocks is truly negligible. The electrical behavior is not at all disturbed by it. This also shows that the ablation experiments are easily reproducible. This has been observed continuously during this research and is certainly due to the usage of a tissue-equivalent material with controlled physical properties. This reproducibility also confirms the adequacy of the experimental set-up and procedures.

Experiment no. 2 reveals that even in complex situations where the voltage is modulated in time and the electrical conductivity is temperature-dependent, the simulations are very realistic. The calculated resistance remains within a few percent of the measured one even after 60 s of heating. The degradation in the agreement observed in the latter part of the heating period can be explained by various factors: the thermal properties of the TEM are not the same as those of water, the temperature coefficient of the conductivity is not constant with temperature, the tip of the experimental electrode is not exactly spherical. Moreover,

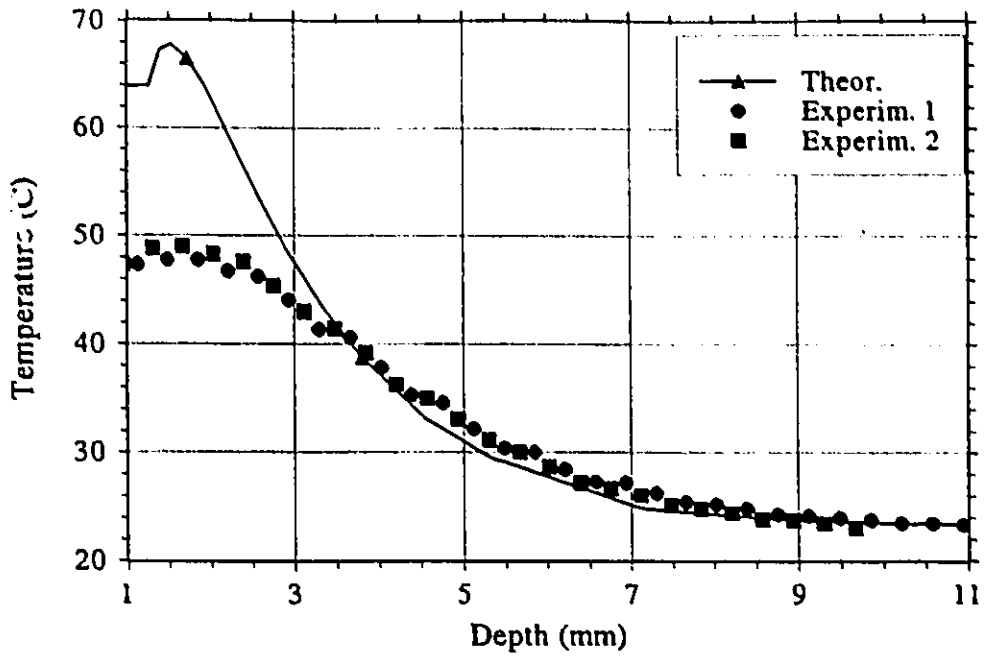

Figure 4.12: Temperature profiles on the electrode axis, v=15.81 V, theory vs experiment (Exp. 4).

as mentioned above the error of the simulation is cumulative in time as ablation progresses. Considering all this, it appears that as far as resistance is concerned, the simulations are realistic. This is again evidenced by the results of Experiment no. 3 with a flat-tip electrode. In these simulations, the finite-element mesh had to be made very dense at the electrode tip to faithfully model the sharp corner. In spite of the added difficulty, the numerical results again prove to be accurate. But it is the prediction of the temperature field that is the ultimate goal of the simulations and this was considered in the fourth experiment.

The results for Experiment no. 4 again show the good agreement between the predicted and measured values of resistance during heating. The temperature profiles that were recorded also agree with the predictions except at depths lower than 3 mm. There are at least two reasons that can explain this. Probably the most important one is the cooling of the TEM while it is being opened up and during the camera scan. There are three different mechanisms responsible for cooling. First, water evaporation from the wet TEM causes an important loss of heat. Second, the sudden flow of air on the hot surface at the opening of the split block causes heat loss by convection. Third, heat is conducted away from the

hot spots through the TEM itself. All these mechanisms are predominant around the point of highest temperature. Furthermore, because the mass of material at a high temperature is relatively small (spherical distribution) the cooling is even more rapid. All these factors contribute to lower the temperature of the hot spot and this type of experimental results had to be expected.

A second factor that can partly explain the lower value of the measured temperature below 3 mm is the limited spatial resolution of the camera. The spatial resolution of a scanning system is related to the physical size of the detector. It represents the ability of the system to distinguish two closely separated sources. The consequence of an imperfect resolution is that the recorded image is always a low-pass filtered (in the space-domain) version of the source. When the source is relatively large, the recorded image is close to the reality. But for smaller sources there results an averaging of the temperature in the neighborhood of the source point whose effect can be very pronounced. In this case, the hot spot is of small size and adjacent to the electrode tip. Because of the low emittance value of stainless steel, the electrode tip appears to the camera as a cold area. Consequently, the inherent spatial averaging can only result in the thermometry system to underestimate the temperature of the hot spot. Again, this agrees with the observation.

Another feature of the temperature profiles is that the measured ones are all slightly higher than the predictions between 4 and 8 mm. The reason for this may be the imprecision on the thermal properties of the TEM. The conduction of heat from the hot spot to the surrounding can not account for such a large difference as confirmed by a separate numerical simulation not included here. Experiments with much more accurate equipment would be necessary to resolve the issue.

All being considered, the agreement between the simulations and the experiments demonstrated above provides a good validation of the numerical model. It is likely that the discrepancies that are noted can largely be attributed to the imprecision in the physical parameters considered in the simulations: electrode shape, thermal properties, temperature coefficient. Much more work with high precision instruments would be required to quantify these effects. As far as we can practically verify, the simulations seem accurate both for the prediction of the resistance and the temperature distribution during the ablation procedure.

4.5 Conclusion

In this chapter we presented a series of experiments designed to test the validity of the theoretical modeling of Chapter 3. Measurements of the time-dependent resistance and the temperature distribution during ablation have been compared with those predicted theoretically under various conditions of voltage excitation and electrode shape. We found that a good agreement was generally obtained which confirms the accuracy of the theoretical model.

The ablation experiments were performed on tissue-equivalent material instead of biological tissue for reasons of convenience and to ensure reproducibility of the physical properties. The evaluation of the resistance during the ablation was relatively simple as it only involves the measurement of electrical quantities that is easy to perform. On the other hand, the accurate determination of the temperature distribution in the material is much more difficult. To accomplish it, a split-block arrangement was conceived to allow the exposure of the cross-section of the heated region to a thermographic camera. This procedure turned out to be very delicate to perform. Problems of focusing, vibration, scanning triggering, and unwanted cooling of the subject are regularly encountered. In addition to the experiments reported here, we also tried to build an experiment that included a cooling fluid around the electrode to reproduce the action of the blood flow present in the heart. In that case, we ran into major problems with the measurement of the temperature due to the presence of the fluid which was opaque to IR radiation. This combined with the difficulty in quantifying the flow around the electrode made those experimental results meaningless.

The difficulty in acquiring information about the temperature field in the heated material provides by itself a good justification for the theoretical approach proposed in this research.

Now that the validity of the theoretical model has been confirmed both analytically in Chapter 3 and experimentally here, we are ready to tackle the study of RF ablation as such. This work is presented in the next two chapters.

Chapter 5

Theoretical Modeling II: Preliminary Considerations

The numerical model is used in order to clarify a number of issues about the realistic modeling of ablation. These include the determination of the model dimensions, of adequate boundary conditions, the importance of the blood flow, and the significance of the temperature dependent conductivity. These preliminary considerations lead to a good understanding of the important components of the model. At the end of this chapter, the model is well defined and can be used with confidence to investigate RF ablation, which is done in the following chapter.

All simulations presented here are done with a time step $\Delta t = 1$ s and $\tau = 0.5$ (refer to Appendix C for the definition of these quantities). The time step has been found adequate by comparing with a few simulations using $\Delta t = 0.5$ s.

5.1 Model Dimensions

The geometry of the model used in this study of RF ablation is presented in Chapter 3. It is axisymmetric and consists of a block of tissue with an ablating and a grounded electrode. In order that the conclusions of the analysis of this model be applicable to real-life ablation, it is essential that the current distribution (or more exactly the dissipated power per unit volume called *specific absorption rate*, SAR) and the temperature field around the ablating electrode be realistic. All the heat transfer phenomena that are significant to the ablation are very localized and therefore not much influenced by the distance between the electrodes. However, the SAR distribution depends more strongly on the model dimensions, which must

$w = h$ (mm)	R (Ω)	SAR at tip ($\times 10^{-4}$W mm^{-3})	% SAR (wrt $w = h = 64$)
14	98.6	2.456	-3.9
25	94.3	2.518	-1.5
34	93.5	2.541	-0.6
44	93.2	2.550	-0.2
54	93.1	2.554	-0.08
64	93.0	2.556	-

Table 5.1: Effect of model dimensions on SAR and resistance.

therefore be chosen to reflect reality as closely as possible. It must be reminded here that the model is homogeneous as explained in Chapter 3. Tissue heterogeneities which also have an effect on the SAR are not considered. The influence of the dimensions of the model on the SAR is now evaluated.

Procedure

Numerical calculations are made using the model of Fig. 5.1. The electrode characteristics, which correspond to realistic values, are the following: length (l)=4 mm, radius (r)=1.25 mm, depth inside tissue (d)=1.25 mm. The tissue is homogeneous heart tissue as discussed before. Blood is assumed to be present around the Platinum electrode. No current flows through the boundaries (Neumann conditions for the voltage), except on the portions corresponding to the electrodes where voltages of 1 and 0 V are applied. The width (w) and height (h) of the model are varied between 14 mm and 64 mm and the resulting SAR distributions are compared. The width and height of the heart block are kept identical.

Results

The SAR calculated at the tip of the ablating electrode and the electrode resistance (defined as the resistance between the two electrodes) are shown in Table 5.1. As the dimensions increase, the SAR at the tip and the electrode resistance vary less and less rapidly, as expected. The values of the SAR at other points around the ablating electrode present a similar behavior. The calculated SAR with $w = h = 44$ mm is within 0.2% of the value obtained with $w = h = 64$ mm.

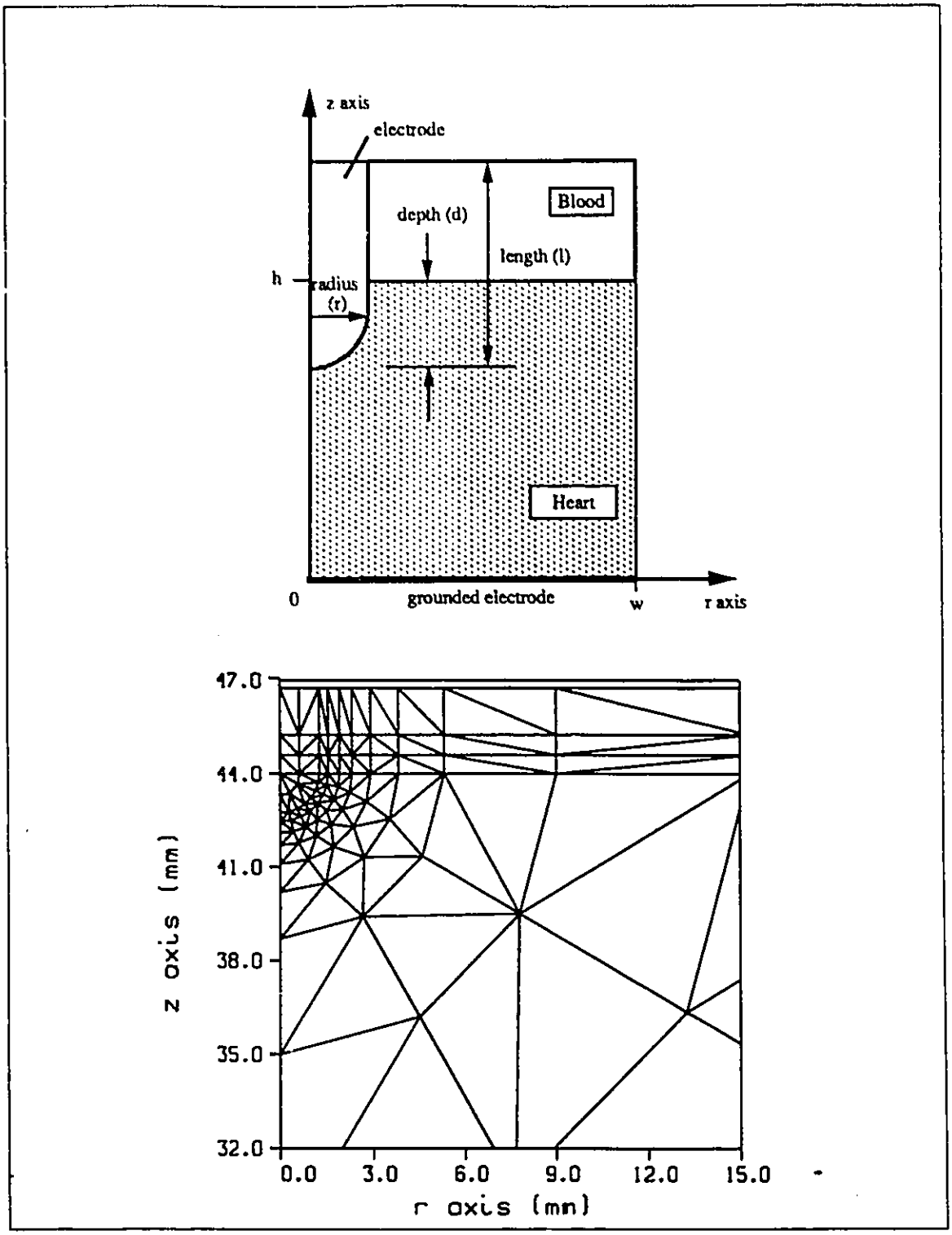

Figure 5.1: Drawing of the model with dimensions and FEM grid around the electrode.

Discussion

When the electrodes are far apart, a further increase in their relative distance only has a minor effect on the current distribution around the catheter electrode. The SAR then becomes practically independent of the electrode distance. An illustration of this is provided by the consideration of the current ($J(r)$) between two concentric spheres of radius r_1 and r_2, and which obeys:

$$J(r) = \sigma \left(\frac{r_1 r_2}{r_2 - r_1} \right) \frac{1}{r^2}$$

where σ is the material conductivity. When $r_2 >> r_1$, $J(r)$ does not depend on r_2 anymore. The situation is analogous here and for a model with dimensions relatively larger than the ablating electrode, the SAR only depends on the size of the ablating electrode and the material conductivity. The electrode resistance behaves similarly.

Dimensions in the order of 64 mm would be expected to produce realistic results because they are comparable to those encountered during catheter ablation on humans. The simulations show that the SAR obtained with $w = h = 44$ is practically the same as with $w = h = 64$ mm. The smaller dimensions are preferred for the remaining of this research because it is easier to work with a small structure than with a large one.

These dimensions are expected to be valid for the thermal problem as well. The boundaries are located far enough from the electrode tip that they should not interfere with the temperature distribution of interest. In fact, for the thermal problem, the boundaries are practically at infinity.

5.2 Boundary Conditions

In general, in order to use the FEM, it is necessary to have a closed solution domain, with appropriate boundary conditions (BC's). Sometimes, the numerical boundaries correspond to real physical ones like is the case for the electrodes in the electrical model considered in this study. In these cases, the BC to be applied is obvious. However, in other cases, a solution is sought for a problem with no natural or convenient physical boundaries. In these so-called open problems, artificial boundaries must be applied to define the solution domain. The location and type of the artificial boundaries must be chosen carefully so as not to introduce artifacts in the numerical solution. When the artificial boundaries are adequate,

the solution in the area of interest can be very close to the solution of the real open problem. The definition of appropriate artificial boundaries must be done in this study. As mentioned in Chapter 3, the BC's to be applied on this model of ablation are relatively obvious except at the heart surface for the electrical problem and at the root of the electrode for the thermal problem. These issues are considered here.

5.2.1 Electrical Boundary Condition

The concern here is the location of the boundary that is appropriate to limit the solution domain in z. During real catheter ablation, the current flows out of the ablating electrode in all directions and not only directly towards the grounded electrode. However, it is clear that the current is the most intense inside the heart, at the electrode tip. In view of this, one may wonder if enforcing a Neumann boundary condition (NBC) at the heart-blood interface does not represent a valid simplification (Fig. 5.1). To use a NBC there significantly facilitates the whole solution because then, the same grid can be used for the thermal and the electrical problems, with a simple change in the types and the values of the BC's. What must be evaluated is whether the SAR around the electrode is significantly modified when the blood around it is removed and replaced by a NBC at the heart-blood interface.

Procedure

Numerical calculations are carried out to compare the SAR distribution at the electrode tip with 1) consideration of the blood surrounding the electrode which is the realistic situation, and 2) a NBC at the heart-blood and the electrode-blood interfaces which may constitute a valid simplification. Simulations are done with the following dimensions: $l = 2.5$ mm, $r = d = 1.25$ mm, $w = h = 44$ mm. The thickness of blood considered is 1.25 and 2.75 mm. For the simulations with blood, a NBC is enforced at the top of the blood layer.

Results

The SAR distributions are shown in Fig. 5.2. (The irregularities in the curves are due to the inter-elemental discontinuity of the electric field in the FEM solution, see p. 125). The electrode resistance is 207.9 and 127.5 Ω with and without the blood (1.25 mm thick) respectively. The figure shows that the SAR with the blood layer has a lower gradient and

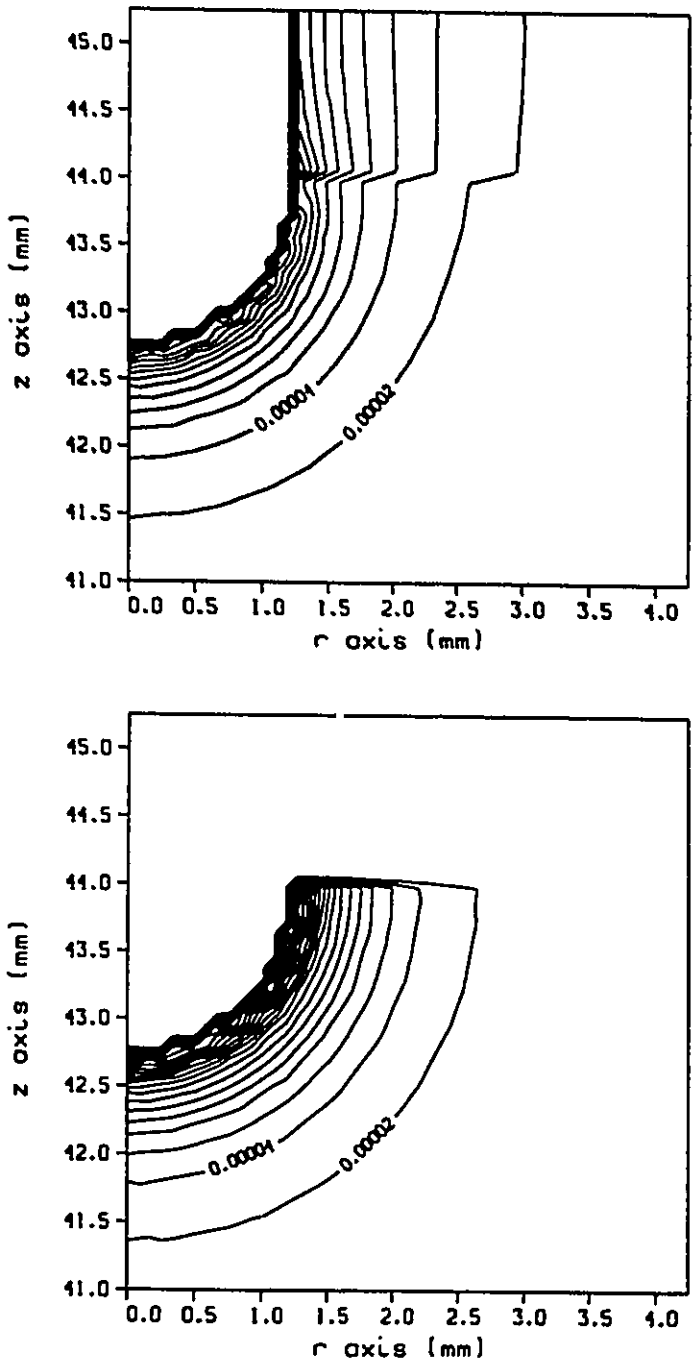

Figure 5.2: SAR (W mm^{-3}) around electrode with and without blood layer. Top: with 1.25 mm blood layer. The electrode resistance is 127.5 Ω, the SAR at the tip is 2.993×10^{-4} W mm^{-3}. Bottom: with NBC at heart-blood interface. The electrode resistance is 207.9 Ω, the SAR at tip is 3.989×10^{-4} W mm^{-3}.

also a lower magnitude at the tip than in the other case. With blood, the SAR at the tip is $2.993 \cdot 10^{-4}$ W mm^{-3}, while without it a value of $3.989 \cdot 10^{-4}$ W mm^{-3} is obtained (+33%). In addition to those differences, the spatial distributions of the SAR are also different. Without blood a spherical distribution is obtained while with the blood the SAR is more concentrated at the tip than close to the heart-blood interface (68% higher). The discontinuity in the SAR at $z = 44$ mm when the blood is present is due to the different conductivity of the blood and heart tissue.

When the blood layer is increased to 2.75 mm, an intense and very localized electric field is produced on the corner of the electrode root. To resolve it adequately would require an extremely fine grid. We used a relatively crude one so that the SAR in that area could not be calculated with a high precision. Nonetheless, the calculation reveals that this new contribution to the current distribution is too localized to have a significant effect on the SAR at the tip. On the other hand it has a non-negligible effect on the resistance.

Discussion

When a NBC is placed at the heart-blood interface, the resulting SAR distribution is very close to the one obtained between two concentric conducting spheres. The calculations show that this overestimates the SAR by as much as 33%. Therefore, it is not a valid simplification concerning both the SAR distribution and the electrode resistance. In order to obtain accurate and realistic results, it is necessary to include the blood surrounding the electrode. This means that two different FEM meshes are required for the electrical and the thermal problems.

The blood layer included in the calculation does not need to extend beyond the electrode root in the case studied here. The reason is that the extra contribution to the electric field is concentrated too far from the area of interest (the electrode tip) to be significant. This reasoning can *a fortiori* be extended to electrodes longer than 2.5 mm and inserted more deeply than 1.25 mm inside the tissue.

5.2.2 Thermal Boundary Condition

The BC's for the thermal problem have all been presented in Chapter 3 except for the electrode root. There, heat generated inside the tissue and conducted through the electrode itself

flows towards the body of the catheter which is cooled by the blood flow. This heat transfer is governed by the properties and the exact geometry of the electrode and the catheter. In absence of these data, it is possible to create an artificial boundary which can provide a valid simplification. Certainly it can neither be a Dirichlet nor a Neumann condition because the temperature is not constant, and heat flow is present. However, an artificial convective BC (CBC) can be enforced (Eq. (3.4), p. 28). An appropriate value for the heat transfer coefficient (h) is determined by modeling.

Procedure

Simulations are performed with various values of h at the root in order to compare the resulting temperature distributions, and draw conclusions as to the most appropriate value. The dimensions are as follows: l = 2.5 mm, $r = d$ = 1.25 mm, $w = h$ =44 mm. This is the shortest electrode considered in this study, the one for which the root BC has the most significant contribution on the final temperature distribution. A constant voltage of 25.5 V is applied on the electrode for 30 s. This value is selected because it is similar to what is used in practice and therefore yields realistic temperature distributions. The particular choices of h are 0, 500 and 2000 W m^{-2} $°C^{-1}$ which reflects the expected order of magnitude of the heat flow. A value of $h = 0$ means no flow of heat and h = 2000 W m^{-2} $°C^{-1}$ is the coefficient for the heart-blood interface. These two values certainly bracket the effective coefficient at the root which may be in the order of 500 W m^{-2} $°C^{-1}$. Because it is only the thermal problem that is of interest in this section, the electrical problem is simplified by considering a NBC at the heart-blood interface and neglecting the temperature dependence of the conductivity. The SAR is therefore constant and need only be calculated once.

Results

The temperature profile vs depth for the three values of h are shown in Fig. 5.3. The temperature is the increase from a basal temperature of 0°C. Depth is measured on the z axis, from the heart surface at 44 mm. The figure shows that the maximum tissue temperature at a depth of approximately 2 mm, varies by 3°C and the electrode temperature by 4°C. In all cases, the temperature difference between the electrode and the tissue is more or less the same. As expected, the higher the value of h, the lower the resulting temperature.

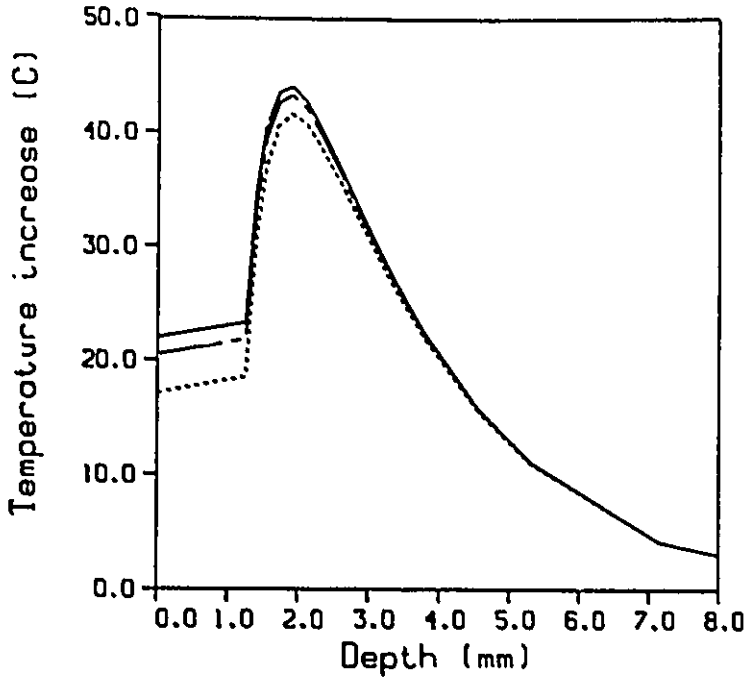

Figure 5.3: Temperature increase (25.5 V, 30 s) vs depth on the z axis with various h (W m^{-2} °C^{-1}) at the electrode root. Solid: $h = 0$, chain: $h = 500$, dash: $h = 2000$.

Discussion

A rough evaluation permits to conclude that h at the electrode root is between 0 and 2000 W m^{-2} °C^{-1}. These simulations do not reveal what its actual value really is. However, they demonstrate that these two extremes result in maximum tissue temperatures that differ by less than 3°C. The reason this boundary is not very determinant on the temperature distribution is that it only represents a small percentage of the whole boundary surfaces. The possible error made by imposing $h = 500$ W m^{-2} °C^{-1} is in the order of only 1°C which is acceptable. All subsequent simulations are done with $h = 500$ W m^{-2} °C^{-1} at the electrode root.

5.3 Importance of the Presence of Blood

The presence of the circulating blood around the ablating electrode certainly contributes to cool the tissue. But how important is this effect and how much more power is necessary because of it? How does this influence the ultimate lesion shape? In this section simulations

are carried out to answer these questions.

Procedure

To demonstrate the effect of the blood flow, two simulations are done. In the first case, blood flow is neglected by setting $h = 0$ at the heart-blood interface and in the second case, the cooling effect of blood is included ($h = 2000$ W m^{-2} °C^{-1}). Since it is the thermal behavior that is of interest, the electrical problem is slightly simplified. The electrical conductivity is considered constant so that the SAR does not vary with time. To enable a meaningful comparison, in both cases the SAR is the same and is calculated *with the blood present*. The geometry is $l = 4$ mm, $r = d = 1.25$ mm and $w = h = 44$ mm. In both simulations, a constant voltage is applied, and its value is selected so as to produce a maximum tissue temperature of +43°C after 30 s.

Results

Fig. 5.4 shows the temperature distributions around the electrode with and without blood flow, respectively. In the first case, the voltage necessary to heat the tissue to +43°C is 28.3 V, while in the other case it is 19.5 V (-31%). Without the flow, the temperature distribution is practically spherical, while it has the shape of a meniscus when the flow is considered. The departure from a pure spherical distribution in the former case is due to the eccentricity of the SAR (refer to the top of Fig. 5.2 for an illustration of the SAR). The point of maximum temperature is deeper (by about 0.5 mm) and the electrode is colder when the blood flow is considered (12°C compared to 40°C).

Discussion

These results show that both from the point of view of the applied power and the lesion geometry, the cooling effect of the blood flow is very significant. In the above example, twice as much power is necessary to produce the same maximum tissue temperature when blood flow is considered. It can also be said that the effect of the blood flow is to push the heat pattern deeper inside the tissue, conceivably resulting in deeper lesions. It is clear that the blood flow is a determinant factor of power and of lesion geometry during ablation. It is expected to be less important when the electrode is inserted deeper inside the tissue.

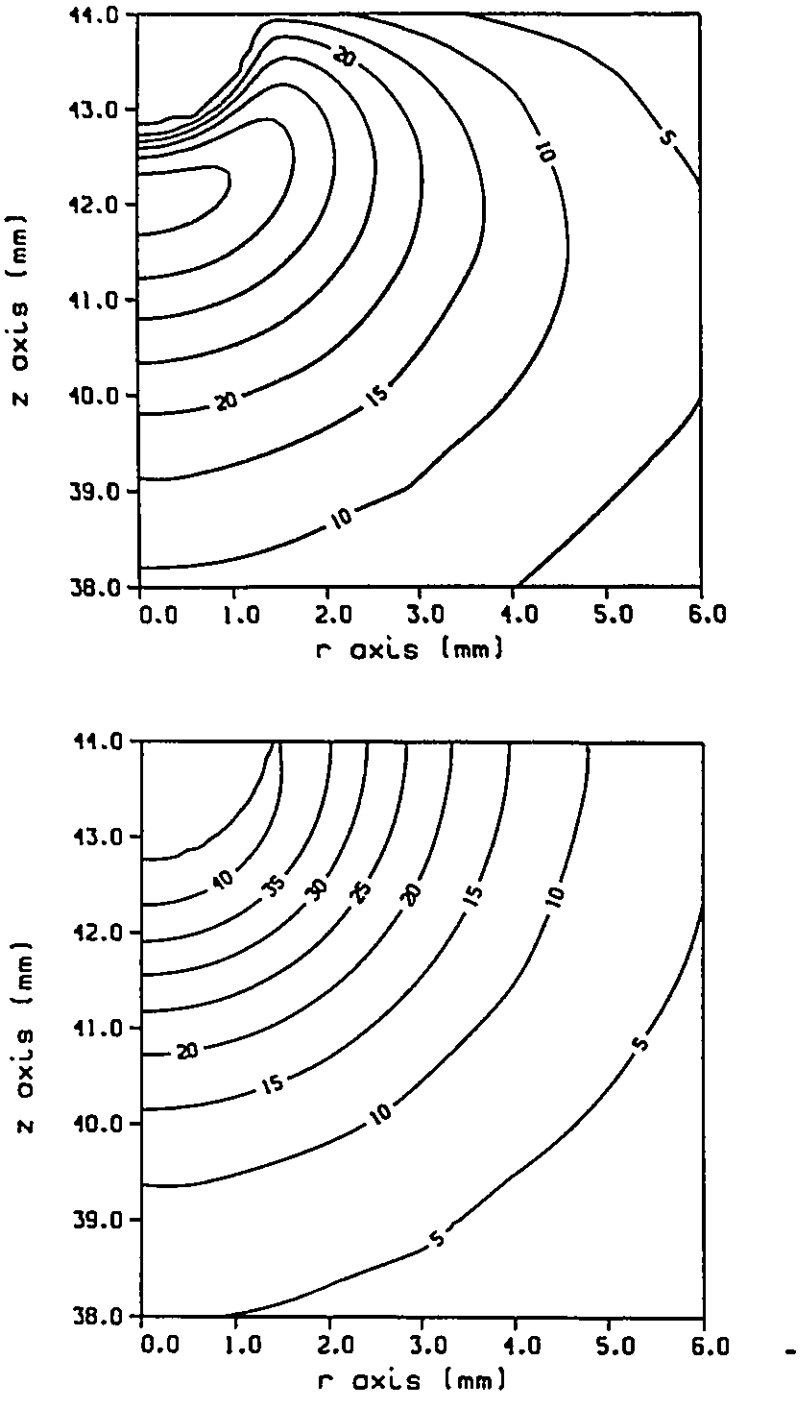

Figure 5.4: Temperature distribution (°C) with and without blood flow. Top: with blood flow ($h = 2000$), 28.3 V, 30 s. Bottom: without blood flow, ($h = 0$), 19.5 V, 30 s.

5.4 Temperature Dependence of the Conductivity

The temperature dependence of the electrical conductivity is approximately +2% $°C^{-1}$. During ablation, temperature elevations of the order of +40°C and more are produced so that at some points, the conductivity of the tissue changes significantly. It is therefore likely that this variation have an influence on the overall process of ablation. In order to evaluate this effect, two simulations are performed.

Procedure

The two simulations consist in heating the tissue by applying a constant voltage of 24.5 V for 30 s. In the first case, the temperature dependence of the conductivity is taken into account while it is neglected in the second case. This means that at every time step, the temperature information is used to update the material properties, and a new SAR distribution is calculated. The geometry is the following: $l = 4$ mm, $r = d = 1.25$ mm, $w = h = 44$ mm.

Results

Fig. 5.5 shows the temperature distributions at $t = 30$ s for each simulation. The overall aspect of the temperature fields is similar, except for the magnitude. With $\sigma(T)$, the tissue reaches +43°C while in the other case, the maximum temperature is no more than 33°C. In both cases the electrode temperature is more or less the same, approximately 12°C. The hot point in the tissue is in both cases located at $z = 42$ mm.

The SAR distributions at $t = 30$ s are shown in Figs. 5.6 and 5.7. The SAR is much more intense (+80%) at the electrode tip when $\sigma(T)$ is considered. The reduction in the resistivity of the tissue has the effect of concentrating the current density. The evolution of the electrode resistance is shown in Fig. 5.8. At $t = 0$, it has a value of 93.2 Ω and at $t = 30$ s, 82.5 Ω (-11.5%).

Discussion

As the tissue heats, the electrode resistance diminishes because of the increase in the conductivity. This results in an elevation of the Joule loss and in a relative augmentation of the SAR at the hot points. In the case of interest here, the augmentation is very significant over

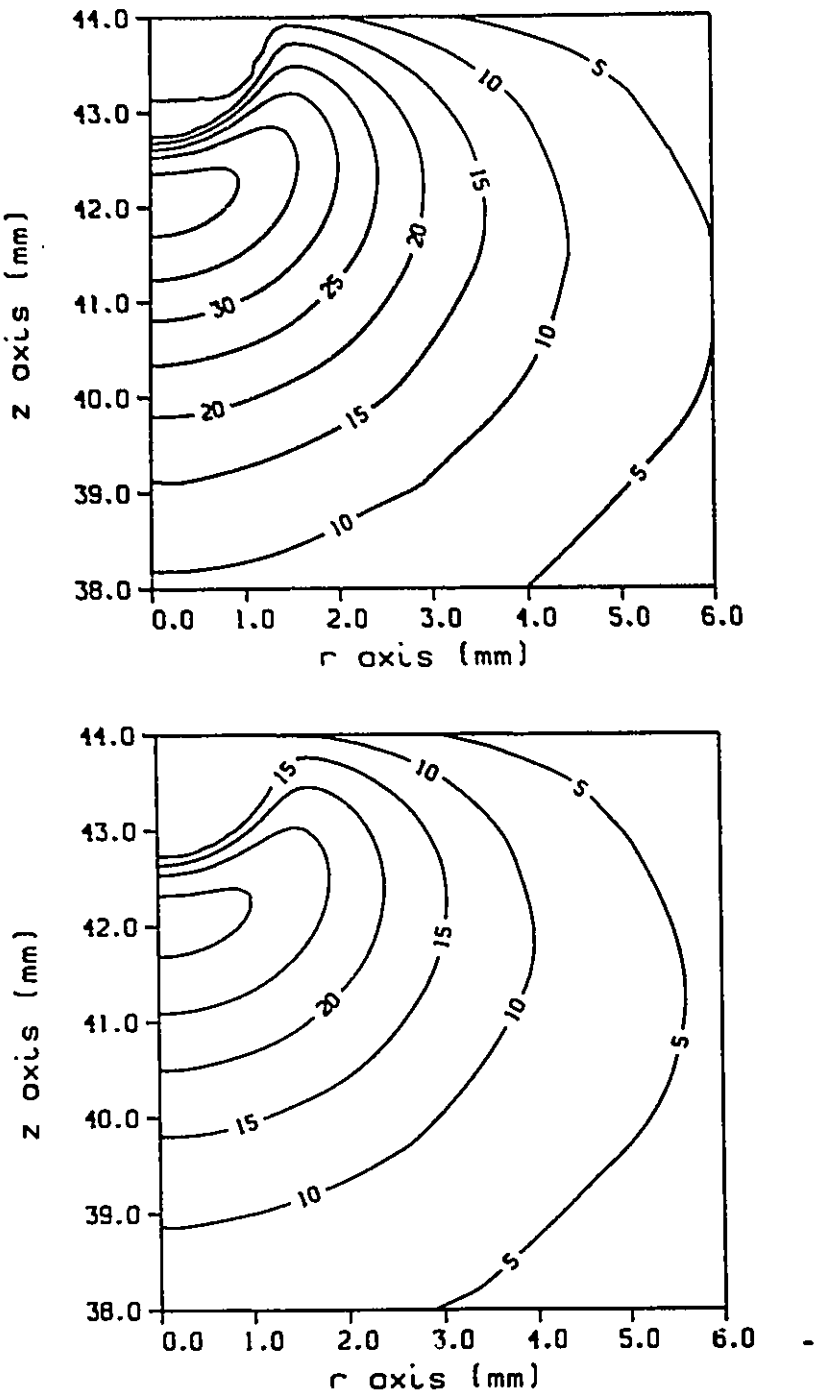

Figure 5.5: Temperature distributions (°C). Top: with $\sigma(T)$. Bottom: with σ constant. In both cases the applied voltage is constant and equal to 24.5 V for 30 s.

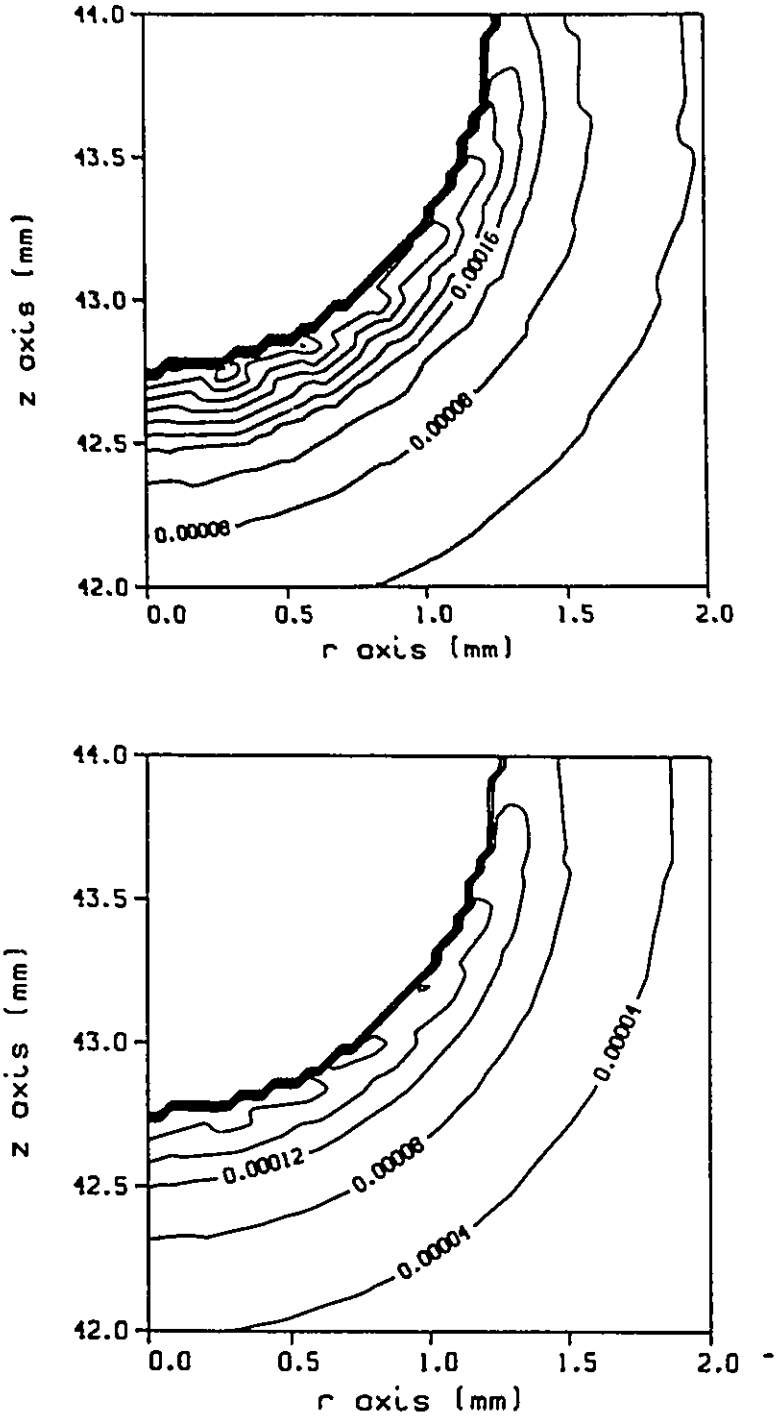

Figure 5.6: SAR distributions (W mm^{-3}) at $t = 30$ s. Top: with $\sigma(T)$. Bottom: with σ constant.

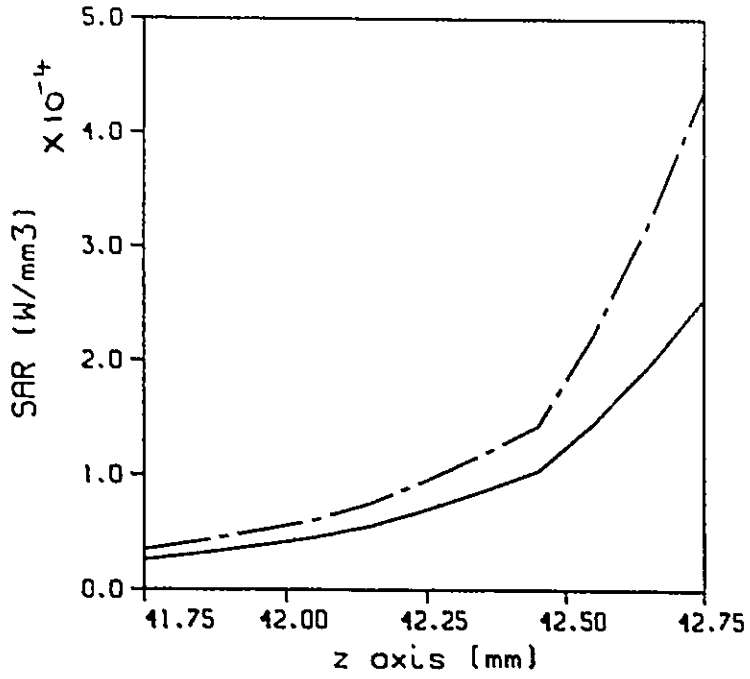

Figure 5.7: SAR (W mm^{-3}) vs position along the z axis at $t = 30$ s with and without $\sigma(T)$). Chain: with $\sigma(T)$. Solid: σ constant.

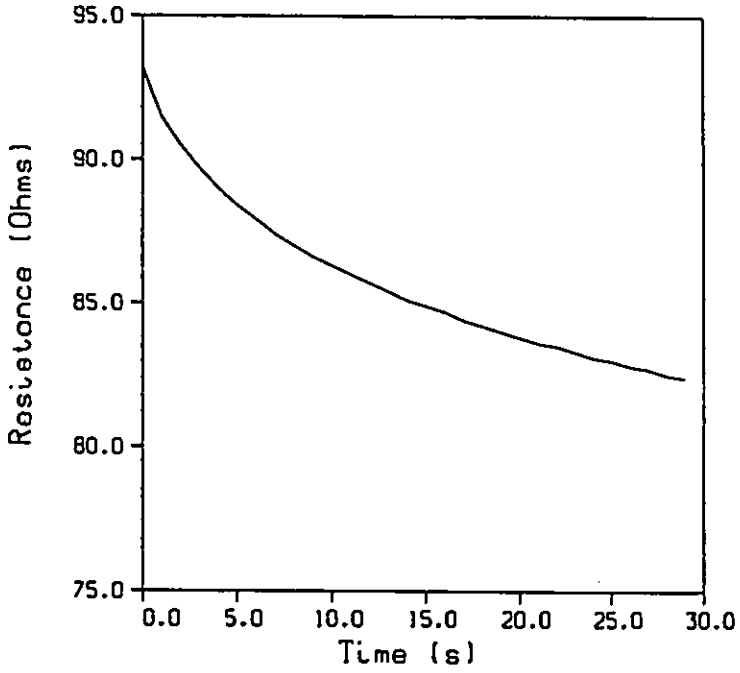

Figure 5.8: Resistance vs time with $\sigma(T)$.

a small region around the tip (roughly within a distance of 0.5 mm). This leads to differences in the tissue temperature.

It is interesting to note that in spite of the important difference in the maximum tissue temperature, the +5°C isotherm is similar in both simulations. This illustrates the fact that in an axisymmetric problem like this one, the incremental heating at larger values of the radius is increasingly difficult. The reason is that the corresponding incremental volume to be heated is increasingly larger.

In view of these results, it appears necessary to consider the temperature dependence of the electrical conductivity, even though this significantly complicates the calculations.

5.5 Conclusion

This chapter presented the results of a number of preliminary simulations, aimed at defining the determinant factors in the model of ablation. First, the appropriate dimensions have been determined. It was found that for large dimensions, the SAR around the electrode tip did not vary significantly. The particular dimensions $w = h = 44$ mm retained in this study are in agreement with those found in reality in humans and at the same time offer an acceptable limit to the model size.

Secondly, the issue of boundary conditions was addressed. A Neumann boundary condition at the heart-blood interface in the electrical problem facilitates the modeling, because it allows the use of the same FEM grid as for the thermal problem. However the simulations showed that this simplification is invalid, and that the blood surrounding the electrode must be considered. It was also shown that this blood layer need not extend beyond the root of the electrode for an accurate evaluation of the SAR at the tip.

In the thermal problem, the boundary at the electrode root was considered as a convective boundary. Calculations done using various values of the heat transfer coefficient were undertaken to determine an adequate value. It was found that a value of 500 W m^{-2} $°C^{-1}$ is reasonable.

Thirdly, the cooling effect of the blood flow was assessed. It is now clear that it is a determinant factor in the ablation process because of its incidence on the required power and the temperature distribution.

Finally, the significance of including the temperature dependence of the conductivity in

the calculations was investigated. The results show that it has a strong effect on the maximum tissue temperature and the power level, and therefore must be included.

With these preliminary considerations, enough confidence in the model has been acquired. The next step is to apply it to study RF ablation.

Chapter 6

Theoretical Modeling III: Study of RF Ablation

One of the difficulties in characterizing RF ablation is the large number of parameters which play a significant role in the procedure. Our investigative approach is to isolate the individual effects of these parameters. To do that, a control simulation with standard conditions of operation is compared with one where only the parameter of interest is varied. Many of those parameters are considered including the electrode geometry and the maximum tissue temperature.

The basis for comparisons is the lesion that is produced and the electrode resistance, both as functions of time. But in all cases these are very strongly dependent on the level of electrical heating that is applied. In order to establish a meaningful foundation for all comparisons, it is necessary to define the voltage excitation that is used. This is explained in details in the first section on voltage modulation.

The lesions produced by RF ablation are more or less ellipsoidal in shape. Accordingly, lesion volume is approximated with the expression for ellipsoids which is V = 4/3 $\pi(abc)$ where a, b, c are the lengths of the semiaxes. Because of the axial symmetry of the numerical model, these correspond to D/2, W/2 and W/2 where W and D are the maximum width and depth respectively.

An effort was made to present the simulation results on plots that have uniform horizontal and vertical scales where possible. This facilitates direct comparisons between different sets of conditions of operation.

The first section of this chapter is a discussion on the modulation of the applied voltage

during ablation. It is followed by the presentation of the control simulation. After that, a section is devoted to the comparison between ablation with a hot-tip catheter and RF ablation. This convincingly demonstrates that the latter approach is much superior.

The next section presents a study of the electrode geometry: the radius, length and shape are considered. Following that is a section investigating various aspects of ablation with a constant applied voltage. This particular electrical excitation is interesting because it is simple to implement in practice.

The following two sections study the effects of the maximum tissue temperature and the depth of the electrode inside the tissue. Then follow a section summarizing the simulation results and recommendations for the optimization of RF ablation.

It is important to mention that only the conditions of operation that are compatible with the clinical application of the RF ablation technique are considered in this study.

6.1 Voltage Modulation

A useful way of comparing different conditions of ablation is to consider the largest possible lesion that can be produced in each case. The mechanism by which a lesion grows in the tissue is thermal conduction. Heat from a hot area flows to the colder surrounding tissue to rise its temperature. Thus, the largest lesion that can be produced is when the maximum tissue temperature (MTT) is maintained at its highest acceptable level during the whole heating period. In this case, heat flow from the hot spot to its neighborhood is as large as possible and the resulting lesion is maximized at all times. Of course, the location of the hot spot itself may vary with time according with thermal transfer phenomena.

In our case, the highest MTT that may be applied is 100°C (an increase of +63°C with a basal temperature of 37°C). Beyond this value, tissue boiling and charring occurs and a corresponding sudden increase in the resistance of the electrode-tissue interface limits any further lesion progression.

In order to maintain the MTT at the desired level at all times, the applied voltage must be properly modulated. Initially, it must be high to rapidly heat the tissue. It is then gradually decreased to reach a steady state where the Joule loss just cancels the heat lost by conduction and convection through the boundaries. The optimum voltage function can be determined only in real time during ablation and using a knowledge of the current MTT.

This is possible during a simulation but unfortunately not experimentally. However since this modulation produces the largest possible lesion at all times, it provides a convenient standard for comparing different conditions of ablation. In this study, this approach is used. For all the different conditions of operation of interest, the optimum voltage function is obtained and the largest possible lesions are compared.

Any voltage function (such as a pulse train for instance) that does not maintain the MTT at the desired level at all times, produces a suboptimal lesion. These functions are therefore not of interest and no further study of them seems justified at this point. However the special case of a constant voltage may be interesting from a practical point of view because of its simplicity. Hence it is investigated later in this chapter.

6.2 Control Case

As mentioned above, the approach used in this study is to isolate the parameters of ablation one at a time and to establish comparisons between a control case and the simulations where the isolated parameter is varied. The control case which forms the basis for comparison is described in this section. It uses a 7,5F electrode which is representative of the clinical reality.

Procedure

The arrangement is similar to the one illustrated in Fig. 5.1. It consists of a hemispherical tip electrode with $l = 4$ mm and $r = d = 1.25$ mm. The block of tissue has dimensions $w = 44$ and $h = 44$ mm. Calculations are made using a time step of 1 s. The applied voltage is modulated so as to produce the largest possible lesion. This is accomplished by adjusting the voltage in order to maintain the MTT at $\approx +63°C$. Because the simulations are time consuming ($\approx$ 2 minutes per time step), the applied voltage is only updated every 5 s. The MTT is therefore $\approx +63°C$ at $t = 5, 10, 15, \ldots$ s.

Two simulations are performed. In the first one, the voltage is turned off at $t = 60$ s, and the cooling phase is observed until $t = 70$ s. In the other case, the voltage is applied for 120 s, in order to show the trend in the evolution of the lesion. The temperature distribution, the resulting lesion depth and width and the electrode resistance are recorded periodically during the simulations.

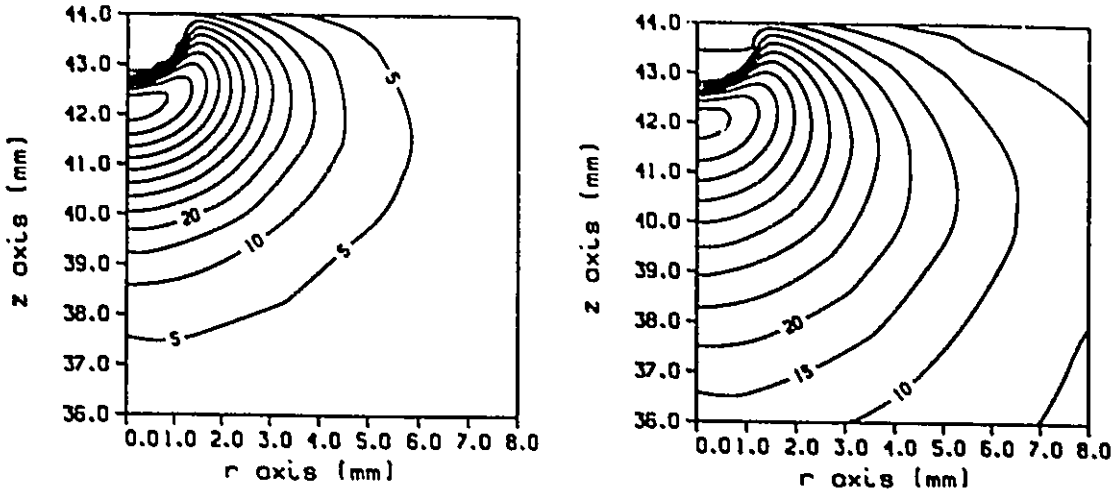

Figure 6.1: Temperature distribution at t =10 (left) and 60 s (right) for the control case. The electrode tip is the top left corner.

Results

The simulation results are presented in Figs. 6.1, 6.2, 6.3, 6.4 and 6.5. Fig. 6.1 shows how the temperature distribution evolves between 10 and 60 s. The isotherms are in the shape of a meniscus. The hot spot in the tissue is $\approx$ +63°C as desired, and is located away from the electrode tip. The tissue surface is relatively cold due to the presence of the flow. For the same reason, the electrode is 40°C colder than the adjacent tissue.

The distribution of the lesion factor at t =10 and 60 s is illustrated by the contour plots of Fig. 6.2. Let us remind here that this factor has a value between 0 and 1 and that below 0.5 the lesion is reversible. In this research we consider that the lesion border is the 0.5 contour. The distance between the 1.0 and the 0.5 contours gives an indication of the lesion sharpness. Sharpness is seen to decrease sensibly with time, from about 0.2 mm at 10 s to 0.3 mm at 60 s. The lesion depth (D) is measured from the tissue surface at z = 44 mm, and the lesion width (W) is measured where it is the largest. At 60 s, D=6.97 and W=9.96 mm.

The temperature vs depth on the z axis is shown at various times in Fig. 6.3 (voltage off at

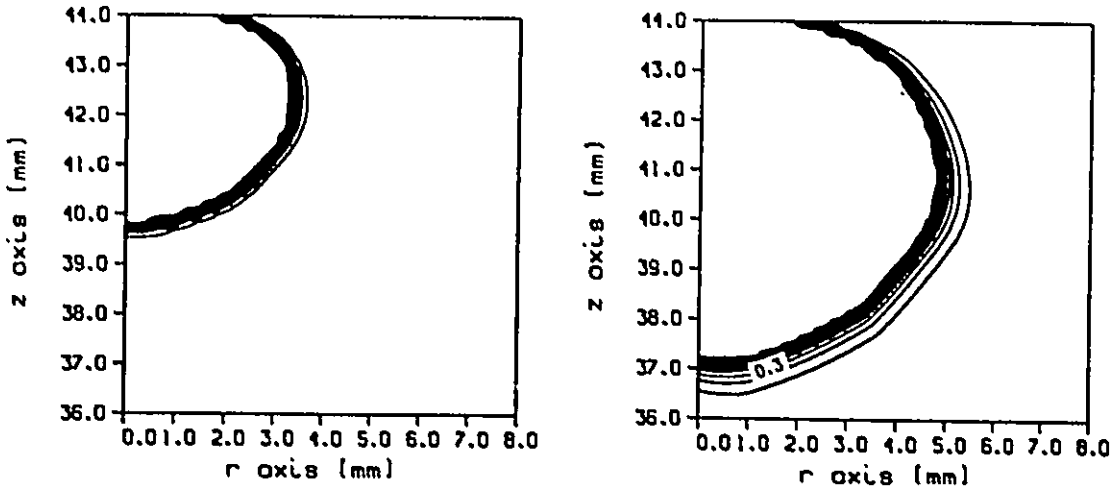

Figure 6.2: Lesion function at t =10 (left) and 60 s (right) for the control case. Lesion function varies between 0 and 1. Contour interval = 0.1.

t = 60 s). The difference in temperature between the MTT and the electrode is in the order of 40°C. The hot spot is located at a depth of around 2 mm in the tissue, that is 0.75 mm below the electrode tip. As heating proceeds, the hot spot moves slightly towards larger depths. As a consequence, the electrode temperature also decreases, by about 2°C. When the applied power is turned off at t = 60 s, the tissue temperature drops rapidly, especially close to the surface because of the flow. The MTT at t = 65 and 70 s is approximately +38 and +28°C respectively, compared to +62°C at t = 60 s. During the cooling phase, the temperature increases very slightly at depths larger than 8 mm.

Fig. 6.4, shows the electrode resistance and the applied voltage vs time. The resistance decreases continuously during heating, reflecting the increase in the tissue conductivity (93.2 Ω at t = 0 to 75.5 Ω at t = 60 and 74.6 Ω at t = 115 s). The change is most pronounced in the first 5 s. A sharp increase in the electrode resistance accompanies the cooling phase (85 Ω at t = 70 s). The applied voltage is initially high (40 V) in order to heat the tissue to $\approx$ 63°C within 5 s. It is then decreased to avoid excessive heating. The rate of change is also high initially (-25% at 5 s) and gradually decreases with time. Between 60 and 120 s the

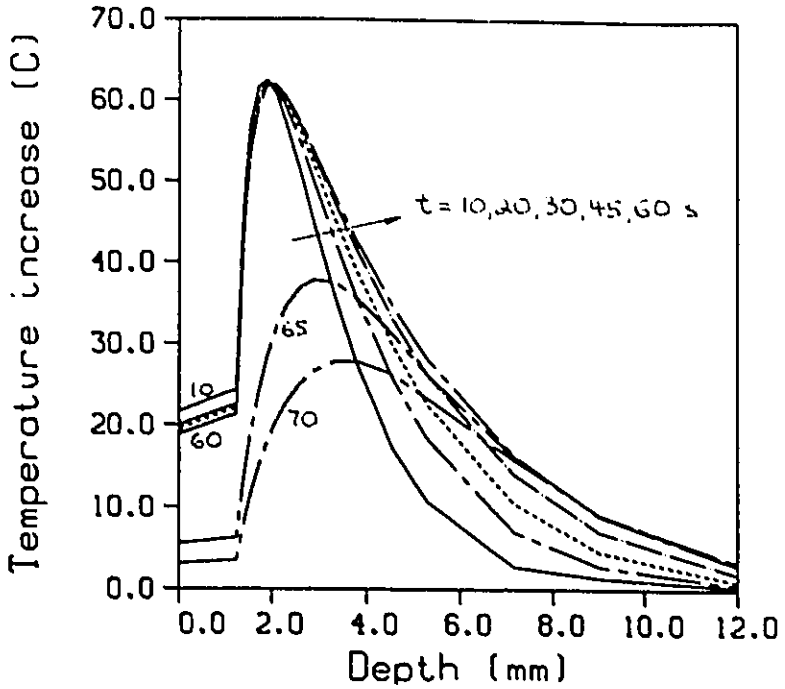

Figure 6.3: Temperature vs depth on the z axis between 10 and 70 s. Voltage is turned off at $t = 60$ s.

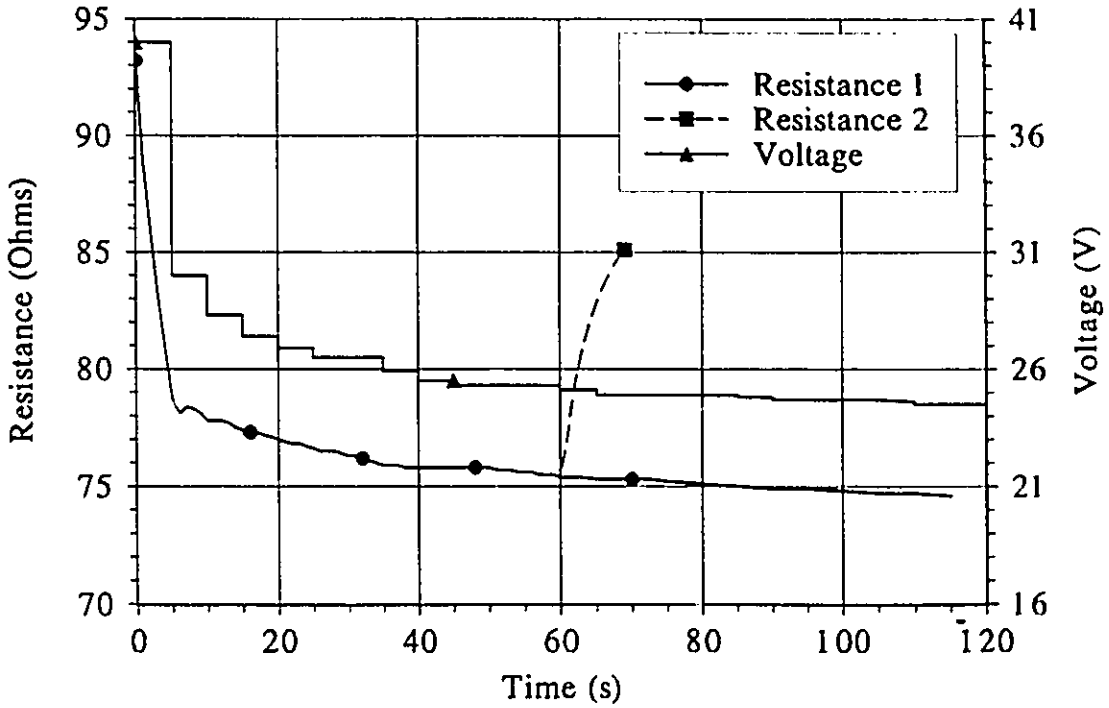

Figure 6.4: Applied voltage and resistance from 0 to 120 s. The case where the voltage is turned off at $t = 60$ s is also shown as Resistance 2.

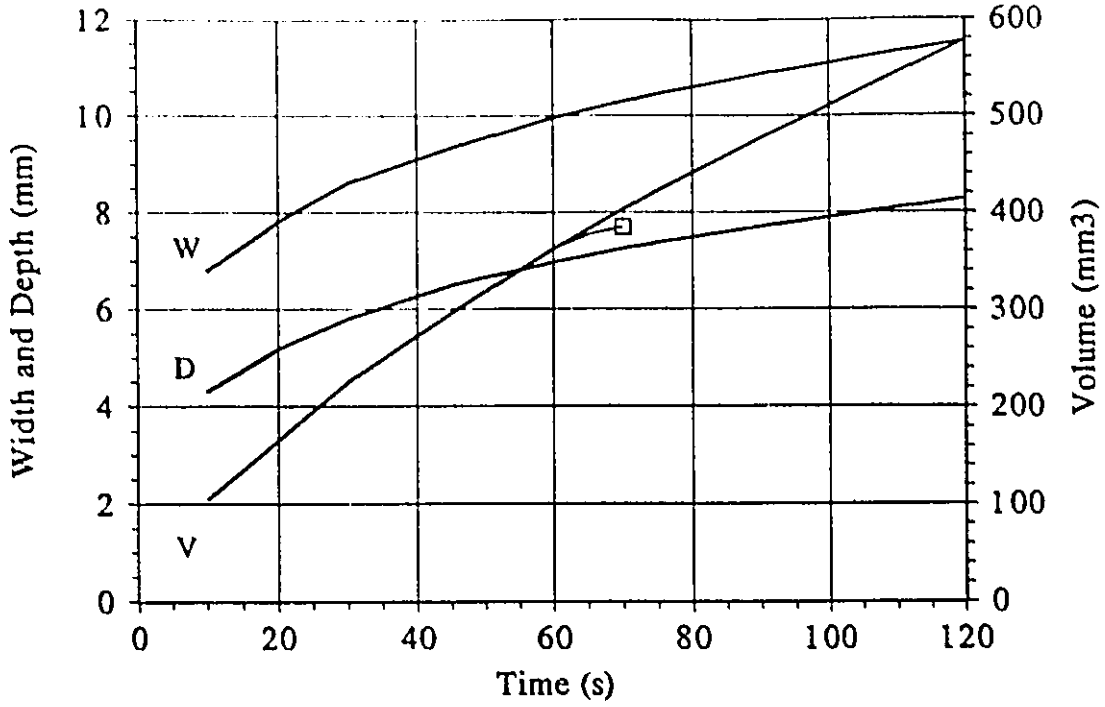

Figure 6.5: Width (W), depth (D) and volume (V) of lesion vs time. The lesion volume at 70 s when the voltage is turned off at t = 60 s is also shown by the square.

voltage is practically constant around 25 V (63% of the value at 0 s). The electrical power at 0 and 60 s is 17.2 and 8.5 W respectively.

The lesion depth (D) and width (W) obtained during the simulations are plotted against time in Fig. 6.5. The lesion volume (V) is also shown in the same figure. At t = 10, 30 and 60 s, V is 100, 208 and 328 mm^3, respectively. The lesion growth rate decreases as time progresses (6.7 mm^3 s^{-1} at t = 10 s and 2.75 mm^3 s^{-1} at t = 120 s). Even after voltage is turned off, the lesion keeps enlarging slightly.

Interpretation of the Results

Due to the smallness of the electrode, the energy is deposited in a thin layer of tissue around it. Part of the energy is absorbed locally, and the remaining flows by conduction to the adjacent tissue and metallic electrode, and by convection to the flow. Initially, the applied voltage needs to be high to rapidly raise the MTT to the desired value, and at the same time to compensate for the heat lost by conduction. As time progresses, the voltage must be decreased towards a value that yields the desired MTT at steady-state. An additional reason

for the necessary reduction in the applied voltage is that the dissipated energy for a given voltage increases with the tissue temperature (because of the increase in σ). This is clearly illustrated in Fig. 5.7, p. 81 where the SAR after heating is significantly higher than initially.

To gain insight into the heating process, let us consider the steady-state. At steady-state all the energy dissipated inside the tissue flows out through the convective and the Dirichlet boundaries. The temperature distribution is delicately adjusted to maintain this state of affair. In a non-linear problem like this one, it is not possible to compute the steady-state temperature directly. The reason is that the power distribution varies with time. However as an approximation, let us directly calculate a pseudo steady-state[1] with the simplification that the power distribution is constant and equivalent to that obtained at $t = 120$ s in the above simulation. This distribution includes the effect of the elevated σ in the hot areas of the tissue. In order to obtain a MTT of +63°C at the pseudo steady-state, the applied voltage must be 24 V. This means that all the energy dissipated by the 24 V source is going out of the domain through the boundaries. The real steady-state certainly requires a voltage slightly lower than 24 V because of its own higher SAR distribution. All this is in agreement with the voltage modulation presented in Fig. 6.4 which has a slightly higher value of 24.5 V at $t = 120$ s.

The displacement of the hot spot inside the tissue is a consequence of the reduction in the applied voltage. Since the immediate surroundings of the electrode are heated directly by the heat source, a reduction of it necessarily entails a temperature reduction. As a consequence, the electrode temperature also decreases. It is important to note the large difference between the temperature of the electrode and the MTT. It is due to the high thermal conductivity of the platinum compared to the tissue. Clearly, the electrode temperature by itself is not a good measure of the tissue temperature.

It is also of interest to examine the evolution of the temperature after power is turned off at $t = 60$ s (Fig. 6.3). Clearly, convective loss to the flow is largely responsible for the rapidity of the cooling. This effect is even more pronounced because of the smallness of the hot spot which globally does not contain much thermal energy. Heat conduction from the hot areas to the surroundings is still present and is illustrated by the modest increase in temperature around 8 mm and deeper.

[1]This is easily done numerically by neglecting the $\partial/\partial t$ term in the heat equation p.26.

The electrode resistance drops rapidly during the first 10 s of heating. This illustrates the fact that the vicinity of the electrode has a large contribution to the total resistance. It is evident that, in this setting, the measurement of the resistance alone cannot be a good indicator of the lesion progression because it remains practically constant between 10 and 120 s.

Lesion progression as illustrated in Fig. 6.5 is an interesting set of data. It shows that the combined evolution of the lesion depth and width is such that the resulting volume grows at an appreciable rate for all the duration of the procedure. After voltage is turned off, the lesion even continues expanding but at a progressively smaller rate. This is a consequence of the lesion factor being expressed as a time integral. It is therefore clear that the longer the duration of power application, the larger the lesion, even for durations up to 120 s.

The control case studied in this section provides a good understanding of the phenomena occurring during ablation. Let us now compare the temperature distributions produced by RF ablation and by a hot-tip catheter.

6.3 Hot-Tip Ablation

Hot-tip ablation refers to the use of a catheter with a heated tip to burn undesirable tissue. One can think of direct resistive heating or of a more fancy approach using inductive heating of a ferromagnetic bead [94]. In principle, this method can be used instead of RF ablation. The temperature of the heated tip can be easily controlled which may represent an advantage. The temperature distribution by this technique is compared to that of RF ablation.

Procedure

A simulation is done with an electrode that is maintained at +63°C for 60 s. The arrangement and the dimensions are the same as for the control case discussed above. The electrode is considered as a Dirichlet condition. The heart surface is cooled by the same blood flow as before. The temperature is calculated as a function of time. It turns out to be significantly lower than the one produced by RF ablation in the control case. A second simulation is then carried out with a larger electrode with $r = 2$ mm.

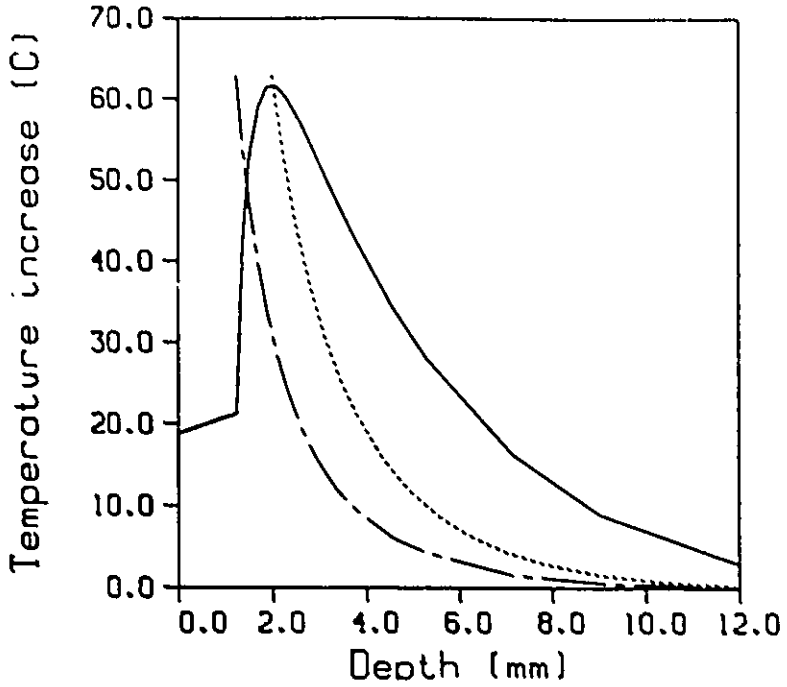

Figure 6.6: Temperature profiles on the z axis for the hot-tip catheters (chain: r = 1.25 mm and dot: r = 2 mm) and the control case (solid) at t = 60 s. The hot-tip catheters are maintained at +63°C.

Results

Fig. 6.6 shows the temperature profiles on the z axis for the hot-tip catheter and the control case at t = 60 s. Clearly, the temperature distribution extends more inside the tissue with the control case than with the hot-tip catheters, even though the MTT is the same in both cases. The simulations show that the distribution with the hot-tip is more abrupt. Even with r = 2 mm, the hot-tip catheter does not heat the tissue as deep as a 1.25 mm RF electrode.

Interpretation of the Results

With a hot-tip catheter, heating only occurs by thermal conduction whereas with RF ablation, energy is directly dissipated inside the tissue. Furthermore, in RF ablation the electrode acts as a heat sink, effectively pushing the hot spot deeper inside the tissue. The two effects combine to produce a higher temperature elevation at depth and conceivably a larger lesion. The results clearly identify RF ablation as a superior approach.

Let us now investigate the influence that a number of parameters have on the lesions

produced by RF ablation. The first parameter of interest is the electrode geometry.

6.4 Electrode Geometry

The geometry of the catheter electrode used for ablation is one of the parameters that can be selected by the operator. In this section we investigate the influence of the electrode geometry on the resulting lesion. A hemispherical tip electrode with different radii and lengths is considered. Also, an electrode with a flat tip is studied.

6.4.1 Electrode Radius

It is recognized in the literature that the lesion size increases with the electrode radius [38, 45, 46]. However, no reliable data is available to quantify the relationship between these two quantities. This issue is considered here.

Procedure

Lesions are calculated for three hemispherical tip electrodes with radii of 1.0, 1.25 (control) and 1.5 mm using the same arrangement as before (Fig. 5.1). These correspond to catheter sizes 6 F, 7.5 F and 9 F. The electrodes all have a length l = 4 mm and are inserted at a depth d = 1.25 mm inside the tissue. The applied voltage on the electrodes is modulated so as to keep the MTT $\approx$ +63°C. As discussed above, for practical reasons, the applied voltage is updated every 5 s. The heating duration is 60 s.

Results

Fig. 6.7 shows the results of the simulations. The lesion is seen to increase in volume with a larger electrode radius. At 10 s, V is 80(-23%), 104 and 132(+27%) mm^3, and at 60 s, V is 274(-24%), 362 and 447(+23%) mm^3 for r = 1.0, 1.25 and 1.50 mm respectively. With r = 1.25 mm the depth and width curves are halfway between those of the other two radii, and so is the volume curve.

A difference in the electrode resistance is observed. Initially, it has values of 101.9, 93.2 and 86.5 Ω for r = 1, 1.25 and 2.5 mm respectively. As heating proceeds, the evolution of the resistance in the three cases parallel each other. After 60 s, the resistance values are 82.5, 75.5 and 70.3 Ω, in all cases 81% of the initial value. The voltage necessary to produce a

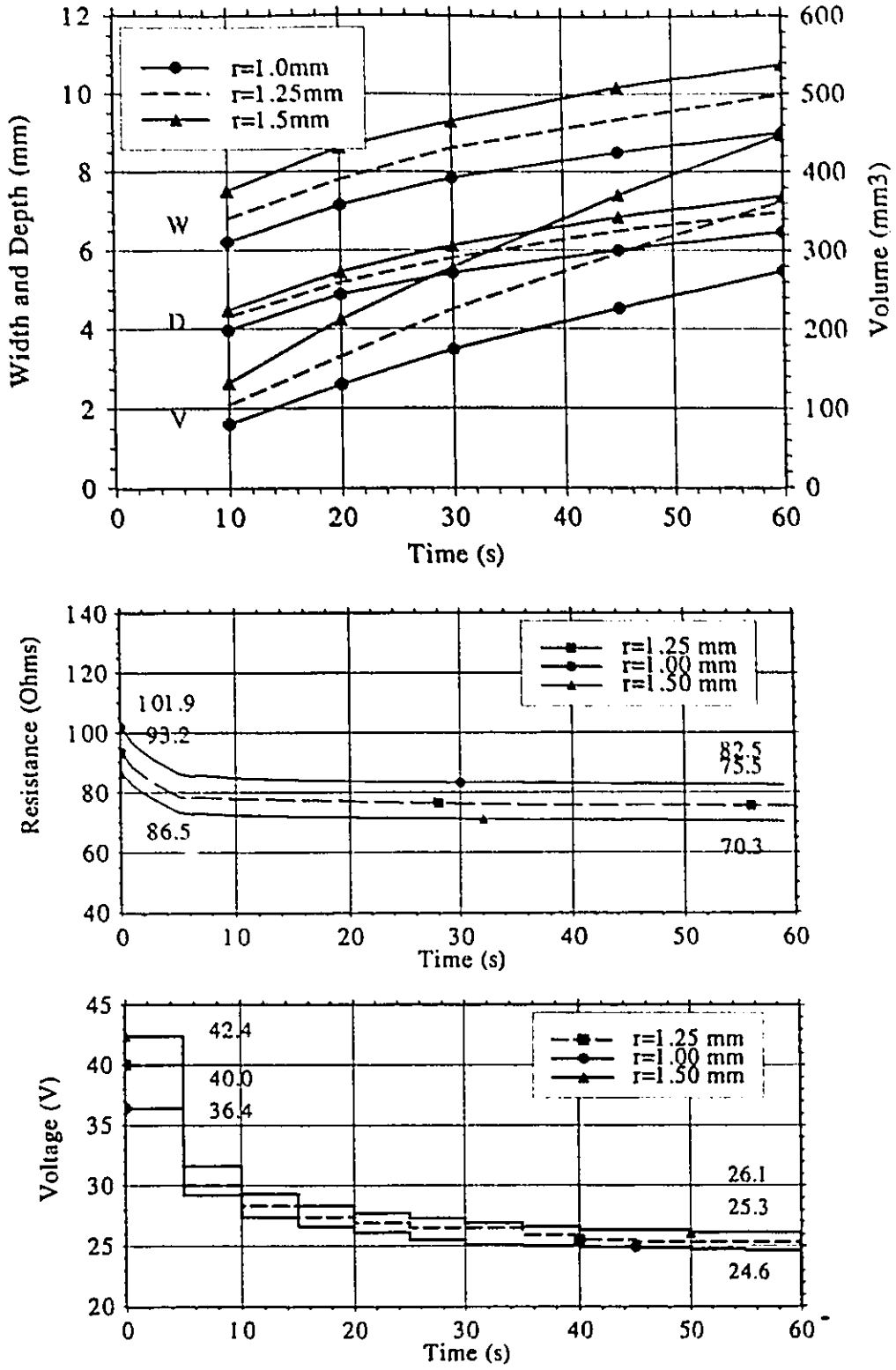

Figure 6.7: Results vs time with various electrode radii (r). Top: lesion width (W), depth (D) and volume (V). Middle: electrode resistance. Bottom: voltage.

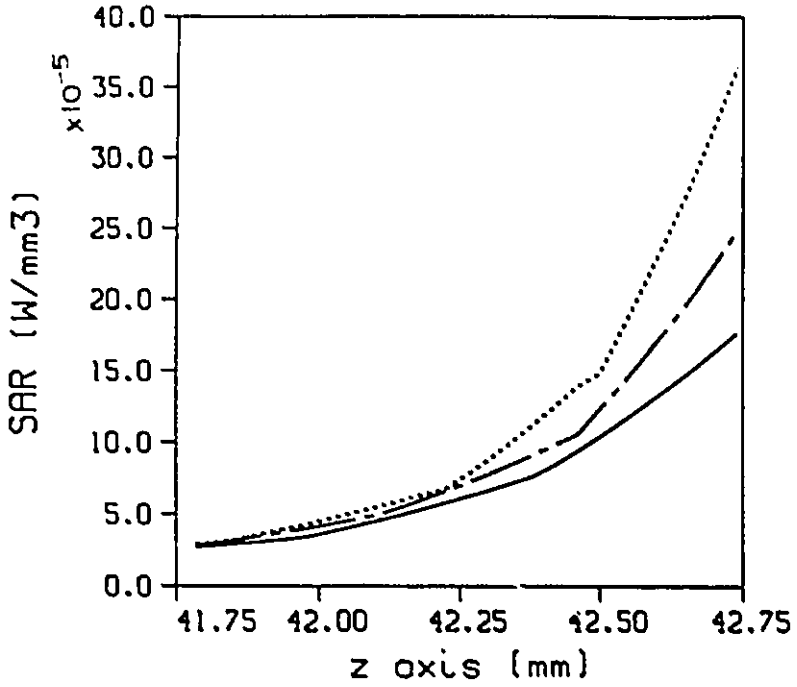

Figure 6.8: SAR profiles at $t = 0$ for electrodes with different radii. Solid: $r = 1.5$ mm. Chain: $r = 1.25$ mm (control). Dot: $r = 1.0$ mm. Notice how the levels are different at $z = 42.75$ mm but similar at $z = 41.75$ mm.

constant MTT is higher when the radius is enlarged and obviously related to the change in resistance. The optimum voltage functions are all similar. The voltage assumes its highest value at the onset of ablation and is progressively reduced afterwards. The rate of change is the highest at 5 s (-20 to -25%) but rapidly diminishes. At 60 s, the voltage is between 60 and 70% of its initial value.

Interpretation of the Results

There are two reasons for the lesion to be larger when the electrode radius increases. First, the contact area with the tissue is enlarged so that the electrical current flows over a larger surface (and the resistance diminishes). Consequently heating occurs over a larger volume. Second, because of the increased radius, the SAR at the electrode tip decreases less abruptly with distance away from the electrode. This is shown in Fig. 6.8. This results in energy deposition that is proportionally deeper inside the tissue with an electrode of larger radius.

The amplitude of the SAR at the electrode surface is reduced when the radius is enlarged.

This explains why, in order to maintain a given tissue temperature, a higher voltage must be applied on a larger electrode. This fact, in conjunction with the reduced resistance, means that the necessary power is significantly larger when a larger electrode is used. At $t = 0$, the power for $r = 1.0$, 1.25 and 1.5 mm is 13, 17.2 and 20.8 W.

The simulations show that the lesion can be effectively made larger by increasing the electrode radius. The results for intermediate values of the electrode radius can be easily interpolated from the plots.

6.4.2 Electrode Length

The length of the ablating electrode is also a determinant factor of lesion size. The literature contains one report of an experimental study of the effect of electrode length [54]. Its conclusions are ambiguous but seem to suggest that larger lesions may be obtained with longer electrodes. The issue is resolved here by calculating the lesions produced with electrodes of various lengths.

Procedure

The simulations are performed with three ablating electrodes with $r = d = 1.25$ mm and three different lengths l =2.5, 4 (control) and 10 mm (Fig. 5.1). The largest possible lesion is simulated, using the voltage modulation scheme described before. Power is applied during 60 s.

Results

The results are shown in Fig. 6.9. The lesion volume is seen to increase with the electrode length. Even though at 10 s all lesions are similar in size with 96 (-8%), 104 and 112 (+8%) mm^3, the difference at 60 s is much more important (310 (-15%), 362 and 454 (+25%) mm^3). The lesion size for the control case is closer to the short electrode than the 10 mm one. The calculations show that even after 60 s, the lesions are still progressing, albeit at a slower rate than before. Fig. 6.10 shows the temperature profiles on the z axis for each electrode. Notice how the electrode gets colder as the length increases ($\approx$ 30, 20 and 15°C for l = 2.5, 4, 10 mm).

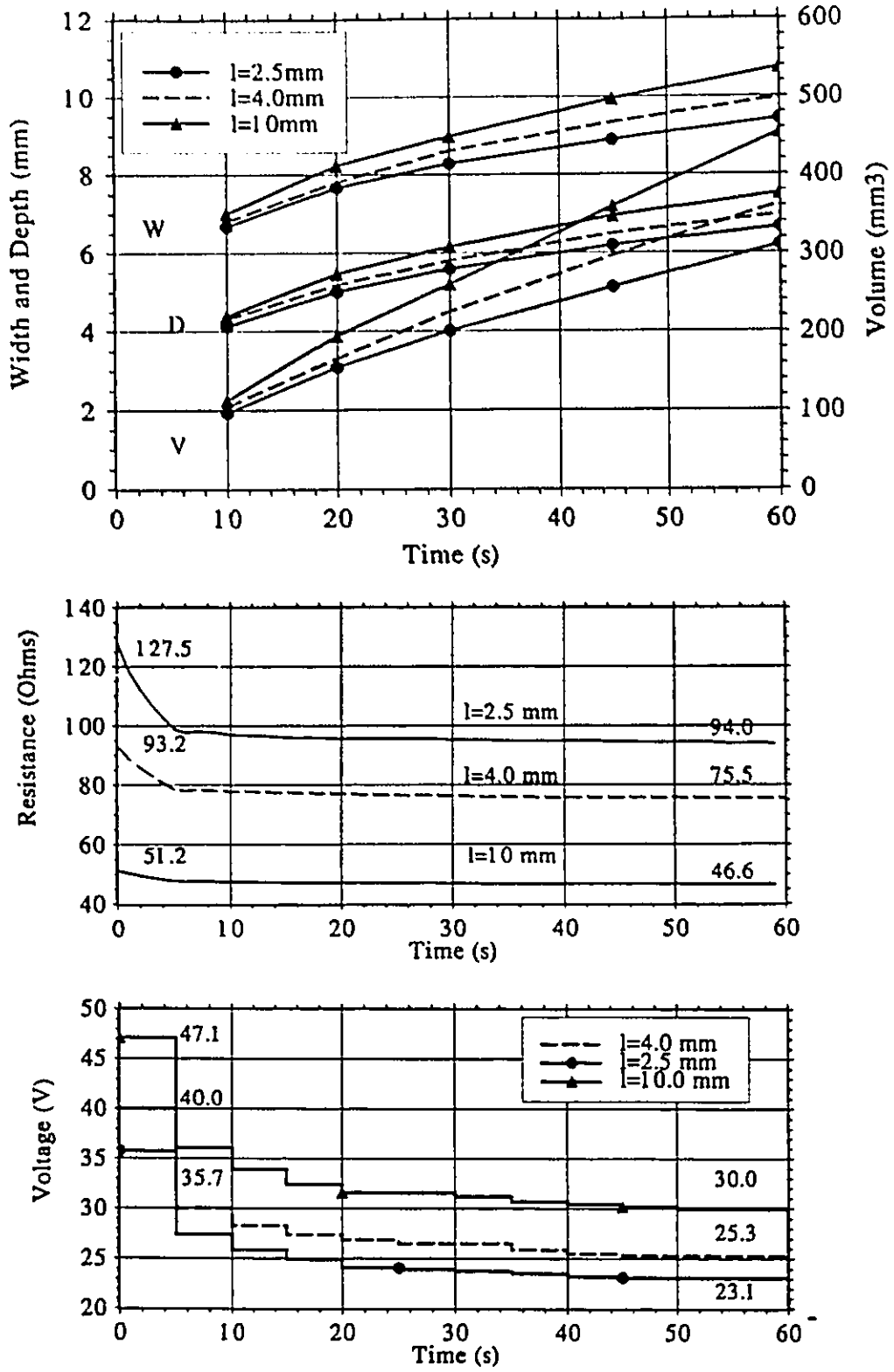

Figure 6.9: Results vs time with various electrode lengths (l). Top: lesion width (W), depth (D) and volume (V). Middle: electrode resistance. Bottom: voltage.

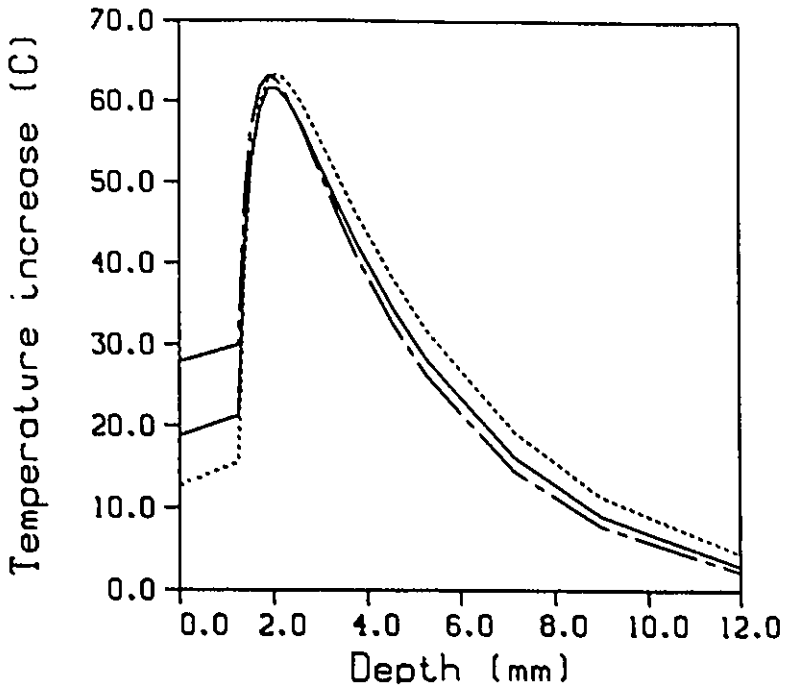

Figure 6.10: Temperature profiles on the z axis at t = 60 s for various electrode lengths. Solid: l = 4.0 mm (control). Chain: l = 2.5 mm. Dot: l = 10 mm.

The resistance values vary largely between the electrodes, the longer ones having a lower resistance. At t = 0, R = 127.5, 93.2 and 51.2 Ω and at t = 60 s, R = 94.0, 75.5 and 46.6 Ω. As seen previously, the electrode resistances decrease as heating progresses. The first 5 s of power application are associated with a much more abrupt resistance variation with the short electrodes than with l = 10 mm. The total resistance variation is more important in percentage for the shorter electrodes.

The voltage amplitude required to maintain the MTT increases significantly with the electrode length (at t = 0, the voltage is 35.7, 40.0 and 47.1 for l = 2.5, 4.0 and 10 mm respectively). The power values at t = 0 are the following: 10.0, 17.2 and 43.3 W for l = 2.5, 4.0 and 10.0 mm. As before, the voltage is reduced as heating progresses in order to avoid overheating. The rate of change is -25% at 5 s and decreases rapidly afterwards. At 60 s, the voltage is approximately 65% of its initial value.

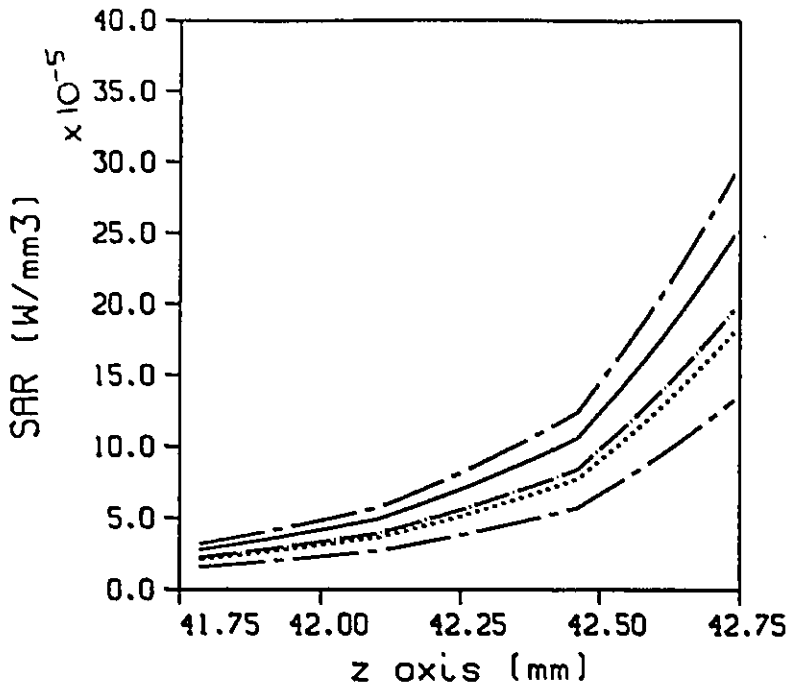

Figure 6.11: SAR profiles at $t = 0$ s for various electrode lengths. Starting from the highest curve, $l = 2.5, 4$ (control), 8,10 (dot curve) and 20 mm. The ratio of one profile over an other one is practically constant for all z.

Interpretation of the Results

Unlike electrode with different radii, electrodes with different lengths have SAR levels which are lower in magnitude but with similar distributions (Fig. 6.11). Therefore the major difference between electrodes of different lengths comes from the difference in the convective losses. Indeed, the longer the electrode the higher the convective loss, the colder the electrode and the deeper (by only a small amount) the hot spot. The resulting lesion is therefore bigger. This effect is expected to saturate with growing lengths. Calculations made with $l = 20$ mm reveal that the electrode temperature is almost the same as with $l = 10$ mm.

The difference in lesion size for the various electrode lengths is minor at 10 s but increases gradually with time. It means that the benefit of using a longer electrode is not obtained for short durations of heating. This is unlike the case where it is the electrode radius that is changed. There, significant differences in the lesion sizes were obtained after only 10 s. The two behaviors are explained by the differing levels of convective loss.

The large variations in resistance between the electrodes studied here is explained by the

difference in their surface areas. Also, long electrodes have a larger portion of their current that flows to the blood, compared to short electrodes whose current is concentrated in the tissue. It means that the variation in the tissue conductivity has a smaller contribution to their total resistance. This explains the observation that the resistance varies less in time for the longer electrodes.

The reduced SAR of long electrodes necessitates a larger voltage in order to produce a given MTT. (The ratio of the SAR's at 0 s is the same as the ratio of the square of the applied voltage.) This, in conjunction with the lower resistance value means that the total power is significantly higher. It is worth noticing that a larger portion of this power is dissipated in the blood when the electrode is longer. In this study it is assumed that the blood flow is large enough that its temperature remains constant. The results show that if enough power is available, the use of a longer electrode produces a bigger lesion. The benefit is not obtained for short durations of application.

6.4.3 Electrode Shape

No studies seem to have been reported concerning electrodes with tips other than hemispherical. Yet it would appear that alternative designs such as an electrode with a flat tip could be compatible with the application in terms of safety and maneuverability. The lesion produced by this new electrode design is calculated here.

Procedure

Calculations are done with two electrodes having $r = d = 1.25$ mm, and $l = 4$ mm. In the first case, the tip is hemispherical (control) while in the other case the tip is flat (the edge has a radius of 0.25 mm). A FEM mesh with very high density is used around the electrode edge to yield good results. The simulations are similar to the ones presented before and are done over a period of 60 s.

Results

The results are shown in Fig. 6.12. After 60 s, the lesions are still progressing, although at a slower rate than before. The lesion is larger (+26% at $t = 60$ s) with a flat tip electrode than with a spherical tip. The flat tip electrode has a resistance that is slightly less (89 vs

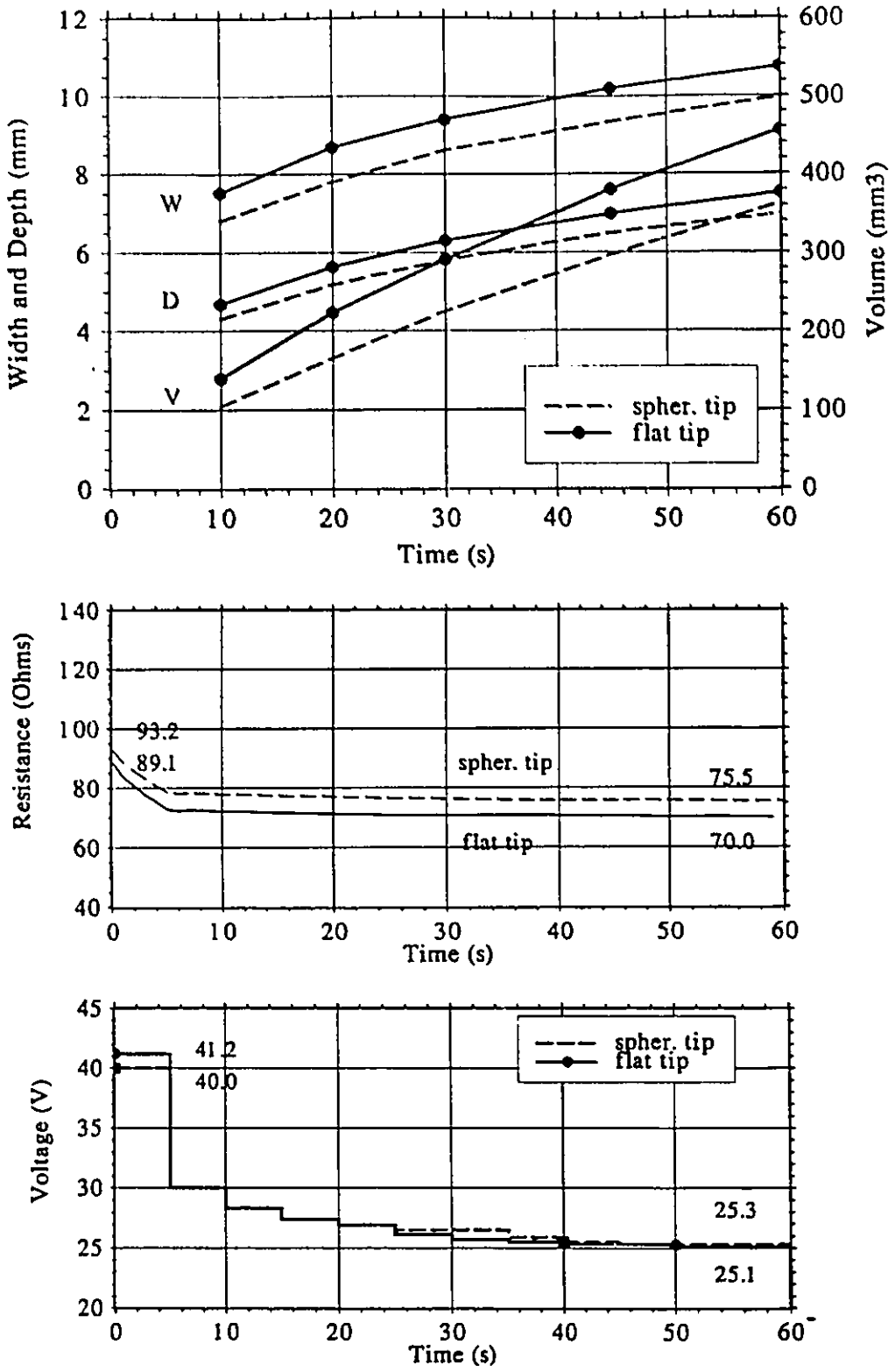

Figure 6.12: Results vs time with flat and spherical tip electrodes. Top: lesion width (W), depth (D) and volume (V). Middle: electrode resistance. Bottom: voltage.

93.2 Ω at $t = 0$) than the control electrode. The voltage functions required in the two cases are virtually the same.

Interpretation of the Results

The difference in lesion size is a consequence of the difference in the SAR distributions. With the flat-tip electrode, a larger portion of the power is deposited around the edge of the tip compared to immediately beneath it (on the z axis). The situation is very similar to increasing the radius to 1.5 mm.

6.5 Ablation with a Constant Voltage

Another aspect of RF ablation that deserves some thoughts is the evolution of the lesion when the applied voltage is constant. Indeed, this approach may be of interest because it is simple to implement in practice. It is not clear if the lesion rapidly saturates or if its size is comparable to the largest possible lesions discussed previously. Calculations are made to answer these questions.

Procedure

Simulations are performed with the same geometry as the control case presented above. In this case however, instead of using a modulated voltage that produces the largest lesion at all times, a constant voltage is applied. Various voltage levels are considered one at a time. For every voltage setting, the heating is stopped when tissue boiling occurs (MTT=+63°C). The lesion size and electrode resistance are recorded periodically. Only heating times smaller than 180 s are considered since longer durations are not applicable in practice. The time steps in these simulations are: v=39.4 V Δt = 0.5 s, v=30.0 V Δt = 1 s, v=26.9 V Δt = 2 s, v=25.5 V Δt = 3 s, v=24.5 V Δt = 3 s.

Results

The results are shown in Fig. 6.13. The voltage is varied between 39.4 and 24.5 V and the time of heating ranges from 5 to 180 s. At all voltage levels, the lesion size progresses practically linearly with time. The largest achievable lesion at each level is indicated by the markers.

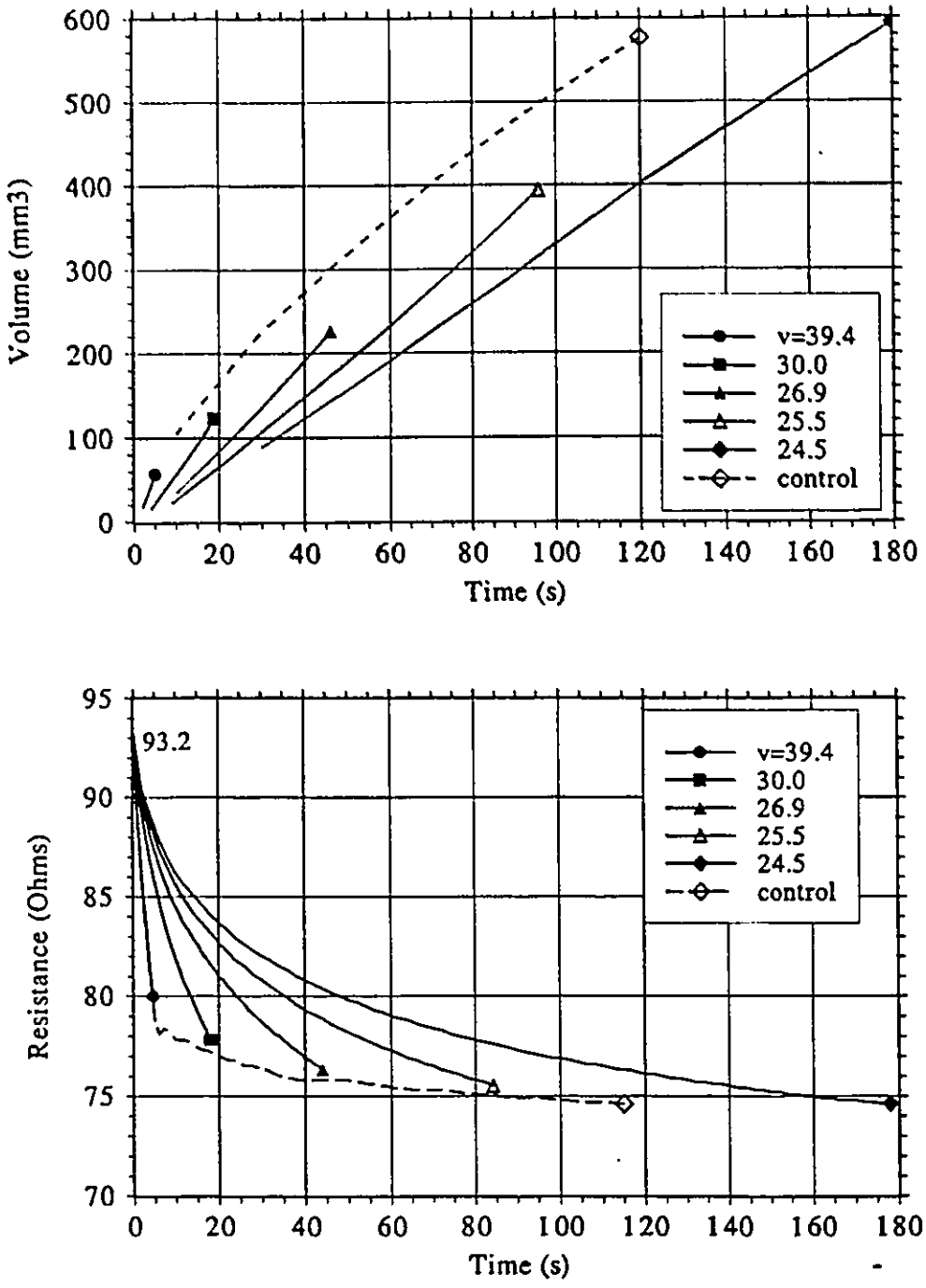

Figure 6.13: Results of simulations with various constant voltage (v) levels. Heating is stopped when the MTT reaches +63°C (point identified by the markers). The control case is also shown. Top: Lesion volume and, bottom: electrode resistance vs time.

This is the point where the MTT=+63°C(for 24.5 V the MTT at 180 s is 61.1 and rising slowly). There is an important difference in the lesions achievable with the different voltage levels. As expected, high voltage causes rapid tissue boiling with limited lesion formation (57 mm^3 after 5 s at 39.4 V). On the other hand, a lower voltage may be applied for a much longer period without causing excessive heating. The resulting lesion grows more slowly but ultimately can be much larger (594 mm^3 at t = 180 s with 24.5 V). The plot also shows the control case which corresponds to the largest possible lesion that can be produced at all times. For t > 20 s, the extent of the lesions obtained with a constant voltage is significantly smaller than the control case (around -20%).

The results show that the resistance decreases monotonically during heating. As expected, the rate of change of resistance is proportional to the applied voltage. At t = 0 s, the resistance is 93.2 Ω in all cases. At the end of the heating sequence, it varies between 74.5 and 80 Ω depending on the voltage. As an illustration of the amount of power required, let us consider the case with 26.2 V. At t = 0, the power is 7.4 W and at t = 60 s, it is 9 W. The change in resistance is responsible for this variation since the voltage is constant. It is interesting to see that the resistance curve for the control case almost coincides with the extremities of all the other curves.

Interpretation of the Results

This set of results is of interest because in practice, it is simple to apply a constant voltage on the ablating electrode. The results are quite clear about the relation between the amplitude of the voltage and the largest achievable lesion. A lower voltage will, after enough time, produce a larger lesion than a high voltage. The reason high voltage lesions are smaller is that thermal conduction is not important enough to dissipate all the heat that is generated locally. There results an excessive temperature elevation close to the electrode and boiling soon limits lesion progression. On the other hand, at a lower voltage, the dissipated energy is conducted away from the electrode and ultimately the lesion grows bigger.

It is worth noticing how a small variation in the applied voltage leads to a large variation in the ultimate lesion size and the time where it is reached. For instance, increasing the voltage from 24.5 V to 26.9 V (+10%) accelerates the heating from 180 to 46 s (-75%) but diminishes the lesion size from 594 to 226 mm^3 (-60%).

Another way of interpreting the results is by considering a fixed duration of heating. Then of course, of all the voltage levels that do not produce boiling within that period, the highest one produces the largest lesion. The difference can be important. Consider a time of 40 s. With 26.9 V, the lesion grows to 191 mm^3. With 24.5 V (-9%), the lesion has a volume of only 125 mm^3 (-35%). A small deviation from the optimum voltage in this case can lead to an appreciable lesion reduction.

As pointed out above, the control resistance curve follows the tips of the other curves. But the electrode resistance is closely related to the temperature distribution around the electrode tip. This means that the temperature distributions at these points must be similar. This is despite the fact that the lesions are very different. It follows that the resistance is not sensitive enough to the lesion size to be a good measure of it.

6.6 Effect of MTT on Lesion Size

In the control case, the largest possible lesion is obtained by keeping the MTT at +63°C which is the point where tissue boiling occurs. In this section we limit the MTT to a lower temperature and observe the effect on the lesion size.

Procedure

The procedure is identical to the control case except that the MTT is limited to +43°C instead of +63°C. The simulation is done over a period of 60 s.

Results

The results are shown in Fig. 6.14. The calculations show that even after 60 s, the lesions are still progressing, but at a slower rate than before. The lesion volume with the lowest MTT is roughly everywhere 50% that of the control case. Both the depth and the width of the lesion are reduced significantly. This difference increases with time. The resistance values after 60 s are 81.3 and 75.5 Ω, again a small difference compared to the lesion difference. The two voltage functions display the same decreasing behavior with time, only their levels differ. For the lowest MTT the voltage varies between 83 and 90% of that for the other case.

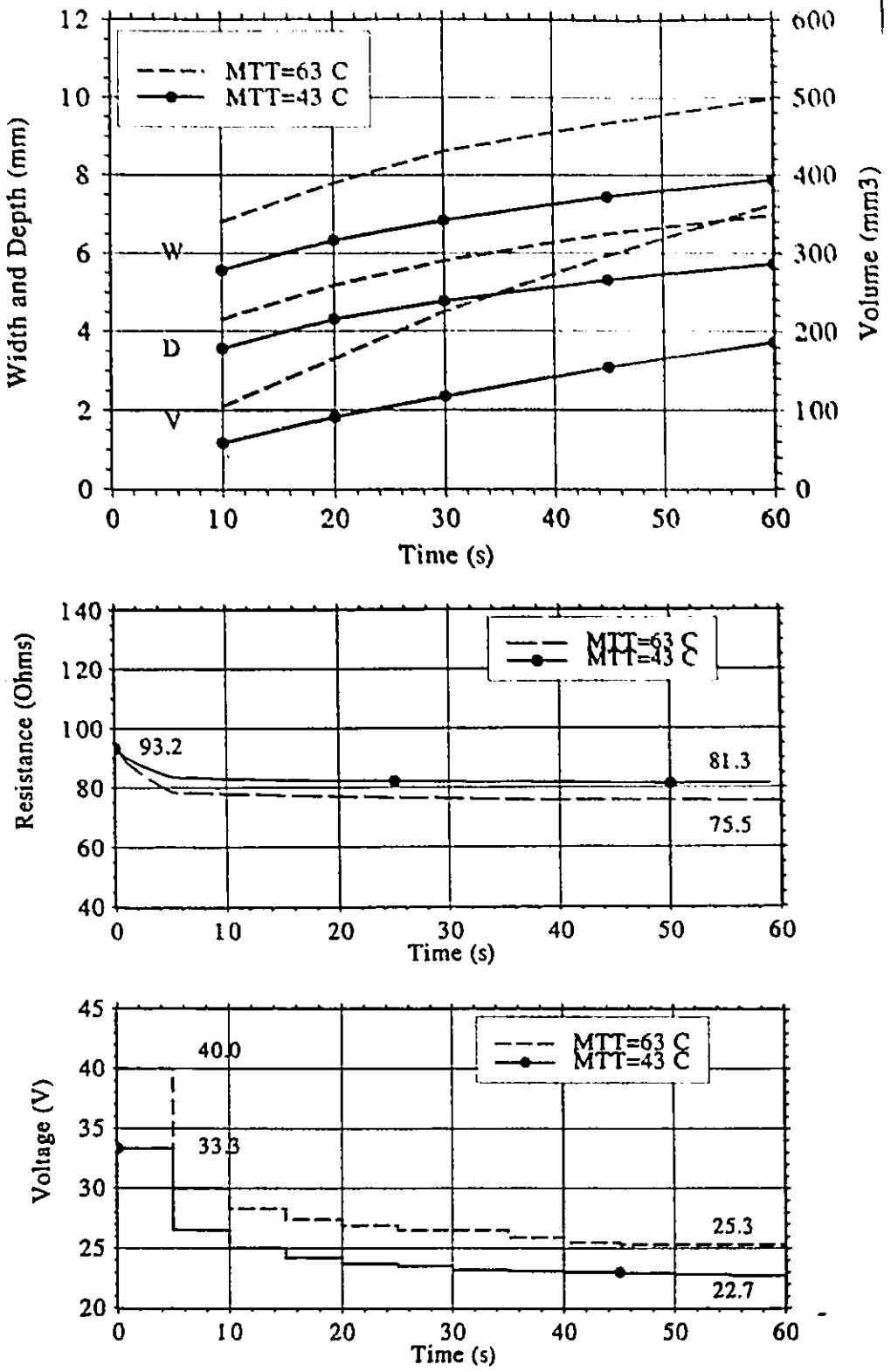

Figure 6.14: Results vs time with MTT = 43°C and 63°C (control). Top: lesion width (W), depth (D) and volume (V). Middle: electrode resistance. Bottom: voltage.

Interpretation of the Results

A temperature increase of +43°C corresponds to an absolute temperature of 80°C in the tissue. Obviously, this is more than enough to produce irreversible damage. Yet, the extent of the lesion is only half of what it is when the MTT is +63°C. This highlights the importance of heating the tissue as much as possible in order to maximize the lesion.

6.7 Effect of Electrode Depth Inside the Tissue

A parameter that certainly has an importance in the process of ablation is the depth at which the electrode is pushed inside the tissue. Unfortunately this parameter is not controllable by the operator. It depends partially on the pressure that is applied on the catheter and partially on the properties of the tissue itself: its toughness and the irregularity of its surface. In order to assess the significance of this parameter, a simulation is performed where the electrode is placed deeper into the tissue than for the control case.

Procedure

The simulation is essentially the same as for the control case except that the electrode tip is 2.5 mm below the tissue surface instead of 1.25 mm. The calculations are done over a period of 60 s.

Results

The results are shown in Fig. 6.15. Both the depth and the width of the lesion with the deep electrode are larger than the control case. The lesion with the deep electrode is 65% bigger at 10 s and 53% bigger at 60 s than the control case. The electrode resistance is initially 97 Ω, 4% more than the control case. However after heating, its value decreases to 68.8, compared to 75.5 Ω for the control. The necessary voltage is lower for the deep electrode than for the control case. Again, it is initially high (37.4 V), drops by 25% at 5 s, and gradually stabilizes to its lowest value (22.5 V, 60% of initial voltage).

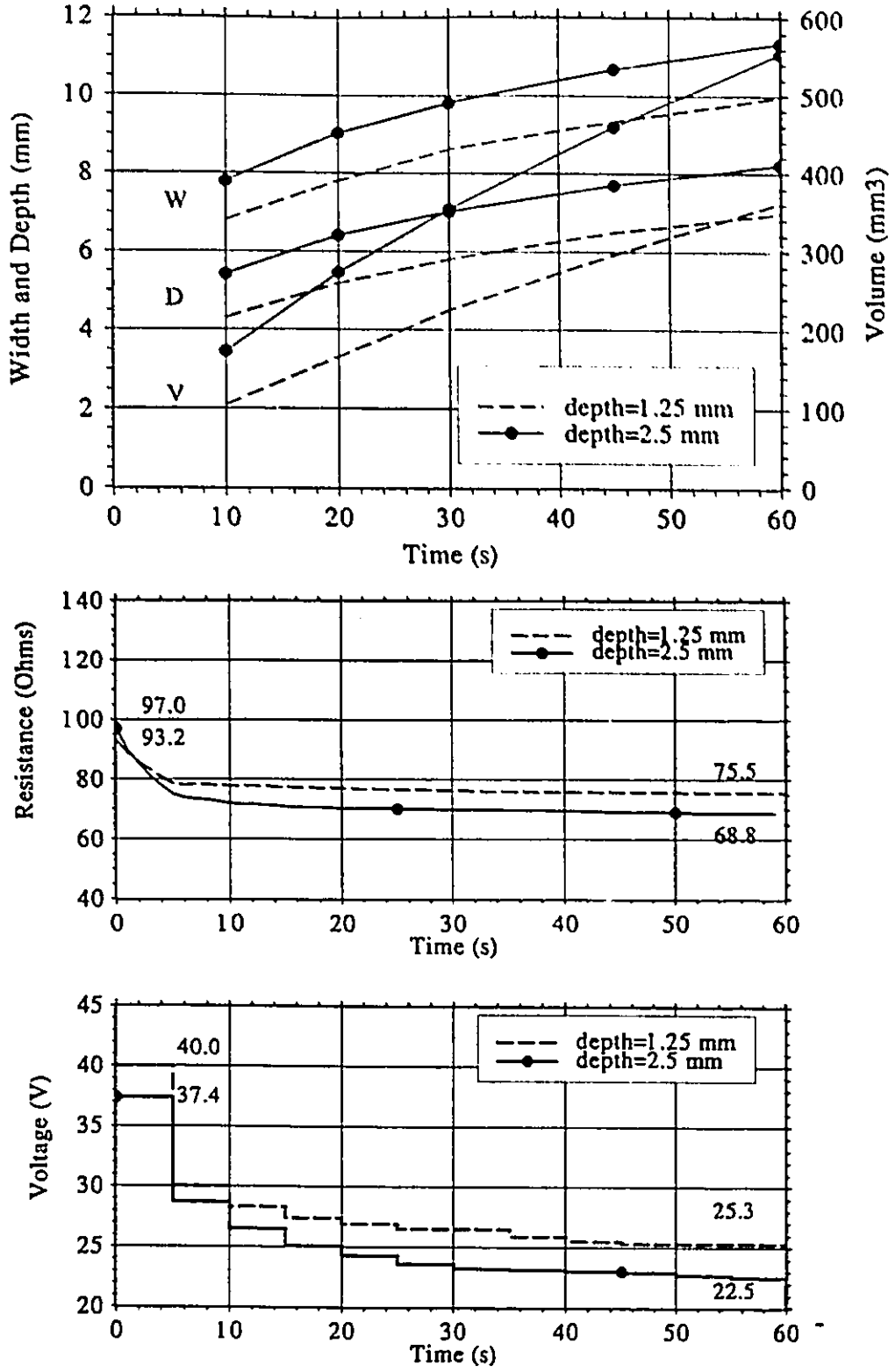

Figure 6.15: Results vs time with electrode depth d=1.25 mm (control) and d=2.5 mm. Top: lesion width (W), depth (D) and volume (V). Middle: electrode resistance. Bottom: voltage.

Interpretation of the Results

When a given electrode is pushed deeper inside the tissue, the SAR distribution at the tip is not significantly changed. This is because the conductivity of the blood and the tissue are relatively close in value. Therefore, this cannot not be the cause for the difference in lesion size observed here. On the other hand when the electrode is deep the hot spot created in the tissue is not confined at the electrode tip but extends along its sides as well. This facilitates lesion progression sideways and results in a wider lesion. Of course the lesion is deeper when the electrode is pushed further inside the tissue.

6.8 Discussion on the Simulations Results

The modeling effort described above dealt with the identification of the relative influence of various parameters during RF ablation. A summary of the main findings is given here.

First of all, it has been clearly demonstrated that the RF ablation technique is superior to hot-tip ablation in terms of the lesion size it can produce. Fig. 6.6 (p. 93) shows that with a 2 mm electrode heated to +63°C, the tissue temperature is lower than with RF ablation with only a 1.25 mm electrode. The difference is significant as shown in the figure and justifies the extra effort of using RF ablation. It must be kept in mind however that the temperature distribution presented is the optimum achievable with RF ablation. In practice, it might not be easy to reach that point. On the contrary, with hot-tip ablation no optimization is necessary, apart from the temperature control of the electrode. Nonetheless, the evidence strongly supports RF ablation as a superior technique.

The modeling results reveal that in general the lesion progresses as long as power is applied, up to durations of 120 s. Of course the growing rate has a tendency to decrease with time (except with constant voltage). This means that in the model considered, the steady-state distribution is reached after a period longer than 120 s. One of the reasons for this is the temperature dependence of σ. As tissue heats up, the SAR distribution changes which forces the temperature distribution to change accordingly. Notice that in the case of hot-tip ablation, the steady-state temperature distribution is reached much faster.

It is worth noticing that in all cases where the largest lesion is sought (MTT is maintained constant), the applied voltage functions were similar. That is, the voltage is high for the first

5 s, decreases by 25% at 5 s, and then gradually to -40% at 60 s. It is quite interesting that this is almost constant in all cases. This finding may represent a certain interest in practice.

Another general observation is that the electrode temperature is significantly lower than the maximum tissue temperature (see for instance Fig. 6.10, p. 99). The reason for this is the blood flow which has been shown to have an important cooling effect (Fig. 5.4, p. 77). It follows from this that the electrode temperature is not a good indication of the MTT unless some kind of correction is used. On the other hand, the electrode resistance is closely related to the MTT but not to the lesion size. This finding may be of interest in practice.

The geometry of the electrode used for RF ablation is one of the sigaificant parameters that can be selected by the operator. Specifically, the effect of the length, the radius and the shape of the electrode have been studied and the results are summarized here.

The use of an electrode with a larger radius is an effective way of enlarging the lesion. The improvement comes mainly from the SAR distribution which becomes less abrupt when the radius is larger. Going from r = 1.0 mm to r = 1.5 mm can increase the lesion after 60 s by 60% (Fig. 6.7, 95). Moreover, the advantage of using a larger radius is visible right at the onset of heating and for the whole period. Using a flat-tip electrode instead of one with a hemispherical tip produces the same type of result. The SAR distribution results in a significantly larger lesion. This finding is of importance because it is not always possible to enlarge the electrode radius.

Increasing the electrode length enlarges the lesion in a different way. For short duration of power application, no real difference is visible because the distribution of the SAR is not changed much (apart from a multiplicative factor). However, the lesion with a longer electrode grows at a faster rate. This is due to the increase in the convective loss. Consequently, no benefit can be obtained by using a longer electrode over a short period. Significant benefit is obtained if the application lasts long. This is quite different from the case where the electrode radius is enlarged. The modeling results show that after 60 s, increasing the length from 4 to 10 mm produces a larger lesion than increasing the radius from 1.25 to 1.5 mm (compare the figures in p. 95 and p. 98). The increase in power requirement is important due to the reduced resistance and reduced SAR of longer electrodes.

The investigation of the effect of a suboptimal MTT reveals a strong influence of this parameter on the lesion size. In the case of interest, the lesion turned out to be 50% smaller

when the MTT is reduced from +63 to +43°C (p. 107). All that is produced with an applied voltage that is between 83 and 90% of the optimum voltage, depending on the time. It shows that the voltage must not vary much from its optimum value in order to produce a large difference in the lesion.

The study of constant voltage excitation reveals interesting results (p. 104). Over the whole duration of heating the lesion progresses linearly, with a rate proportional to the applied voltage. At high voltage, the growing rate is high but the power must be interrupted early to avoid overheating. The achievable lesion turns out to be smaller than for a lower voltage which can be applied for a longer period of time. The results also show that a small difference in the voltage leads to a large difference in the size of the achievable lesion and the time to produce it. If the time of application is limited, the highest voltage which does not exceed the MTT limit should be used. Yet, the lesion achievable with a constant voltage are 20% smaller than the optimum lesion achievable over the same period.

The depth of the electrode turns out to be a determinant factor in the lesion size (see Fig. 6.15, p. 109). Unfortunately, this is not a parameter that can be controlled in practice. In the simulations performed here, its effect on the lesion are larger than the effects of the other parameters considered. On the other hand, the variation in the depth should not affect the nature of the conclusions reached about the effect of the other factors. Only their relative magnitude may be altered.

The shape of the lesion is apparently not something over which much control can be exerted. At early times, the various electrode geometries produce slightly different width to depth ratios, varying roughly between 1.5 and 1.7. As time progresses, these diminishes to about 1.35 and 1.5. Obviously the geometry of the model and the thermal transfer phenomena dictate this behavior. Similarly, the lesion sharpness decreases with time (Fig. 6.2, p.88), but there does not seem to be any ways of avoiding this.

The simulations carried out in this chapter provide a new insight into the mechanisms of RF ablation. The extension of these results to real life ablation is discussed next.

6.9 Recommendations for RF Ablation

It makes no doubt that the results obtained in this study must be extended with care to the real-life. In order to be tractable, a number of simplifications had to be included in the

model. In view of the complexity of the matter and the number of factors coming into play, the significance of all results must be confirmed experimentally. Yet, the simulation results can advantageously be used to orient the experimental work. Indeed, it is much easier do carry out experiments when one knows exactly what to look for. The expertise and resources necessary for experimental work of this nature is unfortunately not available for the time being. In the mean time, we offer here a few comments based on the results of the theoretical analysis which may maximize the lesions.

- The catheter electrode should be as long as possible, and as big as the application allows. The level of the applied voltage must be adjusted accordingly;
- An electrode with a flat tip is superior to an electrode with a spherical tip;
- The power should be applied as long as possible since the lesion grows continuously;
- Modulating the voltage can produce considerably larger lesions. The preferred approach is to apply a relatively high voltage (and power) at the onset and decrease it gradually during ablation;
- A correction must be applied to the electrode temperature in order to evaluate the tissue temperature;
- The electrode temperature alone is not a good indicator of lesion size;
- With modulated voltage, the electrode resistance must not be used as an indication of the lesion size but as an indication of the tissue temperature;
- With the application of a constant voltage, the electrode resistance should vary continuously indicating tissue heating and lesion progression;

Some aspects of the problem which turn out to have a considerable importance on the lesion size will always remain more or less uncontrollable: the depth of the electrode inside the tissue, the variability of the tissue properties, the instability of the contact. One has to accept these inherent limitations of the technique. On the other hand, some issues brought up in this study may prove to have a practical significance that has been neglected in the past. It is the case for the electrode geometry which undoubtedly affects the lesion size. It is also the case for the electrical excitation and the electrode resistance.

In practice, the electrode resistance has two components: the resistance of the heart and lung tissues which has been calculated in this study, and an additional contribution from the fat and skin layers which is not known. Obviously, these act as a voltage (and power) divider between the two electrodes. The effective voltage appearing across the heart layer (the one considered in this study) is therefore only a portion of the total applied voltage. It is possible, by making a few resistance measurements before ablation is performed, that the fat component could be quantified. This information, in conjunction with the simulation results, would help in the evaluation of the magnitude of the voltage to be applied. Furthermore, since the optimum voltage modulation is practically always the same in all cases studied here, this modulation could be used with a potential improvement of the outcome.

Chapter 7

Conclusion

7.1 Summary of the Research

In this research a theoretical approach is used to investigate the RF ablation technique. There are a few reasons for this. The first one is the absence of reliable theoretical results to support the experimental observations reported in the literature. Another reason is that a theoretical approach provides a more thorough understanding because it permits to study individually the effects of various parameters. Finally, an experimental research necessitates medical expertise and equipment that is considerably more important than what is readily available.

The model of ablation is axisymmetric and consists of an electrode coming in contact at right angle with a slab of homogeneous heart tissue. The blood flow around the electrode is also considered. The most appropriate values for the physical properties in the model are determined after a review of the literature on that subject. The thermal lesion is calculated with an expression developed to predict the extent of human skin burns and is based on the phenomenon of protein denaturation. A numerical simulator based on the method of finite-elements is developed to solve the differential equations governing the physical processes of interest. The complexity of the simulations (time-dependence, non-linearity, coupling of electrical and thermal problems) is such that no analytical methods is available to validate the software in a convincing way is available. Because the whole research relies on the modeling software, an experimental proof of its validity is sought.

The experiment consists in comparing the predicted and measured electrode resistances and temperature distributions produced by RF ablation on a tissue-equivalent material.

Tissue-equivalent material, developed during this work, is used because of the repeatability of its properties. A thermographic camera is used for temperature measurements. Continuous, modulated and pulsed electrical excitations are considered. In all cases a good agreement is obtained which confirms the applicability of the software to the study of RF ablation.

Preliminary calculations are performed with the simulator in order to assess the significance of a number of factors. These calculations lead to the identification of the blood flow and the temperature dependence of the conductivity as two significant factors that must be considered in the modeling.

The investigation of RF ablation as such is carried out by calculating the effects of a number of parameters taken in isolation. Among the parameters under study are the electrode geometry and voltage modulation. The time evolution of the lesions are presented. Comparisons with a common control case reveal how increasing the length and the radius of the electrode can produce larger lesions. The results also reveal that the use of a flat-tip electrode is preferable to a spherical tip. The lesions obtained with the optimum voltage modulation are shown to be considerably larger than with a constant voltage.

The objectives of this work have been realized. A numerical model for the calculation of the time-dependence of the lesion produced by RF ablation has been developed. An experiment has been realized to confirm its validity. The software has been used to study the effect of various factors on the final lesion and recommendations have been formulated to improve the existing procedure. The theoretical results of this thesis are the first to be published and can certainly help the investigators of the RF ablation technique who rely on an experimental approach.

7.2 Future Work

It is the author's opinion that the lesions currently produced clinically by RF ablation are not maximized. A thorough experimental research should be undertaken in order to assess the full potential of the technique. In light of the results presented here, those studies could be more focused and effective than those presented so far in the literature. However one must realize that experimental research of this nature involves many people, is complicated to set-up and is costly. It is not clear whether the potential benefit of better controlling the procedure outweighs the cost of the research.

The author does not think that further theoretical work on the lesion formation process itself is justified. The major aspects of the procedure are fairly well known now. The uncontrollable factors naturally occurring during ablation seem too numerous and important to justify more in-depth analyses.

New methods of catheter ablation of the myocardium using microwave energy have been suggested recently. A lot of issues on this topic remain to be clarified: can it really be superior to RF? Is it at all feasible with the existing technology? What type of antenna should be used? These can constitute interesting avenues for further research.

Appendix A

Quasi-Static Approximation for the Electric Field

The following presents a justification for the use of Equation (3.2) to obtain the voltage distribution. Interesting discussions about the quasi-static approximation can be found in [95, p.455],[96, p.225],[97].

The solutions for electromagnetic fields comprise a phase delay term of the form

$$e^{-jkR} = 1 - jkR - \frac{(kR)^2}{2} - \frac{j(kR)^3}{3} \ldots$$

which describes the retarded nature of the harmonic fields away from the sources. Close to the sources, when $kR << 1$, we have $e^{-jkR} \approx 1$ and no retarded effect is observed. That is, the field solution is everywhere in phase, much like the situation obtained for static fields. This is the quasi-static approximation which transforms Maxwell's equations into:

$$\begin{aligned} \vec{E} &= -\nabla V \\ \nabla \cdot \vec{D} &= \rho \\ \nabla \cdot \vec{J} &= -j\omega\rho \end{aligned}$$

where the conventional notation has been used for the variables. Using the constitutive relations we get

$$\nabla \cdot \left(\epsilon + \frac{\sigma}{j\omega}\right) \nabla V = 0. \qquad \text{(A.1)}$$

In our application, it is required to compute the power dissipated in the tissue by the electrical current. Due to the geometry, most of it is deposited very close (< 1 cm) to the catheter

electrode. Using published data for the heart's electrical properties at 1 MHz (Chapter 3) we have: $\epsilon' = 2 \cdot 10^3$, $\epsilon'' = \sigma/\omega\epsilon_0 = 1.1 \cdot 10^4$, $k^2 = \omega^2\mu_0\epsilon_0(\epsilon' - j\epsilon'')$, and

$$k = 2.2 \angle -39.8^\circ.$$

With $R = 10^{-2}$ m, we get $kR << 1$ and the quasi-static approximation is justified. Furthermore for heart tissue we have

$$\epsilon'' > 5\epsilon'.$$

We assume that ϵ' is negligible with respect to ϵ'' and we can use the approximation

$$\nabla \cdot \sigma \nabla V = 0$$

instead of (A.1).

Appendix B

Evaluation of the Heat Transfer Coefficient at Blood Interfaces

This appendix derives the value of h at the interfaces where blood is flowing (electrode and heart). For simplicity, it is assumed that the prevailing conditions are those of laminar flow over a flat plate. As the situation in the heart is much more complex than that, this yields only a first order approximation.

When a fluid is moving over a solid at a different temperature, a transfer of heat occurs between the two (convective heat transfer). The rate of heat transfer per unit area from the solid to the fluid has been observed experimentally to obey

$$q = h\,(T_{\text{solid}} - T_{\text{fluid}})$$

where h (W $\text{m}^{-2}\,^{\circ}\text{C}^{-1}$) is the heat transfer coefficient which depends on the interface, the flow regime, the fluid viscosity and various other factors. Many authors treat the problem of heat convection and develop mathematical expressions to evaluate h for idealized cases [98, 99]. Our particular problem is to quantify h around the catheter electrode. This is a very complex problem because of its geometry and because the blood flow is complex and pulsatile. Moreover, all conditions depend on the particular location in the heart where the ablation takes place. It is therefore not possible to evaluate h with any precision in this case. Instead, it was decided to compute the order of magnitude of h. For that, we used the approximation for a steady, laminar flow over a flat plate. This certainly constitutes a lower bound for the heat transfer coefficient in our application.

The plate is assumed to be held at a constant temperature. As the fluid progresses, its temperature tends to equilibrate with that of the plate. Beyond a certain distance down the

plate surface, the temperature distribution in the fluid remains constant. Writing the energy balance equation for an elemental control volume inside the fluid, we obtain a differential equation for the fluid's temperature. The spatial derivative of the temperature at the solid liquid interface is then used to evaluate a *local transfer coefficient* h_x at a particular position x on the plate. An average transfer coefficient over the whole plate can also be calculated. It is given by

$$h = 0.664 \, \mathrm{Pr}^{1/3} \, \mathrm{Re}^{1/2} \, \frac{k}{L}$$

where

$$\begin{aligned} \mathrm{Pr} &= \text{Prandtl number} &&= c_p \mu / k, \\ \mathrm{Re} &= \text{Reynolds number} &&= L v \rho / \mu. \end{aligned}$$

In the above, the symbols used are

c_p = specific heat (J kg^{-1} $^\circ\mathrm{C}^{-1}$),

μ = absolute or dynamic viscosity (kg m^{-1} s^{-1}),

k = thermal conductivity (W m^{-1} $^\circ\mathrm{C}^{-1}$),

L = length of plate (m),

v = velocity of the fluid outside the boundary layer (m s^{-1}),

ρ = density (kg m^{-3}).

In our case the following values are used:

- $c_p = 4180$ J kg^{-1} $^\circ\mathrm{C}^{-1}$, the value for water,
- $\mu = 2.319 \cdot 10^{-3}$ kg m^{-1} s^{-1}, [5, p.111]
- $k = 0.55$ W m^{-1} $^\circ\mathrm{C}^{-1}$, Table 3.2 p. 36,
- $L = 10^{-2}$ m, representative of the lesion diameter,
- $v = 0.1$ m s^{-1}, conservative value for blood velocity in heart,
- $\rho = 1000$ kg m^{-3}, value for water.

The value calculated for h is thus:

$$h \approx 2000 \text{ W } \mathrm{m}^{-2} \, ^\circ\mathrm{C}^{-1}.$$

As mentioned above, this constitutes a lower bound estimate. The small size of the area of interest is the reason why h is large.

Appendix C

Time-Dependent FEM Formulation

This appendix develops the system of equations that must be solved to obtain an approximate solution ϕ' to partial differential equation (3.7) which is repeated here:

$$F(\phi) = P\nabla^2\phi + Q\frac{\partial\phi}{\partial t} + \psi = 0. \qquad (C.1)$$

Depending on the values of P, Q, ϕ and ψ, this general differential equation is used to calculate the electrical potential V or the temperature T. For the electrical problem,

$$\begin{aligned} \phi &= V \ (\mathrm{V}) \\ P &= \sigma \ (\mathrm{S\ m^{-1}}) \\ Q &= 0 \\ \psi &= 0 \end{aligned}$$

and for the thermal problem,

$$\begin{aligned} \phi &= T \ (^\circ\mathrm{C}) \\ P &= k \ (\mathrm{W\ m^{-1}\ ^\circ C^{-1}}) \\ Q &= -\rho c_p \ (\mathrm{kg\ m^{-3}})(\mathrm{J\ kg^{-1}\ ^\circ C^{-1}}) \\ \psi &= \text{heat source} \ (\mathrm{W\ m^{-3}}). \end{aligned}$$

The spatial operator is treated with the FEM and a time-stepping scheme using the FDM approximation resolves the time dependence. It will be assumed here that ϕ' and ψ

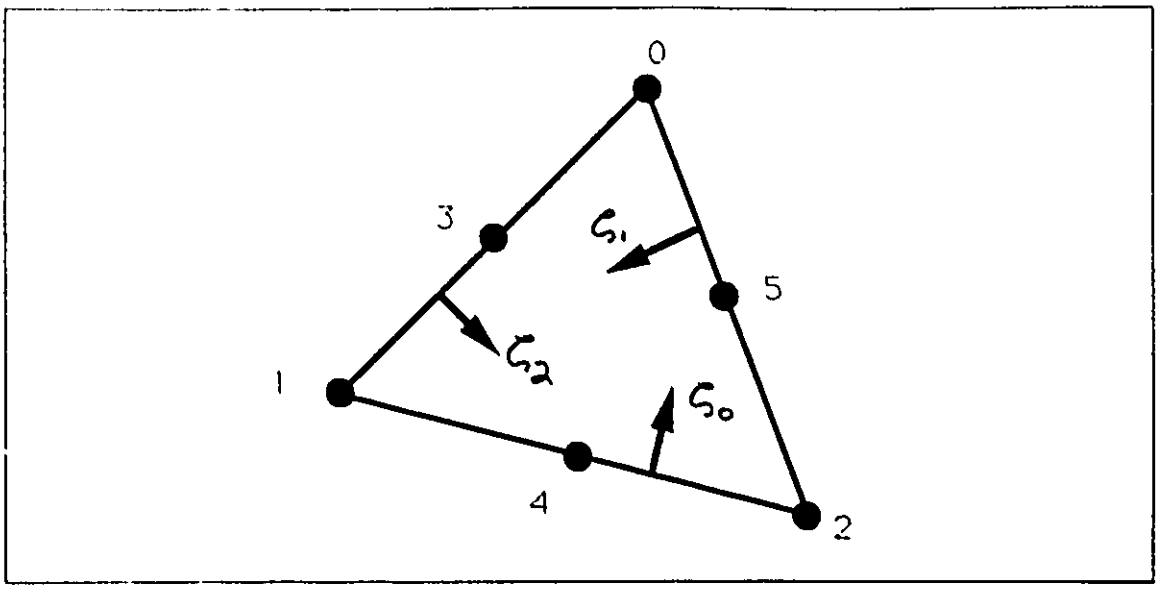

Figure C.1: Drawing of a generic 6 node triangle e with node numbering and local coordinates. See [101].

vary with time but that all other quantities including the boundary conditions are fixed. For the thermal problem, this corresponds to computing the time variable temperature of a fixed medium heated with a time variable heat source. The details of the C programs are in [100]. The development presented here in mathematical language has been briefly summarized in plain words in Chapter 3.

In this research, (C.1) has been solved in cylindrical coordinates (r, θ, z) assuming axial symmetry $\partial/\partial\theta = 0$ so that the domain of interest is the half-plane $-\infty < z < \infty, r > 0$. The domain is divided into a mesh of second order (6 nodes) triangular elements as described in [101, Chap. 4]. Notice however that the node numbering scheme used there differs from this one. The first section gives a detailed description of the second order triangular elements, their local coordinate system, and the basis functions defined over them. In the following section, the development of the system of linear equations for (C.1) is carried out. It contains three generic matrices whose computation are done in the last section.

C.1 Second Order Triangles

Figure C.1 shows a generic second order triangular element ϵ with the local node numbering

and the local coordinates $(\zeta_0, \zeta_1, \zeta_2)$[1] which assume values $0 \leq \cdot \leq 1$. For a point (r, z) inside the triangle, the local coordinates are obtained by:

$$\zeta_i = \frac{1}{2A_e}(a_i + b_i r + c_i z) \qquad i = 0, 1, 2 \tag{C.2}$$

with

$$\begin{aligned} a_i &= r_{i+1}z_{i+2} - r_{i+2}z_{i+1} \\ b_i &= z_{i+1} - z_{i+2} \\ c_i &= r_{i+2} - r_{i+1} \\ A_e &= \text{area of triangle.} \end{aligned} \tag{C.3}$$

The indices must be understood as progressing $0, 1, 2, 0, 1$. The basis functions associated to the nodes are the same second order polynomials as used in [101] and are defined by:

$$\begin{aligned} \alpha_0(r, z) &= 2\zeta_0^2 - \zeta_0 \\ \alpha_1(r, z) &= 2\zeta_1^2 - \zeta_1 \\ \alpha_2(r, z) &= 2\zeta_2^2 - \zeta_2 \\ \alpha_3(r, z) &= 4\zeta_0\zeta_1 \\ \alpha_4(r, z) &= 4\zeta_1\zeta_2 \\ \alpha_5(r, z) &= 4\zeta_0\zeta_2. \end{aligned} \tag{C.4}$$

For clarity, the (r, z) dependence of the basis functions will not be explicitly shown. Each α_i has local support on the triangle, is equal to 1 at its associated node and to 0 at every other nodes. The α_i's are therefore independent. Figure C.2 shows plots of some of the basis functions on two adjacent triangles. This choice of α_i's satisfies the inter-element continuity requirement for ϕ' because the 3 nodes on each edge of a triangle guarantee that only one second order polynomial can describe ϕ' on that edge [101, p.108]. However, the first derivatives of the basis functions are not continuous between elements[2]. It can also be shown that:

$$-2A_e \cot\theta_i = (b_{i+1}b_{i+2} + c_{i+1}c_{i+2}), \tag{C.5}$$

[1] Node numbering starts at 0 instead of 1 for direct compatibility with arrays defined in C.

[2] This means that the electric field and consequently the SAR calculated in the electric problem is not continuous between elements. This is not a major limitation, as far as the thermal problem is concerned, if the triangles are small enough. See also Section C.4.

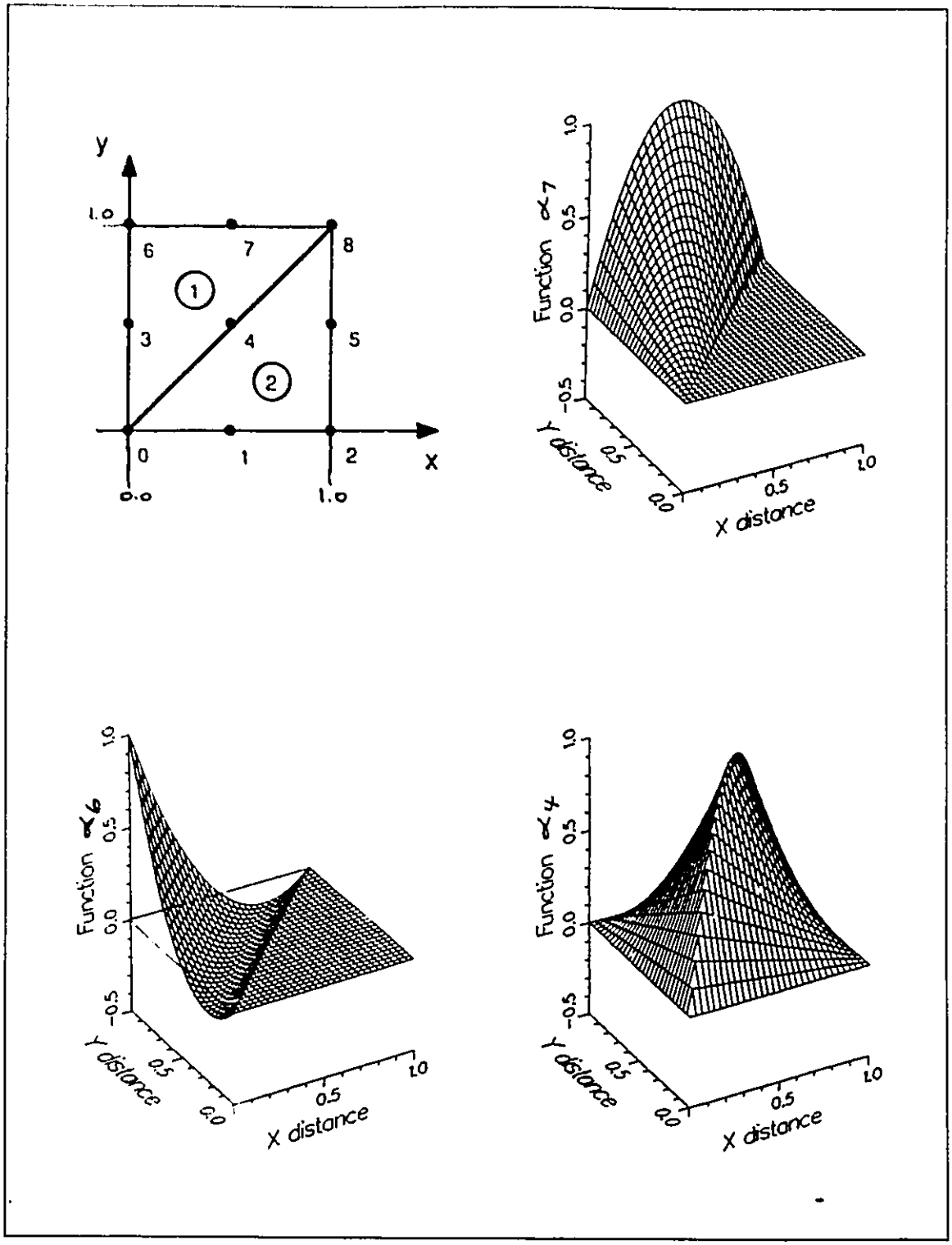

Figure C.2: Some of the second order polynomial basis functions α_i's used for the expansion of ϕ'.

$$2A_e\left(\cot\theta_{i+1}+\cot\theta_{i+2}\right) \;=\; \left(b_i^2+c_i^2\right),$$

and that,

$$r=\sum_{v=0}^{2} r_v\zeta_v, \tag{C.6}$$

$$\iint_e \zeta_0^m\,\zeta_1^n\,\zeta_2^p\,dr\,dz = 2A_e\frac{m!\,n!\,p!}{(m+n+p+2)!}, \tag{C.7}$$

where θ_i is the internal angle at vertex i and the index v denotes the triangle vertices (local nodes 0,1,2).

C.2 Development

Let us take over from where we left in Chapter 3 by rewriting Eq. (3.7):

$$P\oint_S \beta_q\nabla\phi'\cdot d\vec{S} - P\int_V \nabla\beta_q\cdot\nabla\phi'\,dV + \int_V Q\beta_q\frac{\partial\phi'}{\partial t}+\psi\beta_q\,dV = 0. \tag{C.8}$$

With the assumption of axial symmetry, ϕ' and ψ refer respectively to $\phi'(r,z,t)$ and $\psi(r,z,t)$. Let us recall here that ψ corresponds to a source term and is a known function. Volume integrals are replaced by surface integrals in the (r,z) plane as follows:

$$\begin{aligned}\int_V f(r,z)\,dV &= \int_V f(r,z)\,r\,dr\,d\theta\,dz\\ &= 2\pi\iint f(r,z)\,r\,dr\,dz.\end{aligned} \tag{C.9}$$

Similarly, closed surface integrals become line integrals in the (r,z) plane:

$$\begin{aligned}\oint_S \vec{g}(r,z)\cdot d\vec{S} &= \oint_S \vec{g}(r,z)\cdot\hat{n}\,r\,d\theta\,dl\\ &= 2\pi\oint_c \vec{g}(r,z)\cdot\hat{n}\,r\,dl\end{aligned} \tag{C.10}$$

where c is the contour in the (r,z) plane, $\hat{n}$ is a unit outward vector normal to c and dl is measured along c. Rewriting (C.8) with (C.9) and (C.10) we get:

$$\begin{aligned}2\pi P\oint \beta_q\nabla\phi'\cdot\hat{n}\,r\,dl &- \\ 2\pi P\iint \nabla\beta_q\cdot\nabla\phi'\,r\,dr\,dz &+ \\ 2\pi\iint\left(Q\beta_q\frac{\partial\phi'}{\partial t}+\psi\beta_q\right)r\,dr\,dz &= 0.\end{aligned} \tag{C.11}$$

Let the domain in the (r,z) plane be divided into a triangular mesh with NN nodes and NTR triangles. Let us expand ϕ' as follows:

$$\phi' = \sum_{i=0}^{NN-1} u_i(t)\,\alpha_i(r,z) \tag{C.12}$$

where the only unknowns are the $u_i(t)$'s. For clarity again, the explicit time dependence of u_i's will not be shown. Next apply (C.12) to (C.11), drop the 2π, use the Galerkin method ($\beta_q = \alpha_q$) and decompose the integrals into summations over every triangle[3]. Equation (C.11) becomes:

$$\sum_{e=0}^{NTR-1} \left\{ P_e \oint_e \alpha_q \nabla\phi' \cdot \hat{n}\, r\, dl - P_e \iint_e \nabla\alpha_q \cdot \nabla \left(\sum_{i=0}^{NN-1} u_i\alpha_i \right) r\, dr\, dz + \right. \tag{C.13}$$

$$\left. Q_e \iint_e \alpha_q \frac{\partial}{\partial t} \left(\sum_{i=0}^{NN-1} u_i\alpha_i \right) r\, dr\, dz + \iint_e \alpha_q \psi_e\, r\, dr\, dz \right\} = 0 \qquad q = 0, NN-1.$$

By using $q = 0, NN-1$, a total of NN equations are obtained and the system can be solved. From now on subscript $_e$ refers to triangle e.

A very significant simplification is possible if one uses the local support property of the α_i's. In fact, the integrals over triangle e vanish if α_q and α_i are not associated to the nodes of e. Consequently the $\sum_{i=0}^{NN-1}$ can be replaced by $\sum_{i=0}^{5}$ where i refers to the local nodes of e. Similarly, q needs only assume values from 0 to 5 again referring to the local nodes. With this observation, the NTR triangles can be considered independently, and their contributions properly assembled as rows and columns of the final system of equations in a sequential manner. Furthermore, over a single triangle, ψ_e can be expanded as (see Section C.4):

$$\psi_e = \sum_{i=0}^{5} w_{ei}(t)\,\alpha_i(r,z) \tag{C.14}$$

where as mentioned above the w_{ei}'s are known. From now on, the contribution to (C.13) of a single **generic triangle** will be considered. The expressions will be written as equations but it must be understood that the equality holds only when the contributions of all triangles are summed. The sign $\doteq$ will be used to remind this important fact.

[3]The contour integral poses a problem because the gradient of ϕ' is not continuous between triangles as it is the case for the exact solution ϕ. However, let us simply assume that it is continuous, so that the contributions from adjacent triangles cancel each other. This is equivalent to ignoring this integral except on the boundary of V.

Simple manipulations of the left-hand side of (C.13) and the use of (C.6) to replace r yield

$$P_e B_q + \sum_{i=0}^{5} \left(-P_e S_{qi} u_i + Q_e T_{qi} \frac{du_i}{dt} + T_{qi} w_{ei} \right) \doteq 0 \qquad q = 0,5 \tag{C.15}$$

where

$$\begin{aligned} \sum_{v=0}^{2} r_v \oint_e \zeta_v \alpha_q \nabla \phi' \cdot \hat{n}\, dl &= B_q \\ \sum_{v=0}^{2} r_v \iint_e \zeta_v \nabla \alpha_q \cdot \nabla \alpha_i \, dr\, dz &= S_{qi} \\ \sum_{v=0}^{2} r_v \iint_e \zeta_v \alpha_q \alpha_i \, dr\, dz &= T_{qi}. \end{aligned} \tag{C.16}$$

For every triangle, (C.15) is a system of 6 ODE's in u_i's. To eliminate the time derivative and transform it into a set of algebraic equations, discretize time as follows [102, 103]:

$$t = n\Delta t \qquad n = 0, 1, \ldots$$

All time variable quantities $X(t)$ become $X(n)$ at $t = n\Delta t$ denoted $X^{(n)}$. Let us next use the variable-weighted implicit formulation to locate the spatial operator of (C.15) at $t = (n+\tau)\Delta t$, $0 \le \tau \le 1$. The time dependent quantities are linearly approximated as:

$$X^{(n+\tau)} \approx (1-\tau) X^{(n)} + \tau X^{(n+1)} \tag{C.17}$$

and the time derivative calculated by

$$\frac{dX^{(n+\tau)}}{dt} \approx \frac{X^{(n+1)} - X^{(n)}}{\Delta t}. \tag{C.18}$$

When τ is 0 and 1, (C.17) results respectively in the backward difference and the forward difference approximations[4]. Using the time approximations in (C.15) yields:

$$\begin{aligned} P_e B_q + \sum_{i=0}^{5} \Bigg\{ & - P_e S_{qi} \left((1-\tau) u_i^{(n)} + \tau u_i^{(n+1)} \right) + \\ & Q_e T_{qi} \left(\frac{u_i^{(n+1)} - u_i^{(n)}}{\Delta t} \right) + T_{qi} \left((1-\tau) w_{ei}^{(n)} + \tau w_{ei}^{(n+1)} \right) \Bigg\} \doteq 0 \qquad q = 0,5 \end{aligned} \tag{C.19}$$

[4]It can be shown that the best accuracy is obtained when $\tau = 0.5$ (Crank-Nicolson scheme). For linear approximation over triangular elements, the Crank-Nicolson scheme is stable for any time step Δt chosen, although for large Δt there may be unrealistic, decreasing oscillations in the calculated time response (see [104]). In this study, time step is decreased to confirm that the solution is not oscillatory. For more on oscillations see [102].

which after rearrangement leads to

$$P_e B_q + \sum_{i=0}^{5} \left\{ \left(\frac{Q_e}{\Delta t} T_{qi} - \tau P_e S_{qi} \right) u_i^{(n+1)} + \right. \tag{C.20}$$
$$\left. \left((\tau - 1) P_e S_{qi} - \frac{Q_e}{\Delta t} T_{qi} \right) u_i^{(n)} + T_{qi} \left((1 - \tau) w_{ei}^{(n)} + \tau w_{ei}^{(n+1)} \right) \right\} \doteq 0 \qquad q = 0, 5.$$

Let us recall here that this final expression represents the contribution of a generic triangle to Equation (C.13) and that $\doteq$ denotes equality when all contributions are added. The indices q and i run from 0 to 5 and refer to the local node numbers. This set of algebraic expressions contributes 6 unknowns and 6 equations to the final system. The unknowns are the u_i's evaluated at time step $(n + 1)$.

A difficulty arises concerning the terms in w_e's which represent the heat source for thermal problems. Indeed, the equation reveals that in order to calculate the temperature at the coming time step ($u_i^{(n+1)}$), one must have a knowledge of the source at that time ($w_{ei}^{(n+1)}$). But the distribution of the heat source depends on the voltage distribution, and hence on the temperature itself because of the temperature dependence of the conductivity. To resolve the situation the treatment of the heat source is done as follows. The electrical power distributed by a unit source, $w_{ei}^{(n)}$ is calculated at a given time step, once the temperature for that time is known. The voltage modulation is considered by multiplying the unit power distribution by a scalar modulation parameter, $\mathrm{mod}^{(n)}$, which numerically is equal to the square of the voltage value. Moreover, the unit power distribution at the coming time step is assumed equal to that at the current time step $w_{ei}^{(n)} = w_{ei}^{(n+1)}$. Clearly, this approach is justified only when the time step is small.

With this treatment of the source terms, and using the notation $\langle \cdot \rangle$ for a matrix and $\langle \cdot$ for a column vector the triangle contribution becomes:

$$P_e \langle \mathrm{B} + \left\{ \frac{Q_e}{\Delta t} \langle \mathrm{T} \rangle - \tau P_e \langle \mathrm{S} \rangle \right\} \langle \mathrm{u}^{(n+1)} \doteq \tag{C.21}$$
$$\left\{ (1 - \tau) P_e \langle \mathrm{S} \rangle + \frac{Q_e}{\Delta t} \langle \mathrm{T} \rangle \right\} \langle \mathrm{u}^{(n)} - \langle \mathrm{T} \rangle \left\{ (1 - \tau) \, \mathrm{mod}^{(n)} + \tau \, \mathrm{mod}^{(n+1)} \right\} \langle \mathrm{w_e}^{(n)}$$

It now remains to develop the generic matrices $\langle \mathrm{S} \rangle$, $\langle \mathrm{T} \rangle$, $\langle \mathrm{B}$.

C.3 Generic Matrices

It turns out that the generic matrices can be obtained from simpler element-independent matrices that can be computed once and for all.

Generic Matrix ⟨S⟩

Equation (C.16) gives

$$S_{qi} = \sum_{v=0}^{2} r_v \iint_e \zeta_v \nabla a_q \cdot \nabla a_i \, dr\, dz. \tag{C.22}$$

Because axial symmetry is assumed, we have

$$\nabla = \hat{a}_r \frac{\partial}{\partial r} + \hat{a}_z \frac{\partial}{\partial z}. \tag{C.23}$$

By the chain rule,

$$\frac{\partial a_x}{\partial r} = \sum_{j=0}^{2} \frac{\partial a_x}{\partial \zeta_j} \frac{\partial \zeta_j}{\partial r}, \tag{C.24}$$

and similarly for $\partial a_x/\partial z$. Using (C.23), (C.24) and (C.2) and combining terms (C.22) becomes

$$S_{qi} = \sum_{v=0}^{2} r_v \iint \frac{\zeta_v}{4A_e^2} \sum_{j=0}^{2} \sum_{k=0}^{2} \frac{\partial a_q}{\partial \zeta_j} \frac{\partial a_i}{\partial \zeta_k} (b_j b_k + c_j c_k) \, dr\, dz. \tag{C.25}$$

Using (C.5) to develop the expression under the double summation we can replace these by a single one and obtain:

$$S_{qi} = \sum_{v=0}^{2} r_v \sum_{k=0}^{2} Q_{qi}^{vk} \cot\theta_k \tag{C.26}$$

where

$$Q_{qi}^{vk} = \frac{1}{2A_e} \iint_e \zeta_v \left(\frac{\partial a_q}{\partial \zeta_{k+1}} - \frac{\partial a_q}{\partial \zeta_{k-1}} \right) \left(\frac{\partial a_i}{\partial \zeta_{k+1}} - \frac{\partial a_i}{\partial \zeta_{k-1}} \right) dr\, dz \tag{C.27}$$

The Q_{qi}^{vk}'s do not depend on absolute triangle coordinates and can be computed once for all. Furthermore, using clever row and column permutations [105], it turns out that all Q_{qi}^{vk}'s can be generated from Q_{qi}^{00} and Q_{qi}^{10} so that only these two need to be stored. Further details are given in [100].

Generic Matrix ⟨T⟩

From equation (C.16):

$$T_{qi} = 2A_e \sum_{v=0}^{2} r_v R_{qi}^{v}$$

where

$$R^v_{qi} = \frac{1}{2A_e} \iint_e \zeta_v a_q a_i \, dr \, dz.$$

the R^v_{qi} do not depend on absolute triangle coordinates and can be calculated once and for all. Again, R^1_{qi} and R^2_{qi} can be obtained by applying row and column permutations to R^0_{qi} so that only this one needs to be stored [105]. Details are given in [100].

Generic Matrix $\langle B$

From (C.16) we have:

$$B_q = \sum_{v=0}^{2} r_v \oint_e \zeta_v a_q \nabla \phi' \cdot \hat{n} \, dl$$

where $\oint_e dl$ represents integration over the perimeter of triangle e and $\hat{n}$ is a unit outward normal vector. Considering the assumed continuity of $\nabla \phi'$, it is easily seen that the contribution to B_q of all the triangles cancel except for those triangles that have an edge lying on an external boundary. It follows that B_q need only be calculated for those triangles. Assuming that at most one side of each triangle lies on a boundary, the contribution becomes:

$$B^k_q = \sum_{v=0}^{2} r_v \int_k^{k+1} \zeta_v a_q \nabla \phi' \cdot \hat{n} \, dl \qquad \text{(C.28)}$$

where nodes k and $k+1$ ($k = 0, 1, 2, 0$) identify the edge on the boundary. It now remains to develop B^k_q for Dirichlet, Neumann and convective boundaries. Figure C.3 shows a generic triangle e with one edge on a boundary and the node identification used in the following developments.

Dirichlet boundary condition: In this case, ϕ' is known at nodes $k, j, k+1$. Therefore, the system has no lines corresponding to $q = k, j, k+1$. We have:

$$B^k_q = \begin{pmatrix} \cdot \\ \cdot \\ B^k_{k+2} \\ \cdot \\ B^k_{j+1} \\ B^k_{j+2} \end{pmatrix}.$$

But on edge $k, k+1$, the basis functions a_{k+2}, a_{j+1} and a_{j+2} all equal 0 so all B^k_q's vanish. Notice that u_i is defined on Dirichlet nodes and $\langle \mathbf{u}^{(n)}$ must contain these values for the right-hand side of (C.21) to be evaluated properly.

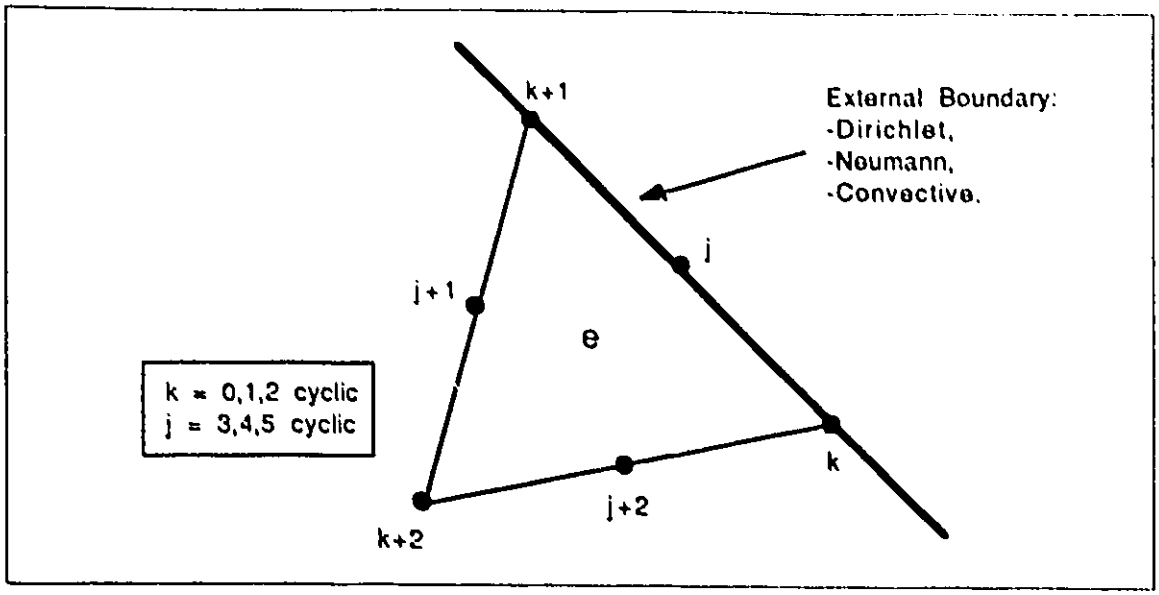

Figure C.3: Generic triangle e with one edge sitting on a boundary.

Neumann boundary condition: For this case, $\nabla\phi' \cdot \hat{n} = C_k$ on edge $k, k+1$ where C_k is a known constant. All 6 nodes of triangle e are unknown, so that the final system of equations contains a line and a column for each of them. Equation (C.28) becomes:

$$B_q^k = \sum_{v=0}^{2} r_v C_k \int_k^{k+1} \zeta_v \alpha_q \, dl = C_k \sum_{v=0}^{2} r_v \int_k^{k+1} \zeta_v \alpha_q \, dl.$$

This expression can be recast as follows for an easier evaluation:

$$B_q^k = C_k d_k L_q^k; \qquad L_q^k = \sum_{v=0}^{2} r_v M_q^{vk},$$

with:

$$M_q^{vk} = \frac{1}{d_k} \int_k^{k+1} \zeta_v \alpha_q \, dl.$$

The M_q^{vk}'s are independent of the triangle shapes and can be computed once and for all. Moreover, they can all be obtained from M_q^{00} and M_q^{01} by proper row and line permutations. More details can be found in [100]. In the above d_k represents the absolute distance between nodes k and $k+1$.

Convective boundary condition: This type of boundary is encountered in thermal problems. The situation they represent is that of the interface between a solid and a flowing fluid

with a constant temperature. It has been found experimentally that in such a case, the gradient of the temperature at the surface is proportional to the temperature at the surface itself. In mathematical terms we have:

$$\nabla T \cdot \hat{n} = \frac{h}{k}(T_0 - T),$$

where T is the unknown temperature at the surface of the solid, T_0 is the known fluid temperature, k is the thermal conductivity of the solid and h is the *heat transfer coefficient* characterizing the particular interfacial conditions (see Appendix B). Using the notation of the general differential equation we have:

$$\nabla \phi' \cdot \hat{n} = C_k(\phi_0 - \phi')$$

where $C_k = h/k$. The expression for B_q^k becomes:

$$B_q^k = \sum_{v=0}^{2} r_v \int_k^{k+1} \zeta_v \alpha_q C_k(\phi_0 - \phi')\, dl.$$

After expansion of ϕ' into its weighted basis functions and using the finite difference approximations at $t = (n + \tau)\Delta t$ we obtain:

$$B_q^k = C_k d_k \phi_0 L_q^k + C_k d_k(\tau - 1)\sum_{i=0}^{5} u_i^{(n)} N_{qi}^k - C_k d_k \tau \sum_{i=0}^{5} u_i^{(n+1)} N_{qi}^k$$

where

$$\begin{aligned} I_{qi}^{vk} &= \frac{1}{d_k}\int_k^{k+1} \zeta_v \alpha_q \alpha_i \, dl \\ M_q^{vk} &= \frac{1}{d_k}\int_k^{k+1} \zeta_v \alpha_q \, dl \\ N_{qi}^k &= \sum_{v=0}^{2} r_v I_{qi}^{vk} \\ L_q^k &= \sum_{v=0}^{2} r_v M_q^{vk}. \end{aligned}$$

Again the I_{qi}^{vk} can be computed once and for all and can all be obtained from I_{qi}^{00} so that only this one must be stored. The contribution to the final system of Equation (C.21) of a triangle with one edge on a convective boundary is thus:

$$-P_e C_k d_k \tau \,(\mathbf{N^k})\,(\mathbf{u}^{(n+1)} \doteq P_e C_k d_k(1 - \tau)\,(\mathbf{N^k})\,(\mathbf{u}^{(n)} - P_e C_k d_k \phi_0\,(\mathbf{L^k}.$$

In this section, the treatment of the boundary conditions has been presented. The finite element program must include the necessary steps to incorporate this information into the final system of equations. This procedure is facilitated by considering a mesh whose triangles contain at most one edge on an external boundary. However, it may happen that a particular node located at the intersection of two portions of the external boundary, assume two different boundary conditions in two adjacent triangles. These situations require a special treatment. More details about the computer implementation in general are given in [100].

C.4 Joule Loss

We want to evaluate the w_{ei} in (C.14). In general, Joule loss (ψ, W m^{-3}) is expressed as

$$\psi(r,z) = \vec{J}\cdot\vec{E} = \sigma\vec{E}\cdot\vec{E} = \sigma|\nabla\phi'|^2. \tag{C.29}$$

The solution domain is subdivided into triangles. Over every triangle, we can associate $\psi_e(\zeta_0,\zeta_1,\zeta_2)$. In this case, ψ_e is continuous in its triangle because ϕ'_e is a second order function of the local coordinates and therefore can be differentiated once. However, since only the continuity of ϕ' and not of $\nabla\phi'$ is guaranteed between adjacent triangles, ψ_e is not continuous there. This is not a major problem if the elements are small enough. Since the ϕ'_e is of second order in the local coordinates, so is ψ_e. Therefore, the value of ψ_e at only 6 points is required to uniquely determine its value over the triangle. Those 6 points can be conveniently chosen as the 3 vertices, and the three middle points of the edges, as before. The expansion (C.14) follows:

$$\psi_e = \sum_{i=0}^{5} w_{ei}(t)\,\alpha_i(r,z). \tag{C.30}$$

Using (C.12) to develop (C.29) we get:

$$\psi_e = \sigma_e \sum_{q=0}^{5} u_q \sum_{j=0}^{5} u_j(\nabla\alpha_q\cdot\nabla\alpha_j).$$

Using the same type of development as for the generic matrices we obtain:

$$\psi_e = \frac{\sigma_e}{2A_e}\sum_{q=0}^{5} u_q \sum_{j=0}^{5} u_j f^e_{qj}(\zeta_0,\zeta_1,\zeta_2)$$

with

$$f^e_{qj} = \sum_{k=0}^{2} \cot\theta_k \left(\frac{\partial\alpha_q}{\partial\zeta_{k+1}} - \frac{\partial\alpha_q}{\partial\zeta_{k-1}}\right)\left(\frac{\partial\alpha_j}{\partial\zeta_{k+1}} - \frac{\partial\alpha_j}{\partial\zeta_{k-1}}\right).$$

The f_{qj}^{ϵ}'s are cast as separate C functions in the program. The $w_{\epsilon i}$'s are calculated by solving ψ_ϵ at the appropriate $(\zeta_0, \zeta_1, \zeta_2)$ corresponding to the six nodes of the triangle. Since ψ_ϵ is not continuous between adjacent triangles, 6 $w_{\epsilon i}$'s must be stored for every triangle.

C.5 Resistance

The resistance R is given by

$$R = 1/W,$$

assuming the applied RMS voltage is one volt. W is the total dissipated power and is given by

$$W = \int_V \sigma |\vec{E}|^2 \, dV = 2\pi \int \int \sigma |\vec{E}|^2 \, r \, dr \, dz = \sum_{e=0}^{NTR-1} W_e.$$

Over every triangle

$$W_e = 2\pi \int \int_e \sigma_e |\vec{E}|^2 \, r \, dr \, dz,$$

where $\vec{E}$ is given by

$$\vec{E} = -\sum_{i=0}^{5} u_i \nabla a_i.$$

Using the same type of development as for the generic matrices,

$$W_e = 2\pi \sigma_e \sum_{q=0}^{5} u_q \sum_{i=0}^{5} u_i S_{qi}.$$

Bibliography

[1] Woodburne R.T., Burkel W.E., Essentials of Human Anatomy, 8th ed, Oxford Univ Press, New York, 1988.

[2] Romanes G.J., Cunningham's Manual of Practical Anatomy, vol. 2, Thorax and Abdomen, 15th ed., Oxford University Press, 1986.

[3] Vander A.J., Sherman J.H., Luciano D.S., Physiologie Humaine, McGraw-Hill, Montréal, 1975.

[4] Ganong W.F., Review of Medical Physiology, 13th ed, Appleton and Lange, Norwalk, Conn., 1987.

[5] Guyton A.C., Human Physiology and Mechanisms of Disease, 4th ed., W.B. Saunders Co., Toronto, 1987.

[6] Labonté S., "Radio-Frequency Transcatheter Ablation Technique," Candidacy Paper presented to the Dept of Elect. Eng., U of Ottawa, March 1991.

[7] Fontaine G., Scheinman M.M., eds., "Ablation in Cardiac Arrhythmias," Futura Publishing Co., Inc., Mount Kisco, NY, 1987.

[8] Scheinman M.M., ed., "Catheter Ablation of Cardiac Arrhythmias," Martinus Nijhoff Publishing, Boston, 1988.

[9] Boyd E.G.C.A., Holt P.M., "An Investigation into the Electrical Ablation Technique and a Method of Electrode Assessment," PACE, vol. 8, pp. 815-824, Nov.-Dec. 1985.

[10] Gallagher J.J., Trantham J.L., "Observations During Catheter Ablation of the Atrioventricular Conduction System in Humans," in Fontaine G., Scheinman M.M., eds., "Ablation in Cardiac Arrhythmias," Futura Publishing Co., Inc., Mount Kisco, NY, 1987.

[11] Bardy G.H., Coltorti F., Stewart R.B., Greene H.L., "Catheter-Mediated Electrical Ablation: The relation Between Current and Pulse Width on Voltage Breakdown and Shock-Wave Generation," Circul Res, vol. 63, no. 2, pp. 409-414, 1988.

[12] Holt P.M., Boyd E.G., "Bioelectric Effects of High-Energy, Electrical Discharges," in Scheinman M.M., ed., "Catheter Ablation of Cardiac Arrhythmias," Martinus Nijhoff Publishing, Boston, 1988.

[13] Holt P.M., Boyd E.G.C.A., "Hematologic Effects of the High-Energy Endocardial Ablation Technique," Circulation, vol. 73, no. 5, pp. 1029-1036, May 1986.

[14] Fontaine G., Volmer W., Nienaltowska E., Aaddaj S., Cansell A., Grosgogeat Y., "Approach to the Physics of Fulguration," in Fontaine G., Scheinman M.M., eds., "Ablation in Cardiac Arrhythmias," Futura Publishing Co., Inc., Mount Kisco, NY, 1987.

[15] Scheinman M.M., "Catheter Ablation for Patients with Cardiac Arrhythmias," PACE, vol. 9, pp. 551-564, July-August 1986.

[16] Bredikis J., Obelienius V., Knepa A., Sakalauskas J., Bredikis A., "Comparative Evaluation and Perspectives of Various Techniques for Ablation of Conduction Pathways in the Heart," in Fontaine G., Scheinman M.M., eds., "Ablation in Cardiac Arrhythmias," Futura Publishing Co., Inc., Mount Kisco, NY, 1987.

[17] Holt P.M., Boyd E.C.G.A., Crick J.C.P., Sawton E., "Low Energies and Helifix Electrodes in the Successful Ablation of the Atrioventricular Junction," PACE, vol. 8, pp. 639-645, Sept.-Oct. 1985.

[18] Morady F., Scheinman M.M., Griffin J.C., Herre J.M., Kou W.H., "Results of Catheter Ablation of Ventricular Tachycardia Using Direct Current Shocks," PACE, vol. 12, pp. 252-257, Jan. 1989, Part II.

[19] Hauer R.N.W., Robles de Medina E.O., Kuijer P.J., Westerhof P.W., "Electrode Catheter Ablation for Ventricular Tachycardia: Efficacy of a Single Cathodal Shock," Br Heart J, vol.61, no. 1, pp. 38-45, Jan. 1989.

[20] Bardy G.H., Coltorti F., Ivey T.D., Stewart R., Greene H.L., "Effects of High-Energy Electrical Shocks Delivered to the atrium of the Coronary Sinus," in Scheinman M.M., ed., "Catheter Ablation of Cardiac Arrhthmias," Martinus Nijhoff Publishing, Boston, 1988.

[21] Fontaine G., "The Effects of High Energy DC Shocks Delivered to Ventricular Myocardium," in Scheinman M.M., ed., "Catheter Ablation of Cardiac Arrhythmias," Martinus Nijhoff Publishing, Boston, 1988.

[22] Huang S.K.S., "Use of Radiofrequency Energy for Catheter Ablation of the Endocardium: A Prospective Energy Source," J Electrophysiology, vol. 1, no. 1, pp. 78-91, 1987.

[23] Saksena S., Gadhoke A., "Laser Therapy for Tachyarrhythmias: A New Frontier," PACE, vol. 9, pp. 531-550, July-Aug. 1986.

[24] Saksena S., "Histologic Effects of Laser-Induced Myocardial Damage," in Scheinman M.M., ed., "Catheter Ablation of Cardiac Arrhythmias," Martinus Nijhoff Publishing, Boston, 1988.

[25] Ciccone J., Saksena S., Pantopoulos D., "Comparative Efficacy of Continuous and Pulsed Argon Laser Ablation of Human Diseased Ventricle," PACE, vol. 9, pp. 697-704, Sept.-Oct. 1986.

[26] Lee B.I., Gottdiener J.S., Fletcher R.D., Rodriguez E.R., Ferrans V.J., "Transcatheter Ablation: Comparison Between Laser Photoablation and Electrode Shock Ablation in the Dog," Circulation, vol. 71, no. 3, pp. 579-586, March 1985.

[27] Narula O.S., Bharati S., Chan M.C., Embi A.A., Lev M., "Microtransection of the His Bundle with Laser Radiation Through a Pervenous Catheter: Correlation of Histologic and Electrophysiologic Data," Am J Cardiol, vol. 54, pp. 186-192, July 1, 1984.

[28] Pecson R.D., Roth D.A., Mark V.H., "Experimental Temperature Control of Radiofrequency Brain Lesion Size, " J Neurosurg, vol. 30, pp. 703-707, June 1969.

[29] Fox J.L., "Experimental Relationship of Radiofrequency Electrical Current and Lesion Size for Application to Percutaneous Cordotomy," J Neurosurg, vol. 33, pp. 415-421, Oct. 1970.

[30] Tabuse K., Katsumi M., Kobayashi Y., Noguchi H., Egawa H., Aoyama O., Kim H., Nogai Y., Yamaue H., Mori K., Azuma Y., Tsuji T., "Microwave Surgery: Hepatectomy Using a Microwave Tissue Coagulator," World J Surg, vol. 9, pp. 136-143, 1985.

[31] Michaletz P.A., Judge D., "Microwave Energy Compared With Heater Probe and BICAP in Canine Models of Peptic Ulcer Hemorrhage," Gastroenterology, vol. 97, pp. 676-684, 1989.

[32] Christensen D.A., Durney C.H., "Hyperthermia Production for Cancer Therapy: A Review of Fundamentals and Methods," J Microwave Power, vol. 16, no. 2, pp. 89-105, 1981.

[33] Marcus F.I., "The Use of Radiofrequency Energy for Intracardiac Ablation: Historical Perspectives and Results of Experiments in Animals," in Breithardt G., et al, eds., "Nonpharmacological Therapy of Tachyarrhythmias," Futura Publ. Co., pp. 213-219, 1987.

[34] Marcus F.I., "Radiofrequency Energy for Catheter Ablative Procedures," in Scheinman M.M., ed., "Catheter Ablation of Cardiac Arrhythmias," Martinus Nijhoff Publishing, Boston, 1988.

[35] Huang S.K., Bharati S., Graham A.R., Lev M., Marcus F.I., Odell R.C., "Closed-Chest Catheter Desiccation of the Atrioventricular Junction Using Radiofrequency Energy: A New Method of Catheter Ablation," J Am Coll Cardiol, vol. 9, no. 2, pp. 349-358, Feb. 1987.

[36] Marcus F.I., Blouin L.T., Bharati S., Lev M., Wharton K., "Production of Chronic First Degree Atrioventricular Block in Dogs, Using Closed-Chest Electrode Catheter with Radiofrequency Energy," J Electrophysiology, vol. 2, no. 4, pp. 315-326, 1988.

[37] Newman D., Evans G.T., Scheinman M.M., "Catheter Ablation of Cardiac Arrhythmias," Curr Probl Cardiol, vol. 14, no. 3 pp. 117- 164, March 1989.

[38] Hoyt R.H., Huang S.K., Marcus F.I., Odell R.S., "Factors Influencing Trans-Catheter Radiofrequency Ablation of the Myocardium," J Applied Cardiol, vol. 1, pp. 469-486, 1986.

[39] Blouin L.T., Marcus F.I., "The Effect of Electrode Design on the Efficiency of Delivery of Radiofrequency Energy to Cardiac Tissues In-Vitro," PACE, vol. 12, pp. 136-143, Jan. 1989, Part II.

[40] Huang S.K., Bharati S., Lev M., Marcus F.I., "Electrophysiologic and Histologic Observations of Chronic Atrioventricular Block Induced by Closed-Chest Catheter Desiccation with Radiofrequency Energy," PACE, vol. 10, pp. 805-816, July-Aug. 1987, Part I.

[41] Ring M.E., Huang S.K.S., Graham A.R., Gorman G., Bharati S., Lev M., "Catheter Ablation of the Ventricular Septum with Radiofrequency Energy," Am Heart J, vol. 117, no. 6, pp. 1233-1240, June 1989.

[42] Haines D.E., Watson D.D., Halperin C., "Monitoring Electrode Tip Temperature During Radiofrequency Fulguration of Ventricular Myocardium is Predictive of Lesion Size," Circulation, vol. 76, Suppl. II, abstract p. 406, 1987.

[43] Haines D.E., Watson D.D., Halperin C., "Characteristics of Heat Transfer and Determination of Temperature Gradient and Viability Threshold During Radiofrequency Fulguration of Isolated Perfused Canine Right Ventricle," Circulation, vol. 76, Suppl II, abstract p.278, 1987.

[44] Haines D.E., Watson D.D., "A Thermodynamic Model for the Heating during Radiofrequency Catheter Ablation Canine Myocardium [sic]: The Temperature Distribution is Independent of the Thermal Conductivity Constant," PACE, vol. 11, abstract p.482, 1988.

[45] Haines D.E., Watson D.D., "Tissue Heating During Radiofrequency Catheter Ablation: A Thermodynamic Model and Observations in Isolated Perfused and Superfused Canine Right Ventricular Free Wall," PACE, vol. 12, pp.962-976, June 1989.

[46] Haines D.E., Watson D.D., Verow A.F., "Electrode Radius Predicts Lesion Radius During Radiofrequency Energy Heating," Circulation Research, vol. 67, pp. 124-129, 1990.

[47] Haines D.E., Verow A.F., "Observations on Electrode-Tissue Interface Temperature and Effect on Electrical Impedance During Radiofrequency Ablation of Ventricular Myocardium," Circulation, vol. 82, pp. 1034-1038, 1990.

[48] Franklin J.O., Langberg J.J., Oeff M., Finkbeiner W.E., Herre J.M., Griffin J.C., Scheinman M.M., "Catheter Ablation of Canine Myocardium with Radiofrequency Energy," PACE, vol. 12, pp. 170-176, Jan. 1989, Part II.

[49] Haverkamp W., Hindricks G., Gulker H., Rissel U., Pfennings W., Borgreffe M., Breithardt G., "Coagulation of Ventricular Myocardium Using Radiofrequency Alternating Current: Biophysical Aspects and Experimental Findings," PACE, vol. 12, pp. 187-195, Jan 1989, Part II.

[50] Wittkampf F.H.M., Hauer R.N.W., Robles de Medina E.O., "Control of Radiofrequency Lesion Size by Power Regulation," Circulation, vol. 80, no. 4, pp. 962-968, Oct. 1989.

[51] Motamedi M., Kotadia R., Xu C.B., Lahmann M.H., "Pulsed vs. Continuous Radiofrequency (RF) Ablation: Greater Depth of Myocardial Coagulation without Crater Formation," Circulation, vol. 82, no. 4, Suppl. III, abstract 2860, Oct. 1990.

[52] Langberg J.J., Chin M.C., Rosenqvist M., Cockrell J., Dullet N., Van Hare G., Griffin J.C., Scheinman M.M., "Catheter Ablation of the Atrioventricular Junction With Radiofrequency Energy," Circulation, vol. 80, pp. 1527-1535, 1989.

[53] Wang X., Moulton K., Margolis D., Roman C., Colarne J., Friday K., Dyer J., Jackman W., "Pulse Duration Required for Radiofrequency Catheter Ablation of Accessory Pathways," Circulation, vol. 82, no. 4, Suppl. III, abstract 2856, Oct. 1990.

[54] Langberg J.J., Lee M.A., Chin M.C., Rosenqvist M., "Radiofrequency Catheter Ablation: The Effect of Electrode Size on Lesion Volume In Vivo," PACE, vol. 13, pp. 1242-1248, Oct. 1990.

[55] Evans G.T., Huang W.H., "Comparison of Direct Current and Radiofreqeuncy Energy for Catheter Ablation of the Atrioventricular Junction: Results of a Prospective Multi Center Study," Circulation, vol. 82, no. 4, Suppl III, abstract 2858, Oct. 1990.

[56] Kuck K.H., Schluter M., Geiger M., Siebels J., Duckeck W., "Radiofrequency Current Approach to Successful Catheter Ablation of Accessory Pathways," Circulation, vol. 82, no. 4, Suppl. III, Abstract 2739, Oct. 1990.

[57] Duckeck W., Engelstein E.D., Kunze K.P., "Modulation of AV Nodal Conduction by Radiofrequency Current: Prediction of Success?," Circulation, vol. 82, no. 4, Suppl III, abstract 0727, Oct. 1990.

[58] Lavergne T.L., Sebag C.I., LeHeuzey J.-Y., Motte G.A., Hidden F.A., Ourbak P.A., Guize J., "Closed-Chest Radio-Frequency Modification of Atrioventricular Junction Using a Suction Catheter: Long-term Results," Circulation, vol. 82, no. 4, Suppl. III, abstract 2859, Oct. 1990.

[59] Margolis P.D., Roman C.A., Moulton K.P., Calame J., Wang X., Lazzare R., Jackman W.M., "Radiofrequency Catheter Ablation of Left and Right Ectopic Atrial Tachycardia," Circulation, vol. 82, no. 4, Suppl. III, abstract 2854, Oct. 1990.

[60] Abstracts of original contributions, 41st Annual Scientific Session, American College of Cardiology, Dallas, Texas, April 12-16, 1992, in JACC.

[61] Abstracts from the 64th Scientific Sessions, American Heart Association, Anaheim, California, Nov. 11-14, 1991, in Supplement to Circulation, vol.84, no. 4, October 1991.

[62] Labonté S., Tang A.S.L., Walley V.M., "Microwave Ablation of the Myocardium with a Monopole Antenna," 14th Annual IEEE-EMBS Conf., Paris, France, 29 Oct.-1 Nov. 1992.

[63] Chato J.C., "Thermal Properties of Tissues," in Skalak R., Chien S., "Handbook of Bioengineering," McGraw-Hill, New York, 1987.

[64] Mechling J.A., Strobehn J.W., "A Theoretical Comparison of the Temperature Distributions Produced by Three Interstitial Hyperthermia Systems," Int J Radiation Oncology Biol Phys, vol. 12, pp. 2137-2149, 1986.

[65] Henriques F.C., "Studies of thermal injury," Archives of Pathology, vol. 5, pp. 489-502, 1947.

[66] Carstensen E.L., Miller M.W., Linke C.A., "Biological effects of ultrasound," J Biol Phys, vol. 2, pp. 173-192, 1974.

[67] Miller M.W., Ziskin M.C., "Biological consequences of hyperthermia," Ultrasound in Med and Biol, vol. 15, no. 8, pp. 707-722, 1989.

[68] Foster K.R., Schwan H.P., "Dielectric Properties of Tissues and Biological Materials: A Critical Review," Crit Rev Biomed Eng, Vol. 17, Issue 1, pp. 25-104, 1989.

[69] Schwan H.P., Foster K.R., "RF-field interactions with biological systems: electrical properties and biophysical mechanisms," Proc IEEE, vol. 68, no. 1, pp. 104-113, 1980.

[70] Stuchly M.A., Stuchly S.S., "Dielectric Properties of Biological Substances: Tabulated," J Microwave Power, Vol. 15, No. 1, pp. 19-26, 1980.

[71] Surowiec A., Stuchly S.S., Keaney M., Swarup A., "In vivo and in vitro dielectric properties of feline tissues at low radio-frequencies," Phys Med Biol, vol. 31, no. 8, pp. 901-909, 1986.

[72] Bowman H.F., Cravalho E.G., Woods M., "Theory, Measurements and Application of Thermal Properties of Biomaterials," Annu Rev Biophys Bioeng, vol. 4, pp. 43-80, 1975.

[73] CRC Handbook of Chemistry and Physics, 70th ed, CRC Press, Boca Raton, Florida, 1989.

[74] Bowman H.F., "Heat transfer and thermal dosimetry," J Microwave Power, vol. 16, no. 2, pp. 121-133, 1981.

[75] Surowiec A., Stuchly S.S., Eidus L., Swarup A., "In vitro dielectric properties of human tissues at radio-frequencies," Phys Med Biol, vol. 32, no. 5, pp. 615-621, 1987.

[76] Surowiec A., Stuchly S.S., Swarup A., "Radio-frequency dielectric properties of animal tissues as a function of time following death," Phys Med Biol, vol. 30, no 10, pp. 1131-1141, 1985.

[77] Stoy R.D., Foster K.R., Schwan H.P., "Dielectric properties of mammalian tissues from 0.1 to 100 MHz: A summary of recent data," Phys Med Biol, vol. 27, no. 4, pp. 501-513, 1982.

[78] Myers G.E., Analytical Methods in Conduction Heat Transfer, McGraw-Hill, New York, 1971.

[79] Nelson J.M., "A triangulation algorithm for arbitrary planar domains," Appl. Math Modelling, vol. 2, Sept. 1978.

[80] Hartsgrove G., Kraszewski A., Surowiec A., "Simulated Biological Materials for Electromagnetic Radiation Absorption Studies," Bioelectromagnetics, Vol. 8, pp. 29-36, 1987.

[81] Stogryn A., "Equations for calculating the dielectric constant of saline water," IEEE Trans Microwave Theory Tech, pp. 733-736, Aug 1971.

[82] Franklin A.D., "Electrode Effects in the Measurement of Ionic Conductivity," J Am Ceram Soc, vol. 58, pp. 465-473, 1975.

[83] Mansfield P.B., "Myocardial Stimulation: The Electrochemistry of Electrode-Tissue Coupling," Am J Physiol, vol. 212, no. 6, pp. 1475-1488, 1967.

[84] Weinman J., Mahler J., "An Analysis of Electrical Properties of Metal Electrodes," Med Electron Biol Engng, vol. 2, pp. 299-310, 1964.

[85] Greatbatch W., Piersma B., Shannon F.D., Calhoon S.W., "Polarization Phenomena Relating to Physiological Electrodes," Ann N.Y. Acad Sci, vol. 166 (or 167), pp. 722-744, 1969.

[86] Greatbatch W., "Metal electrodes in bioengineering," CRC Crit Rev Bioeng, pp. 1-36, Jan. 1981.

[87] Geddes L.A., DaCosta C.P., Wise G., "The impedance of stainless steel electrodes," Med Biol Eng, vol. 9, pp. 511-521, 1971.

[88] Cetas T.C., "Practical Thermometry with a Thermographic Camera: Calibration, Transmittance, and Emittance Measurements," Rev Sci Instrum, Vol. 49, No. 2, pp. 245-254, 1978.

[89] Quinn T.J., Temperature, Academic Press, Toronto, 1983.

[90] Schooley J.F., Thermometry, CRC Press, Florida, 1986.

[91] Heinisch R.P., "The emittance of blackbody cavities," in Plumb H.H., ed, Temperature, Instrument Society of America, Pittsburgh, vol. 4, Part 1, pp. 435-447, 1972.

[92] Bedford R.E., "Effective emissivities of blackbody cavities- A review," in Plumb H.H., ed, Temperature, Instrument Society of America, Pittsburgh, vol. 4, Part 1, pp. 425-434, 1972.

[93] Rohsenow W.M., Hartnett J.P., Ganic E.N., eds., Handbook of Heat Transfer Fundamentals. McGraw-Hill, NY, 1985.

[94] Conway J., Anderson A.P., "Electromagnetic Techniques in Hyperthermia," Clin. Phys. and Physiol. Meas., vol. 7, no. 4, pp. 287-318, 1986.

[95] Shen L.C., Kong J.A., Applied Electromagnetism, 2nd edition, PWS Publishers, 1987.

[96] King R.W.P., Prasad S., Fundamental Electromagnetic Theory and Applications, Prentice-Hall, Toronto, Canada, 1986.

[97] Plonsey R., Heppner D.B., "Considerations of quasi-stationarity in electrophysiological systems," Bull Mathematical Biophysics, vol. 29, pp. 657-664, 1967.

[98] Bennett C.O., Myers J.E., Momentum, Heat and Mass Transfer, McGraw-Hill, New York, 1962.

[99] Rohsenow W.M., Choi H., Heat, Mass and Momentum Transfer, Prentice-Hall, Englewood Cliffs, NJ, 1961.

[100] Labonté S., Ph. D. Laboratory Notebook, Electrical Engineering, Univ. Ottawa, 1991.

[101] Silvester P.P., Ferrari R.L., Finite element for electrical engineers, 2nd ed., Cambridge Univ. Press, 1990.

[102] Wood W.L., Lewis R.W., "A comparison of time marching schemes for the transient heat conduction equation," Int J Numer Meth Eng, vol. 9, pp. 679-689, 1975.

[103] Lapidus L., Pinder G.F., Numerical Solution of Partial Differential Equations in Sciences and Engineering, John Wiley and Sons, New York, 1982.

[104] Myers .E., "Critical time step for finite-element solutions to two-dimensional heat-conduction transients," J Heat Transfer, Trans ASME, v. 100, no. 1, pp. 120-127, Feb. 1978.

[105] Silvester P., Konrad A., "Axisymmetric triangular finite elements for the scalar Helmholtz equation," Int J Num Meth Eng, vol. 5, pp. 481-497, 1973.